



Morphological/Nanostructural Controls Toward Intrinsically Stretchable Organic Electronics

Journal:	<i>Chemical Society Reviews</i>
Manuscript ID	CS-REV-10-2018-000834.R1
Article Type:	Review Article
Date Submitted by the Author:	30-Nov-2018
Complete List of Authors:	<p>Ma, Rujun; University of California, Los Angeles, Department of Materials Science and Engineering, The Henry Samueli School of Enginee and Applied Science; Nankai University, School of Materials Science and Engineering & National Institute for Advanced Materials</p> <p>Chou, Shuyu; University of California, Los Angeles, Department of Materials Science and Engineering, The Henry Samueli School of Enginee and Applied Science</p> <p>Xie, Yu; University of California, Los Angeles, Department of Materials Science and Engineering, The Henry Samueli School of Enginee and Applied Science</p> <p>Pei, Qibing; University of California, Los Angeles, Department of Materials Science and Engineering, The Henry Samueli School of Enginee and Applied Science</p>



Morphological/Nanostructural Controls Toward Intrinsically Stretchable Organic Electronics

Rujun Ma,^{*ab} Shu-Yu Chou,^a Yu Xie^a and Qibing Pei^{*a}

Received 00th January 20xx,
Accepted 00th January 20xx

DOI: 10.1039/x0xx00000x

www.rsc.org/

The development of intrinsically stretchable electronics poses great challenges in synthesizing elastomeric conductors, semiconductors and dielectric materials. While a wide range of approaches, from special macrostructural engineering to molecular synthesis have been employed to afford stretchable devices, this review surveys recent advancements in employing various morphological and nanostructural controls to impart mechanical flexibility and/or to enhance electrical properties. The focus will be on (1) embedding percolation networks of one-dimensional conductive materials such as metallic nanowires and carbon nanotubes in an elastomer matrix to accommodate large external deformation without imposing a large strain along the one-dimensional materials, (2) design strategies to achieve intrinsically stretchable semiconductor materials that include direct blending of semiconductors with elastomers and synthesizing semiconductor polymers with appropriate side chains, backbones, cross-linking networks, and flexible blocks, and (3) employing interpenetrating polymer networks and bottlebrush structures in stretchable polymeric dielectric materials to prevent electromechanical instability. Moreover, intrinsically stretchable electronic devices based on these materials, such as stretchable sensors, heaters, artificial muscles, optoelectronic devices, transistors and soft humanoid robots will also be described. Limitations of these approaches and measures to overcome them will also be discussed.

1. Introduction

In recent years, stretchable electronics that preserve designed electrical properties under repeated tensile strain have attracted much attention, with a wide range of prospective applications, such as stretchable optoelectronic devices,¹⁻⁷ artificial muscles,⁸⁻¹¹ stretchable transistors,¹²⁻¹⁸ electronic skin,¹⁹⁻²¹ soft and humanoid robots,²²⁻²⁵ stretchable energy harvesters,²⁶⁻³⁰ and stretchable sensors.³¹⁻³⁶ Many of these are related to or work with human motions, which experience tensile strains up to 55%.^{37, 38} Conventional electronic materials, such as metals, crystalline silicon semiconductors, silicon oxide dielectrics, and conjugated polymers, are generally un-stretchable; they either crack at strains as small as 1% or undergo plastic deformation at strains greater than a few percent. To impart mechanical stretchability, two different and sometimes complementary strategies have been extensively reported in the literatures: (1) patterning nonstretchable electronic materials into special geometries such as meandering structures or wavy buckles to accommodate large external deformation in the nonstretchable materials^{13, 39-45} and (2) synthesizing new intrinsically stretchable electronic materials.^{3, 15, 46-49}

The meandering structures or wavy buckles can be attained by applying thin electronic materials onto prestretched elastomer and releasing the strain after processing. The resulting structure can be

stretched up to the prestretched value where the active components are not stretched and the high performance of electronic materials is hardly degraded. This approach has produced important stretchable electronic devices. However, challenges and obstacles still remain, such as the lack of visual transparency, complexity in the integration of these constructs on an elastomer substrate, and difficulty in shrinking the pitch size and packing a large number of functional components. Intrinsically stretchable electronics entail elastomeric stretchability for each component, and thus hinge on the development of intrinsically stretchable electronic materials.^{3, 46, 49, 50} With these materials, the device fabrication can be greatly simplified and integration of the devices with small pitch size, high density and transparency can be realized without incurring sophisticated processes.^{46, 48, 51-53} A wide range of techniques have been explored to synthesize intrinsically stretchable electronic materials, ranging from embedding nanostructured conductors and semiconductors into elastomers, to molecular engineering of conjugated polymer semiconductors for enhanced stretchability and dielectric elastomers for high permittivity. Many of these may be generalized as morphological or nanostructural control to attain intrinsically stretchable electronic materials. As a conceptual illustration of this general approach, Figure 1 shows an intrinsically stretchable thin-film field-effect transistor (TFT) via morphological/nanostructural controls of the key materials. The intrinsically stretchable conductive electrodes are realized by embedding percolation networks of one-dimensional conductive materials such as metallic nanowires and carbon nanotubes in an elastomer matrix to accommodate large external deformation without incurring large strain along the one-dimensional materials. The intrinsically stretchable semiconductor is obtained by directly blending semiconductors with elastomers and synthesizing semiconductor polymers with appropriate side chains, backbones, cross-linking networks, and flexible blocks. The

^a Soft Materials Research Laboratory, Department of Materials Science and Engineering, Henry Samueli School of Engineering and Applied Science, University of California, Los Angeles, California 90095, United States

^b School of Materials Science and Engineering, National Institute for Advanced Materials, Nankai University, Tianjin 300350, P. R. China

*E-mail: malab@nankai.edu.cn; qpei@seas.ucla.edu

intrinsically stretchable dielectric layer is achieved by employing interpenetrating polymer networks and bottlebrush structures in stretchable polymeric dielectric materials to prevent electromechanical instability. In this review, we survey strategies to synthesize elastomeric conductive, semiconductive and dielectric materials via these morphological approaches and examine how these materials are assembled to develop intrinsically stretchable electronic devices.

2. Intrinsically Stretchable Conductive Materials

Conventional conductive materials such as metal, carbon based materials and conducting polymers are brittle or undergo plastic deformation under a few percent strain. Elastomeric electrically conductive materials, representing new alternatives to rigid conventional electrical conductors, will enable the development of next-generation electronic devices such as stretchable displays,^{3, 54-56} flexible solar cells,⁵⁷ wearable healthcare sensors⁵⁸⁻⁶⁰ and soft robotics.³⁸ The fabrication of hybrid materials comprised of conductive materials and a soft matrix by morphological controls is a common approach to obtaining the intrinsically stretchable conductors. In this section, we will review a variety of stretchable conductors based on silver nanowires (AgNWs),^{47, 61-63} carbon nanotubes (CNTs),^{38, 64, 65} Graphene,^{66, 67} carbon grease,^{8, 68} conducting polymers,^{69, 70} liquid metals,⁷¹ and hydrogel^{72, 73}. A list of intrinsically stretchable conductive materials is summarized in Table 1.

2.1 Intrinsically stretchable AgNWs electrodes

Silver is the most conductive metal. The success in synthesizing silver nanowires opened an opportunity to synthesize AgNWs percolation networks that attain high electrical conductivity while allowing optical transmission and mechanical deformation of the network without significantly straining the nanowires.⁷⁴⁻⁷⁸ Thanks to the urgent need for a transparent electrode to replace indium tin oxide (ITO) for enhanced flexibility, there has been a flurry of research efforts on developing AgNWs based transparent electrode for optoelectronic device applications.⁷⁹ In addition, the relatively low fusing temperature at the intercrossing of AgNWs could further decrease the resistance of the conductive pathway.^{75, 80, 81} A variety of high performance electronic devices have been successfully fabricated by employing transparent electrodes based on AgNWs.^{27, 82-86} These AgNW conductive electrodes are prepared by vacuum filtration, spray coating or meyer rod coating. All of these methods are carried out at relatively low temperatures. Highly stretchable and transparent heater based on AgNWs for wearable electronic applications have been reported by Hong et al.⁸⁴ AgNWs percolation network were prepared by directly transferring vacuum filtration onto the elastic polydimethylsiloxane (PDMS) film. After the vacuum filtration transfer of AgNWs percolation network, the PDMS film was trimmed and fixed between two glass substrates. Electrically driven resistive Joule heating was induced by applying a constant direct current (DC) bias voltage at two ends of the AgNWs percolation network. Figure 2a shows a photograph of transparent and stretchable AgNWs/PDMS heater where the area of blue dotted circle is the AgNWs network. The transparent and stretchable AgNWs/PDMS film under a temperature of 60 °C before and after stretching with 60% strain was captured by an infrared (IR) camera and is shown in Fig. 2b. In Fig. 2c, the AgNWs/PDMS heater is affixed to a human wrist with outward and inward bending and exhibits

good stability under both conditions. The stretchable and transparent AgNWs/PDMS heater with good electrical, mechanical and thermal stability demonstrates the potential for future wearable electronics applications. Yang et al fabricated conductive and stretchable composite electrodes by spray coating AgNWs onto polyurethane (PU) and following a high-intensity pulsed light (HIPL) technique.⁸⁷ The conductivity of wire-wire junction and adhesion of wire-substrate was increased by HIPL. Figure 3a shows the fabrication of AgNWs/PU composite electrode by spray coating AgNWs onto PU and the photonic sintering process at room temperature and in air. Partial AgNWs were embedded into the PU substrate after the exposure of high intensity light. The surface roughness of the AgNWs/PU electrode was decreased to 204 nm after photonic sintering compared with the original roughness of more than 500 nm. A uniform distribution of AgNWs network with 0% strain was observed in Fig. 3b while the non-uniform distribution of sparse and dense AgNWs was shown with 100% strain. Even when the AgNWs/PU electrode was under 100% strain, its sheet resistance was less than 10 Ω/sq. Fig. 3d and 3e demonstrate that light emitting diodes (LEDs) based on AgNWs/PU composite conductors can be cyclically stretched between 0 and 20% strain. The stretchable AgNWs/PU composite electrodes show perfect performance during stretching between 0 and 20% strain. A wearable sensor based on AgNWs/PU composite electrode, which has the potential application of e-skin for robots, can detect the accurate motion of human finger joints as shown in Fig. 3f.

Stretchable AgNWs percolation network has also been developed for energy harvesting by Jeong et al,²⁷ a field that attracted remarkable attention. The stretchable and high-performance energy harvester was realized by very long stretchable AgNWs electrodes and exhibited up to 200% of stretchability and large power output. Figure 4a shows the schematic of the stretchable energy harvester structure, which was made of very long AgNWs percolation electrodes and a piezoelectric elastic composite. The piezoelectric elastic composite was prepared by mixing $(1-x)(\text{Pb}(\text{Mg}_{1/3}\text{Nb}_{2/3})\text{O}_3-x(\text{PbTiO}_3))$ (lead magnesium niobate-lead titanate) (PMN-PT), multiwalled carbon nanotubes (MWCNTs), and ecoflex silicone rubber. AgNWs percolation network prepared by the vacuum suction method using very long AgNWs was transferred onto both sides of the piezoelectric elastic composite. Various piezoelectric dipoles were obtained, while the piezoelectric particles in ecoflex silicone rubber was stressed by mechanical deformation in the piezoelectric elastic composite. AgNWs percolation network electrodes can accumulate or push electrons via the outer load by changing dipole moments and generate the output electricity. The energy harvester can be stretched up to 200% strain and return to its original state after release, as shown in Fig. 4b. Figure 4c exhibits the output open-circuit voltage and short-circuit current of the stretchable energy harvester with forward and reverse connection. The output open-circuit voltage of 4 V and short-circuit current of 500 nA in the forward and reverse connections were generated under the strain of 200%.

Although AgNWs networks have exhibited significant advantages, one critical issue that prevents AgNWs to be implemented in wide applications is high surface roughness; this creates a nonuniform top coating layer, which causes shorts and device failure. In order to address the issue of large surface roughness when AgNWs film is coated directly on the substrate, Pei group introduced a transfer technique to embed the nanowires within the surface layer of a polymer matrix.^{3, 61, 88-94} The AgNWs solution was coated onto the

release glass substrate by the meyer rod to form a uniform AgNWs percolation network, and then a monomer with photoinitiator was drop casted on top of the AgNWs percolation network. After UV curing, which was used to crosslink the elastomer, the AgNWs network was embedded in the polymer matrix. After releasing the AgNW-polymer film from the glass substrate, the freestanding film exhibits very low surface roughness, which is desirable for fabricating electronic devices. Yu et al. fabricated the AgNWs/polymer composite electrode with the surface roughness of less than 5 nm by embedding AgNWs percolation network into acrylate polymer.⁶¹ High-performance polymer light-emitting diodes were fabricated using this AgNWs/polymer composite electrode with low surface roughness.

Yun et al. fabricated bistable large strain actuators capable of strains as high as 140% by embedding the AgNWs percolation networks into a bistable electroactive polymer (BSEP), a type of shape memorable actuator polymer (Fig. 5).⁹² Figure 5a shows the schematic of the composite electrode preparation of AgNWs network in a copolymer of tert-butyl acrylate (TBA) and acrylic acid (AA) (poly(TBA-co-AA)) by in-situ photo-polymerization. The transferred AgNWs network was buried in the shape memory polymer, which can be observed from a cross-sectional SEM image as shown in Fig. 5b. The surface roughness of this composite electrode was much lower than that of AgNWs network on the polymer substrate. In addition, there was no degradation of surface conductivity after conducting peeling tests with Scotch tape thanks to the strong adhesion between the shape memory polymer and AgNWs network. The hydrophobic property of homopolymer of TBA caused the poor interfacial bonding with AgNWs network. The additional AA that was added into the homopolymer of TBA could increase the interfacial bonding between the polymer matrix and AgNWs electrode via the carboxylic acid group (Fig. 5c). The glass transition temperature of copolymer was improved by increasing the concentration of AA. The optimized concentration of AA was 5wt% considering the increase of power consumption at higher glass transition temperature. The sheet resistance of AgNWs electrode was increased when the shape memory polymer film was stretched. However, the addition of AA in the copolymer can minimize the rate of resistance increase during stretching. The sheet resistance of the conductive electrode can remain within the range of 10^2 and 10^3 Ω/sq at strains as high as 140%. The BSEP actuator had different deformation with different electric fields as shown in Fig. 5d. The area strain of actuator can reach up to 68% under the electric field of 45 MV/m. Moreover, the actuated shape can be maintained when the Joule heating current was removed and the actuator was cooled to room temperature.

For healable applications of AgNWs network, Li et al. developed a healable stretchable transparent conductor by embedding AgNWs network and poly(3,4-ethylenedioxythiophene):polystyrenesulfonate (PEDOT) hybrid layer into the surface of a Diels–Alder elastomer substrate.⁹⁵ In recent years, healable conductors, a key component in healable electronics, have been widely studied to achieve higher recyclability, increase the lifetime of the electric device and decrease the amount of electric waste.^{96–102} The AgNWs junctions were soldered by the binder of PEDOT layer to decrease the resistance of AgNWs junctions and confine the nanowires network in the surface of the polymer substrate. Ethanol-water wetting of the PEDOT layer can tune the bonding between PEDOT and AgNWs and the prestretched AgNWs network with large strain can be reached while keeping the wet

PEDOT layer. The hybrid composite film had an initial sheet resistance of 15 Ω/sq and a transmittance of 78% at 550 nm. Even when the film was stretched to 30% strain, the sheet resistance of AgNWs network was increased to only 21 Ω/sq . The razor blade cut, along the conductive surface of the copolymer, could be healed by heating at 100 °C. Figure 6a shows the mechanical healing performance of stress and strain response. Both maximum stress and strain were dramatically decreased after blade cutting with depth of 40 μm on the surface of the conductive electrode. 97% of the mechanical property was healed by heating the damaged sample for 3 min at 100 °C. The resistance change of fresh film and healed film as a function of strain is shown in Fig. 6b. The resistance of healed film was increased by 20% compared with that of the fresh film at 0% strain. The AgNW network fractures and tiny substrate cracks were observed after 100 cycles of stretching-relaxing between 0% and 60% strain as shown in Fig. 6c. After healing by heating treatment, the fractured AgNWs were reconnected as shown in the SEM image in Fig. 6d. To realize the healable device, Bae et al. used AgNWs healable conductive films to fabricate the four-wire resistive type healable touch panels.¹⁰³ AgNWs healable conductive films were prepared by embedding AgNWs percolation networks into the Diels–Alder healable polymer. Cracks can be obtained by electrical and mechanical loading. The good performance of the healable touch panel highlights the future potential in the healable electronics.

Using the intrinsically stretchable AgNWs network, Hu et al. fabricated a stretchable transparent capacitor by sandwiching the elastomer film between two AgNWs network electrodes embedded into the surface of PU substrate (Fig. 7a).⁹³ AgNWs arrays were patterned on a glass substrate utilizing a designed contact mask by spray coating. Urethane liquid rubber compounds were drop-casted over the AgNWs arrays on glass substrate and AgNWs arrays embedded in PU substrate were peeled off after curing. Figure 7b shows the resistance change of AgNWs composite electrodes with different sheet resistance as a function of tensile strain. The normalized resistance of all samples was increased when the composites were stretched. When the strains were relatively small, the normalized resistance was linearly improved for all samples with different initial sheet resistance. The composite electrodes can be stretched by more than 100% strain and the resistance at 60% tensile strain was increased between 5.4 and 20.1 times than that of composite films at 0% tensile strain with initial resistance between 8 and 44.7 Ω/sq . The capacitance change of cyclic test between 0% and 60% strain is shown in Fig. 7c. The capacitance of device at 60% strain was 0.3 times higher than that of device at 0% strain in each stretching cycle. The cycling test of capacitance change presented good reliability. As shown in Fig. 7d, the capacitance changes of device at different tensile strains as a function of applied pressure exhibited a linear response. Moreover, the sensitivity of device with same applied pressure was increased when the device was stretched. The pressure sensitivity of device at 60% tensile strain was 0.5 times higher than that of device at 0% tensile strain while the applied pressure was 100 kPa. This capacitor device by AgNWs composite electrodes with stretch and pressure sensitivities could be applied in touch screens, soft robotics, electronic skin or wearable electronics.

Despite the significant advantages of AgNWs percolation networks, the large haze value of transparent conductive AgNWs networks limits the application for most touch panels. Fabrication of transparent conductive film using smaller diameter AgNWs was expected to be the direct route to solving the haze issue. Moreover,

freestanding AgNWs electrodes exhibit poor thermal stability when thermally annealed at 180 °C and even worse thermal stability when embedded in the polymer matrix.¹⁰⁴ AgNWs coated with Zinc oxide through a low temperature atomic layer deposition could improve the thermal stability of AgNWs while maintaining a high transmittance.⁹¹

Other metallic nanowires such as copper¹⁰⁵ and gold¹⁰⁶ nanowires have been intensively investigated and have demonstrated promising results recently. Copper nanowires are also a good candidate as the stretchable conductive film because copper is 1000 times more abundant and 100 times less expensive than silver. However, the chemical oxidation of copper nanowires degrades the properties and reliability of copper nanowire films and limits the application of stretchable electronic devices. Gold nanowires possess high conductivity and oxidation resistance and are a good alternative to realizing transparent stretchable conductive films. However, gold is a noble metal and relatively expensive.

2.2 Intrinsically stretchable carbon materials electrodes

Carbon materials such as carbon grease, CNTs and graphene, which possess excellent electrical and mechanical properties are widely researched conductive materials for stretchable electrodes. Carbon grease is synthesized by mixing carbon powder with a silicon oil matrix and is capable of maintaining conductivity at high tensile strain.^{107, 108} Carbon grease has a sheet resistance of ~100 kΩ/sq and is easy to obtain and handle. Pelrine et al. stenciled conductive carbon grease on the top and bottom of the prestrained HS3 silicone film to fabricate the electrical actuator as shown in Fig. 8a.⁸ A relative strain of 117% in the central region of the actuator was observed when an electric field of 128 MV/m was applied between two carbon grease electrodes on both sides of the prestrained HS3 silicone film. Niu et al. developed an actuator by synthesizing a new dielectric elastomer and utilizing carbon grease as electrodes without prestretching. The dielectric elastomer was synthesized from Ultraviolet (UV) radiation polymerization by customizing the density of crosslink and adding the plasticizer in the material to achieve stable large strain. Figure 8b shows the performance of actuators with various crosslinker concentrations under different electric field.¹⁰⁹ A maximum electromechanical strain of 314% was achieved by tuning the amount of crosslinkers. There was no observed migration of carbon grease with actuated strain less 50%; however, when the actuated strain was more than 100%, migrated carbon grease was visible.¹¹⁰ Carbon grease also exhibits several other drawbacks; it is very messy, easily rubbed off of the elastomer substrate, has a lower interlayer adhesion, and is difficult to deposit a uniform thin layer.^{110, 111}

Many of these shortcomings can be addressed by CNTs. Pei group spray-coated single walled carbon nanotubes (SWNTs) on both sides of 3M VHB 4950 film to obtain large strain actuation.¹¹² Figure 9a shows the resistance change of SWNTs electrode on the film as a function of strain and the electrical conductivity of SWNTs composite electrode was maintained up to 700% tensile strain. Photographs of actuator exhibited the increase in strain under the applied voltage of 4.5 kV as shown in the inset of Fig. 9a. The defects of dielectric film may lead to the breakdown through the membrane under the applied electric field. However, after applying an electric field, the dielectric films with carbon grease or carbon powder broke down and became inactive.^{110, 111} SWNTs electrodes with their property of self-clear could overcome this morass and prevent premature failure

while the membrane was broken-down.⁹⁶ Figure 9b shows the SEM image of isolated patches of SWNTs near the fault. The isolated and nonconductive patches of SWNTs can improve fault-tolerance of the dielectric elastomers actuators.

A capacitive energy harvester was developed by spray-coating SWNTs on both sides of the silicone film.¹¹³ The cyclic test of SWNTs electrode on silicone film up to 100,000 cycles exhibited the stable conductivity as shown in Fig. 9c. The energy harvester under 50% tensile strain was measured at various voltages and 7.5 mJ/cm³ was achieved under an electric field of 20 MV/m (Fig. 9d). Moreover, Lipomi et al. fabricated a skin-like pressure and strain sensor by patterning SWNTs electrodes using stencil mask (Inset of Fig. 9e).⁶⁴ The morphology of SWNTs network electrodes on PDMS substrate can be changed when the substrate was stretched and relaxed. The conductivity of SWNTs electrodes on PDMS film was as high as 2200 S/cm at 150% strain. In the cyclic test, the minimum resistance was observed at the 1500th cycle due to reaching optimum morphology at that period (Fig. 9e). Figure 9f shows the stable cyclic test of capacitance change between 0% and 30% tensile strain.

Another alternative is the dry method of directly drawing out CNTs film from as-grown superaligned CNTs arrays to develop a stretchable conductor.¹¹⁴⁻¹¹⁶ Feng et al. presented a stretchable transparent conducting film made from super-aligned carbon nanotubes.¹¹⁴ Figure 10a shows a CNTs film with a width of 18 cm directly drawn from a superaligned CNTs arrays on an 8-inch wafer. The CNTs/polyethylene composite film can be obtained by straightforward roll-to-roll process. The sheet resistance and transmittance of a freestanding CNTs film as a function of strain is shown in Fig. 10b. The transmittance of the freestanding CNTs film improved, but the sheet resistance of the film increased when the stretching ratio increased. The sheet resistance was increased to 1.6 kΩ/sq at 60% strain when the transmittance was improved to 86.5% at 550 nm. Further, Liu et al. embedded superaligned CNTs film onto the surface of PDMS substrate as shown in the inset of Fig. 10c.¹¹⁷ There was no observed change of resistance after 200 cycles between 0% and 15% tensile strain. For better applications, Chen et al. fabricated stretchable and transparent supercapacitors with high performance by utilizing superaligned CNTs film (Inset of Fig. 10d).¹¹⁵ The capacitance of device was almost constant with the tensile strain up to 30% in both directions.

Graphene has been actively investigated as a transparent conductive electrode in stretchable electronics due to its fascinating electrical, optical mechanical and thermal properties.^{54, 118-121} Kim et al. synthesized a large-scale pattern of graphene films utilizing chemical vapor deposition (CVD) on thin nickel layers and transferred them to a PDMS substrate.⁶⁶ The resistance of graphene on PDMS substrate as a function of strain was investigated, as shown in Fig. 11a. There was no observed change of resistance when the film was stretched below 6% strain. However, mechanical failure occurred and the resistance further increased when the graphene film on PDMS substrate was stretched more than 6% strain due to the high tensile strength. Even though graphene possesses excellent optical and electrical performance, its high mechanical strength inhibits its application in highly stretchable electronics. To overcome the mechanical limitations of graphene, Bao group synthesized highly stretchable graphene devices by multilayer graphene/graphene scrolls (MGs) (Inset of Fig. 11b).¹²² Graphene scrolls intercalating between graphene layers can bridge cracks to provide conductive paths in the graphene sheets and remain highly conductive at high

strain. Figure 11b compared the resistance change of a plain bilayer graphene film and bilayer MGG as a function of stretching cycles at 50% strain. The plain bilayer graphene film observed 7.5 times increase in resistance, while the bilayer MGG after 700 cycles at 50% strain obtained only 2.5 times increase in resistance. To further evaluate the performance of graphene-based films, a stretchable capacitor was fabricated using different types of graphene films as gate electrodes as shown in Fig. 11c. The capacitance of devices with plain monolayer and bilayer graphene electrodes was dramatically reduced below 30% strain. However, the improved capacitance gated by MGGs and the plain trilayer graphene was observed due to the decrease in thickness of the dielectric layer when stretched. In addition, the fully transparent and stretchable all-carbon transistor controlled the switching of LED as shown in Fig. 11d.¹²² There was no observed change in LED light intensity at 100% strain. For the stretchable sensor application of graphene, Park et al. developed a highly stretchable and wearable graphene sensor through a layer-by-layer assembly technique. Figure 11e shows the resistance change of PDMS coated graphene sensors as a function of strain. The rubber yarn (RY) sensor presented high sensitivity under stretching while the nylon covered rubber yarn (NCRY) sensor exhibited a linear relationship between the resistance change and tensile strain. To test elbow bending, the NCRY sensor was sewn on elbow wrap and placed into the arm (Inset of Fig. 11f). The different signals of NCRY sensor was observed when the arm was bent with angles of 45°, 90° and 135° (Fig. 11f). The wearable electronics with graphene-based sensors provided a meaningful approach to monitor various human motions.

2.3 Intrinsically stretchable conducting polymers

PEDOT:PSS is another promising material for stretchable conductors with great mechanical, electrical and transparent properties. The conductivity of PEDOT:PSS can be as high as >1000 S/cm. Low conductivity commercial PEDOT:PSS could be rendered highly conductive by employing polar solvents, surfactants, and ionic liquids in polymer solution to control the polymer morphology during solvent drying. Dimethyl sulfoxide (DMSO), ethylene glycol (EG), zonyl, N, N-dimethylformamide and 1-ethyl-3-methylimidazolium tetracyanoborate (EMIM TCB) have all been effective in morphological control.¹²³⁻¹²⁸ PEDOT:PSS has a large elastic modulus of ~2 GPa and a small elastic strain of less than 6%.¹²⁹⁻¹³² One alternative is to incorporate PEDOT:PSS with elastomer to fabricate the conductive stretchable composite or to coat PEDOT:PSS onto a polymer to form a wavy structure. Lee et al. presented a strain-insensitive stretchable electric conductor based on PEDOT:PSS/acrylamide organogels up to 400% tensile strain.¹³³ Figure 12a shows the resistance change of the PEDOT:PSS–PAAm organogels with different ratios of PEDOT:PSS as a function of strain demonstrating the insensitive resistance change under stretching. The stretchable LED arrays under 200% strain using PEDOT:PSS–PAAm organogel as an electrical interconnect demonstrated the excellent performance of this organogel as shown in the inset of Fig. 12a. For electroluminescent applications, Teo et al. fabricated a semitransparent and stretchable alternating current electroluminescent device by sandwiching ZnS:Cu phosphor microparticles/PDMS layer between two PEDOT:PSS/EMIM TCB electrodes (Top of Fig. 12b).¹³⁴ The performance of device was maintained at the strain of 50% as shown in the bottom of Fig. 12b. Moreover, the conductivities of 3100 S/cm at 0% strain and 4100 S/cm at 100% strain for PEDOT:PSS polymer composite film were reported by Bao's group in Fig. 12c.¹³⁵ The conductivity of 100 S/cm

did not falter under the 600% strain. Inset of Fig. 12c shows the schematic of PEDOT:PSS with stretchability and electrical conductivity (STEC) enhancers. For the application of stretchable PEDOT:PSS/STEC as interconnects in high-density circuits, nine rigid field-effect transistor devices were connected by lines of PEDOT:PSS/STEC as show in the inset of Fig. 12d. 3 x 3 arrays of field-effect transistors were uniformly stretched up to 125% strain in all directions. The mobility for all the transistors was changed within ± 10% between 0% and 125% tensile strain in Fig. 12d. The PEDOT:PSS composites as the interconnects have stable electrical properties, outstanding stretchability, and show promise in potential applications in bioelectronics and wearable electronics.

2.4 Intrinsically stretchable liquid metal electrodes

Liquid metals based on gallium alloys used for soft and stretchable electronics are another novel direction due to their low toxicity, essentially no vapor pressure and can be infinitely deformed while maintaining high electrical conductivity.¹³⁶⁻¹³⁸ To date, there is no known material that shows a better combination of electrical conductivity and stretchability than liquid metal.^{136, 138} Normally, liquid metals were injected into fluidic channels as highly stretchable and conductive interconnects, antennas and wires.¹³⁹⁻¹⁴¹ Zhu et al. injected eutectic gallium indium (EGaIn) into a core of stretchable fiber made of Poly[styrene-*b*-(ethylene-co-butylene)-*b*-styrene] (SEBS) resin as shown in Fig. 13a.¹³⁸ The conductivity of this intrinsically stretchable conductor can be preserved under reversible stretching. The intrinsically stretchable and conductive fibers can also be prepared by utilizing a dip-coating method to coat liquid metal onto the silicone elastomer fiber in Fig. 13b.¹⁴² There was no apparent change in LED light intensity under 210% strain when the fibers were applied as the interconnects (Fig. 13c). Other applications were also studied, such as a stretchable acoustic device (SAD), which can be fabricated using a liquid metal coil by injecting Galinstan into a micro-patterned elastomer channel, as shown in Fig. 13d.¹⁴³ The resistance of liquid metal coil was increased by just 6% under the biaxial stretching of 30% strain (Fig. 13e). SAD as a microphone can be realized by the electromagnetic interaction between a liquid metal coil and a magnet, as shown in Fig. 13f. No observable sound pressure level change was present at the uniaxial strain of 50%.

2.5 Intrinsically stretchable conducting hydrogels electrodes

Conducting hydrogels have also been investigated for intrinsically stretchable conductor in recent years.¹⁴⁴⁻¹⁴⁶ The crosslinked network in the hydrogels provides the mechanically deformable matrix, whereas the solvent carries ions for electrical conduction with fairly low resistance. Suo group developed a transparent, high speed and large strain actuator by sandwiching a dielectric elastomer layer between two hydrogel electrodes made of polyacrylamide hydrogel containing a NaCl electrolyte as show in Fig. 14a.⁷² The active region of the actuator was highly transparent to all colors and stretchable. The area strain of 167% was reached when the voltage was applied between two hydrogel/electrolyte electrodes. The hydrogel/electrolyte conductors have lower conductivity compared with other electronic conductors at low strain; however, the hydrogel/electrolyte conductors exhibited higher conductivity than existing electronic conductors at high strain (Fig. 14b). To further maintain conductivity of the hydrogel at high strain, Ma et al. fabricated the crosslinked PAA (polyacrylic acid, *n*-PAA) hydrogels utilizing the linear PAA hydrogels co-crosslinked by the hydrophilic groups between PSA and PAA.¹⁴⁷ Figure 14c shows the resistance

change of the PEDOT:PSA/n-PAA and PEDOT:PSS/n-PAA hydrogels with different weight ratios as a function of strain. The conductivity of the PEDOT:PSA/n-PAA hydrogel was maintained under the strain of 800%. Two LED lights interconnected by PEDOT:PSA/n-PAA hydrogel remained turned on when stretched to a 200% strain (Inset of Fig. 14c). For the healable application of hydrogel, stretchable conductive supramolecular hydrogels with good mechanical strength, self-healability, and thermo-processability were prepared.¹⁴⁸ Figure 14d presented healable performance of poly (N-acryloyl glycinamide-co-2-acrylamide-2-methylpropanesulfonic) hydrogels with PEDOT/PSS (PNAGA-PAMPS-PEDOT/PSS). The hydrogel cut into two pieces by a sharp blade can be healed back to 85% of its previous form by immersing into a 90 °C water bath for 3 h. There was no significant difference of the conductivity between the original and healed hydrogels. The hydrogel with excellent performance in stretchability and conductivity can have promising potential applications where biocompatibility is of concern.

Overall, none of the conventional conductive materials, such as metals, carbon-based materials, or electrolytes are intrinsically stretchable. By embedding these materials in an elastomeric matrix, intrinsically stretchable conductors have been obtained that retain high electrical conductivity at large strains. Morphological or microstructural control plays a central role as each of these conductors have their own unique combination of chemical, electrical, and mechanical attributes and available form factors. Metal nanomaterials, particularly AgNWs, embedded in the surface of an elastomer substrate exhibit promising performance in high surface conductivity, intrinsic stretchability and high transparency. CNTs also present excellent mechanical deformability and offer higher chemical stability than AgNWs. PEDOT:PSS is attractive in that it is a commonly used transparent material to enhance the performance of organic thin film electronic devices. Hydrogels and liquid metals have the advantage of their electrical conductivity being unchanged or the change being completely reversible within certain strains. The conductors made of 1-D materials generally exhibit different degrees of continuous deterioration in repeated stretching. Further morphological or microstructural investigations should upgrade the performance of all these materials. Still, a slew of stretchable electronic devices have already been demonstrated with eye-catching deformability.

3. Intrinsically Stretchable Semiconductor Materials

Conventional semiconductors such as silicon, indium gallium zinc oxide, and pentacene are more brittle than metals. To achieve mechanical stretchability in electronic devices, efforts have been focused on engineering special mechanical structures and architectures to accommodate strain in brittle materials while stretched. Several representative works include the wavy structure,¹⁴⁹ wrinkle structure,⁴² in-plane serpentines,⁴⁵ rigid island with soft elastic interconnects,^{150, 151} and kirigami architecture.¹⁵²⁻¹⁵⁴ Despite these extrinsic approaches being compatible with rigid semiconductors, they have limited durability and require complicated fabrication. In order to achieve stretchable electronics with high strain tolerance, an alternate route is to develop intrinsic stretchable semiconductors. A truly intrinsically stretchable semiconductor material can deform elastically while maintaining its electrical properties. In recent years, much effort has been put into developing intrinsically stretchable organic semiconductors for

organic solar cells (OSCs),¹⁵⁵⁻¹⁵⁹ organic light emitting electrochemical cells (OLECs),^{3, 160} organic light emitting diodes (OLEDs),⁴ and organic field-effect transistors (OFETs).^{46, 161-164} Morphology is the key factor that dominates the mechanical properties and charge transport of the semiconductor materials; the details in molecular mixing, film texture, degree of crystallinity of individual phases, and phase separation of the blend are all controlled by the organic semiconductor film morphology.^{155, 157, 165} However, the main challenge in designing an intrinsically stretchable semiconductor arises from the conflict of the material morphology being against the design rule of semiconducting polymers. An ideal polymer that has great electrical transport property requires a morphology of high crystallinity and dense packing, whereas a soft polymer that has high stretchability requires an amorphous morphology with low glass transitional temperature and large free volume. Recent studies have reported achieving intrinsically stretchable semiconductor materials by directly synthesizing molecular stretchable materials through side chain engineering, polymer backbone modification, crosslinking of polymer networks, and infusion of flexible blocks into copolymers.^{155-157, 166-169} However, the method of synthesizing a stretchable semiconductor is very complicated. Thus, a simple approach was also developed to control the morphology of the polymer film through blending the current organic semiconductors with elastomers to achieve an intrinsically stretchable semiconductor.^{3, 4, 46, 158, 160, 164, 170-173} A list of intrinsically stretchable semiconductor materials is summarized in Table 1.

3.1 Achieving intrinsically stretchable semiconductors for OSCs

Organic semiconductors are normally synthesized from π -conjugated polymers and they have the advantages of achieving high mobility and inheriting mechanical resistance to strain. The semiconductor layer in OSCs is usually a heterojunction blend of electron-donor and electron-acceptor materials. The charge transport properties and the elastic properties are determined by the morphology and molecular structure of the composite blend. Lipomi *et al.* revealed the photovoltaic properties of OSCs under strain.¹⁶⁹ The OSCs are based on two different conjugated polymers that blend with [6,6]-phenyl C61 butyric acid methyl ester (PCBM); the two conjugated polymers are poly(3-hexylthiophene) (P3HT) and a donor-acceptor conjugated polymer that contains repeating units of diketo pyrrolo-pyrrolo, thiophene, thienothiophene, and thiophene (DPPT-TT). The authors observed that conjugated polymers have a direct impact on the photovoltaic properties of OSCs under strain. Blending PCBM into P3HT drastically stiffened the P3HT:PCBM film from 0.92 GPa to 4.3 GPa, whereas blending PCBM into DPPT-TT only brought the film's elastic modulus from 0.99 GPa to 1.4 GPa.¹⁶⁹ The authors suspect that the difference in film morphology (Fig. 15a) contributes to the difference in the mechanical property, but a detailed study was not provided. It is not a surprise that the greater the elastic modulus of the film, the easier the film will crack. Figure 15b shows that crack formation under 20% strain is a lot worse in the P3HT:PCBM film compared with the DPPT-TT:PCBM film. In addition, the results show that the crack formation in the active layer has a direct impact on photovoltaic properties. The increase in open-circuit voltage (V_{oc}) is greater in P3HT:PCBM based OSCs compared with DPPT-TT:PCBM based OSCs under strain. It is suspected that an increase in V_{oc} has a direct correlation with crack density, and the higher the crack density, the greater increase of V_{oc} in solar cells.¹⁶⁹ The highest power conversion efficiency (PCE) achieved by both OSCs are similar; 0.47% for P3HT:PCBM based OSC and 0.42% for DPPT-TT:PCBM based OSC. By carefully designing the molecular structure

of the conjugated polymers in synthesis, stretchable conjugated polymers with great mobility can be achieved. P3HT is one of the most widely explored organic semiconductors due to its excellent properties, but unfortunately it is too brittle for stretchable OSCs application. Lipomi and coworkers later discovered that the length of the alkyl side-chain has a direct influence on the mechanical properties of poly(3-alkylthiophene) (P3AT).^{155, 156} As shown in Fig. 16a, cracks were observed in the P3HT:PCBM film, whereas no cracks were observed in the P3DDT:PCBM film under 10% strain. The results confirm that as the length of the alkyl side chain in P3AT increases, the tensile modulus drastically reduces, which is explained by the decreasing crystallinity in the polymer films.¹⁵⁶ An organic solar cell based on P3AT:PCBM has been demonstrated without losing its photovoltaic properties where P3DDT:PCBM shows a 0.3% PCE. In the same work, the authors also discovered a common processing additive, diiodooctane (DIO), significantly reduced the tensile modulus in the P3AT:PCBM film. Polymeric or small molecular additives, which are used to increase the solar cell efficiency, tend to act like a plasticizer. A detailed study on the effect of DIO on film modulus was done by Pei and coworkers, and an organic solar cell based on a polymer blend of poly(thieno[3,4-b]-thiophene/benzodithiophene) (PTB7), [6,6]-phenyl-C71-butyric acid methyl ester (PC₇₁BM), and a small amount of DIO exhibited intrinsic stretchability up to 100% strain.¹⁵⁸ The highest PCE measured for the OSC device is 3.48% and remained at 2.99% after 100 stretch-release cycles. Figure 16b demonstrates a stretchable OSC up to 100% strain. The stretchability is due to the presence of free volume in the semiconductor film, which results from the slow evaporation of DIO; these free spaces in the polymer film allow grain sliding during large deformation. The DIO additive has a direct impact on the morphology of the polymer blend as shown in Fig. 16c. The atomic-force microscopy (AFM) images reveal that the PTB7:PC₇₁BM blend film shows phase separation with domains, whereas the blend with DIO displays morphology with smaller grains uniformly dispersed in the film. The authors speculate that the elastomeric behavior of the film may be attributed to the small grain domains, which can tolerate large deformation by enduring small motions. The dichroic ratios were also measured to prove no cracks formed while the blend film with DIO was under strain.¹⁵⁸

3.2 Achieving intrinsically stretchable semiconductors for OLECs and OLEDs

Blending approach was also used in achieving intrinsically stretchable light emitting electronics. The first intrinsically stretchable OLEC was reported by Yu *et al* in 2011; the sky-blue OLEC could be stretched up to 45% (Fig. 17a).¹⁶⁰ The semiconductor layer is composed of a blue emissive polymer (polyfluorene copolymer (PF-B)), an ionic conductor (poly(ethylene oxide) dimethacrylate ether (PEO-DMA)), and a salt (lithium trifluoromethane sulfonate (LiTf)). It is observed that the light intensity of the blue OLEC parallel to the stretching direction is 2.8 times higher than that of the perpendicular direction with a polarizer; this phenomenon can be explained by the alignment of the light-emitting polymer.¹⁶⁰ Liang *et al.* fabricated a yellow OLEC with an improved stretchability of up to 120% over 1000 cycles.³ The device performance of the yellow OLEC is shown in Fig. 17b and the device remained functional under 120% strain. The active luminescent layer consisting of a blend of yellow emissive polymer (SuperYellow), ethoxylated trimethylpropanetriacrylate (ETPTA), polyethylene oxide (PEO), and lithium trifluoromethane sulfonate (LiTf) was laminated between two AgNW-PU electrodes. Super Yellow is comprised of high

molecular weight, which contributes to large-strain stretchability.¹⁷⁴⁻¹⁷⁷ ETPTA was added to the blend to conduct ions and to form a crosslinking network, which is beneficial in stabilizing the P-I-N junction during OLEC operation. Moreover, the crosslinking networks provide elasticity to the stretchable semiconductor film. Here, PEO serves as an ionic conductor; incorporating PEO into the polymer blend further enhances the stretchability of the semiconductor film. Pei and coworkers further studied the morphology of the SuperYellow:ETPTA:PEO:LiTf film and revealed that the yellow luminescent layer exhibits a rubbery elasticity.¹⁷⁰ Figure 17c shows the SEM image of the OLEC blend's film morphology. An interpenetrating network of a phase separated morphology is witnessed where SuperYellow forms a continuous network while ionic mediums fill the pores. The pores inside the film could accommodate large strain without undergoing plastic deformation (Fig. 17d). The dichroic ratio of the OLEC blend remains around 1 up to 100% strain, which reveals that SuperYellow polymer chains remain random. Both the conjugated polymer network and ionic phase are amorphous, hence, stretching does not induce polymer chain orientation.¹⁷⁰ Although stretchable OLEC's simple structure and easy processing are beneficial for low cost applications, their slow turn-on and low efficiency make them undesirable for display application. To achieve high device performance, an OLED structure is favorable. The first stretchable OLED was demonstrated by Liang *et al.*; this white OLED can be stretched up to 130% and the emission intensity is fairly uniform across the lit area (Fig. 17e).⁴ The luminescent layer is a blend of white light-emitting polymer (WLEP) and 1,3-bis[(4-tert-butylphenyl)-1,3,4-oxadiazolyl]phenylene (OXD-7). As a π -conjugated polymer, the white light-emitting polymer have advantages in its intrinsic stretchability. Thus, the white light-emitting polymer was selected to achieve an intrinsically stretchable OLED. Liang *et al.* reported that as the stretching-releasing cycle increases, the intrinsically stretchable OLED shows a decreasing trend in brightness. It is speculated that the change in electroluminescence of the OLED under strain is directly related to the film morphology. More studies need to be performed in charging injection interfaces and molecular orientation of the emissive layer to better understand the electroluminescence performance.

3.3 Achieving intrinsically stretchable semiconductors for OFETs

In order to achieve a fully stretchable OFET, it is essential to develop an intrinsically stretchable active-channel material. Conjugated semiconductor polymers have also been developed as an active layer for intrinsically stretchable OFETs. Both molecular synthesis and blending approach were used to develop stretchable semiconductors for OFETs. Bao and coworkers reported a highly stretchable OFET that could be stretched up to 265% in the perpendicular direction and up to 160% in the parallel direction while maintaining transistor characteristics (Fig. 18a).¹⁶¹ P3HT was chosen to be used as a channel material due to its advantage in mechanical properties; with the 2D packing structure, P3HT could tolerate large deformation by reorienting its polymer backbones.^{161, 178} High stretchability was achieved due to the formation of microcracks inside the P3HT layer with PU/P3HT/PU structure over 50% strain.¹⁶¹ Figure 18b shows the morphology of the P3HT layer under 0% and 200% strain; it can be detected that the microcrack size is much smaller than the size of the device, which contributes to the stretchability of the film. In order to further explore stretchable semiconductor polymers, Bao and coworkers developed a quick and easy soft contact lamination method to study the electrical properties of semiconductor polymers under strain. Among all the

materials they investigated, poly(isoindigo-bithiophene) (PII2T) demonstrated both high stretchability and stable mobility under high strain. This method successfully identified a feasible candidate for stretchable transistors.¹⁶³

Side-chain engineering has been used in polymeric electronics very recently; several side-chain modifications have been studied for intrinsically stretchable electronic applications. Isoindigo-based polymers are known to provide high-charge carrier mobility, attributable to their great electron-withdrawing ability in the conjugated polymer system.¹⁷⁹ Polymers containing isoindigo-bithiophene backbone and branched side-chains have previously shown great charge transport ability with high stretchability.¹⁸⁰ Chen and coworkers demonstrated an intrinsic stretchable field-effect transistor using a semiconductor with PII2T main-chain that incorporates a carbosilane side-chain (PII2T-C8); the mobility remained above $1 \text{ cm}^2/\text{V}\cdot\text{s}$ even under 60% strain.¹⁸¹ Polymers with carbosilane side-chain and isoindigo-bithiophene backbone show a dense lamellar packing morphology, as seen in Fig. 18c, and results in a shorter π - π stacking distance. The condensed inter-chain packing structure results in a superior charge transport property. Grazing incident X-ray diffraction was used to study the film morphology of the stretchable polymers. Figure 18d shows that when the X-ray light is perpendicular to the stretching direction, a decrease in lamellar distance is observed under 40-60% strain; when the film is stretched beyond 80%, the lamellar distance returns to its original value. The decrease in lamellar distance between 40-60% tensile strain is due to the alignment of the polymer chain in the stretching direction; when the strain increases beyond 80%, crack formation helps release the tensile strain on the polymer film and the lamellar distance reverts to its original value. Figure 18e demonstrates the stretchable thin film topography under strain, and the hypothesis can be proven through the AFM images. The same group later reported another intrinsic stretchable semiconductor polymer that also contained isoindigo-bithiophene backbone but with poly(butyl acrylate) (PBA) side-chains.¹⁸² PBA is an elastic polymer with a low glass transitional temperature of $-54 \text{ }^\circ\text{C}$; by introducing PBA into the PII2T backbone, the resulting semiconductor polymer was able to be stretched to 60% strain while maintaining its electrical properties. As shown in Fig. 19a, a pristine PII2T exhibits a well-organized packing morphology, but with an increasing amount of PBA introduced to the PII2T polymer, the film morphology became disordered due to the interruption of polymer interchange by the elastic side-chains. The AFM images also suggest a decrease in polymer crystallinity with an increase in PBA content, which results in a soft semiconductor polymer. The soft mechanical property of the semiconductor is further confirmed by the optical microscope images in Fig. 19b. The pristine PII2T polymer clearly shows crack formation under stretch and as the amount of PBA content increases, the film ductility improves drastically.¹⁸²

Elasticity is an important property for intrinsically stretchable electronics; however, most of the works reported so far only focus on softening the semiconductor materials through increasing amorphous fraction at the molecular level of the polymer to achieve greater strains without forming cracks. The mechanical and electrical properties after the film returned to its original state were rarely discussed. For a stretchable electronic to be useful, it is important for the polymer film to exhibit the same properties it had prior to the stretch once it is released back to its original state. A well-known approach used to achieve a true elastic polymer is through the crosslinking of polymer networks. Crosslinking of polymer networks

prevents irreversible sliding between polymer chains, suppresses aggregation of polymer chains, and reduces crystallinity of the polymer film.^{183, 184} Wang *et al.* synthesized a diketopyrrolopyrrole (DPP)-based conjugated polymer with cross-linkable PDMS oligomers, which were used to fabricate an intrinsically stretchable semiconductor. The resulting FET device achieves $0.66 \text{ cm}^2/\text{V}\cdot\text{s}$ at 0% strain and maintains a stable mobility above $0.4 \text{ cm}^2/\text{V}\cdot\text{s}$ after 500 cycles of stretch-and-release cycles under 20% strain.¹⁸⁵ DPP polymers are known to be one of the best performing conjugated polymers with high mobility,^{186, 187} while PDMS is known to be one of the most flexible due to the presence of an Si-O-Si bond, which can vary between 135° to 180° . The DPP-based conjugated polymer crosslinked with PDMS oligomers results in a polymer film with increased elasticity; no crack formation was observed after 500 stretch-and-release cycles under 100% strain.¹⁸⁵ In Fig. 20a, optical microscope images of both crosslinked polymers (20DPPTTECx) and non-crosslinked polymers (20DPPTTEC) under 0% and 150% strain are shown; the observation of crack formation under 150% strain in non-crosslinked polymer film was found, whereas no cracks were visible in the cross-linked polymer film. In addition, the AFM images of both crosslinked polymers and non-crosslinked polymers are shown in Fig. 20b. The nanofiber morphology is observed in the 20DPPTTEC film indicating high crystallinity domains, while the 20DPPTTECx film shows a decrease in nanofiber domains, which implies a decrease in crystallinity.¹⁸⁵

Another approach than can be used to achieve a stretchable semiconductor is through synthesizing conjugated block copolymers, which combines a conjugated polymer block and a flexible polymer block. The block copolymer approach enables the fine-tuning of the mechanical properties and electrical properties of the synthesized materials. One of the earlier works in synthesizing block copolymers for stretchable electronics application was reported by Müller *et al.*¹⁶⁸ Semiconductor diblock copolymers that consist of polyethylene (PE) and regioregular P3HT exhibit outstanding flexibility and stretchability up to 600% strain, which is the best performing stretchable semiconductor to date.¹⁸⁵ P3HT was chosen here for its excellent conducting properties thanks to its semi-crystalline structure, while PE provides exceptional mechanical properties and chemical resistance. The diblock copolymer combines the advantages of both polymers and results in good electronic and mechanical performance, which are required for stretchable electronics.¹⁶⁸ Figure 20c shows the P3HT-PE diblock copolymer stretched up to 600%. The Optical microscope images show a classical neck formation, which is a result of plastic deformation of the copolymers. However, the irreversible plastic deformation of the P3HT-PE diblock copolymer under strain is not desirable. Furthermore, due to the introduction of the insulator block into the P3HT block, its electrical property is comprised with an average mobility of $0.02 \text{ cm}^2/\text{V}\cdot\text{s}$ at 0% strain which is two magnitudes lower than the $1 \text{ cm}^2/\text{V}\cdot\text{s}$ charge carrier mobility benchmark for FET.¹⁸⁵⁻¹⁸⁹ A different synthesis utilizing block copolymers was proposed by Peng *et al.* In this work, the authors designed a new semiconductor-rubber-semiconductor triblock copolymer based on the principle of thermoplastic elastomers. The alternating rubbery and hard segments facilitate the elastic deformation of the triblock semiconductor as shown in the insert of Figure 21b. The semiconductor material used in the triblock is, once again, the well-studied semiconductor polymer P3HT and the rubber material used in this ABA triblock copolymer is poly(methyl acrylate) (PMA).¹⁶⁷ The two-phase nanostructure contains a crystallinity domain that provides charge transport in a rubber matrix, which helps to increase

the semiconductor's mechanical stretchability.¹⁶⁷ Figure 21a demonstrates the proposed film morphology of the P3HT-PMA-P3HT triblock copolymers, where P3HT forms a nanofibrillar network with ordered polymer inter-chain stacking embedded in a rubbery PMA matrix. The nanofibrillar networks allow the triblock copolymer to reduce the content of the semiconductor materials while retaining its electrical properties.^{190, 191} The P3HT-PMA-P3HT copolymer demonstrates the mechanical characteristics of elastomers as shown in Fig. 21b where the film deformed elastically with 6 MPa Young's modulus and an elongation at break of 140%. Compared with the P3HT homopolymer with reported values of 28 MPa Young's modulus and 13% elongation at break, the result further confirms PMA successfully contributes to increasing film stretchability and elasticity.¹⁶⁸ The annealing temperature plays an important role in film morphology of the triblock copolymers; as the temperature increases, the nanofibrillar structure appears, as shown in Fig. 21c. The authors suspect the nanofibrillar structure is the result of dense and ordered pi-pi stacking of P3HT. The nanofibers help to connect P3HT networks and provide efficient charge transport pathways.¹⁶⁷

Despite side-chain engineering, infusing flexible blocks into copolymers, and modifying segmented polymer backbones being successful at enhancing the molecular stretchability of semiconductor films, most of the works reported thus far have failed to demonstrate both high mobility and high stretchability simultaneously. Incorporating polar substituents into a conjugated polymer is known to influence the morphology of the polymer film and provides dynamic behavior to the polymer chains.⁴⁹ Oh *et al.* present an intrinsic stretchable semiconductor, which incorporates hydrogen-bonding moieties to achieve high stretchability and charge mobility under strain. Introducing hydrogen-bonding moieties into DPP conjugated polymers helps to partially break down the conjugated network and promote dynamic non-covalent crosslinking networks, which results in lower elastic modulus.⁴⁹ The dynamic non-covalent crosslinking networks can be easily broken-down to accommodate mechanical strain; at the same time, it possesses a self-healing ability, which allows the semiconductor film to return to its original state.⁴⁹ The synthesized stretchable material is based on DPP repeating units and non-conjugated 2,6-pyridine dicarboxamide (PDCA) moieties in the polymer backbone. PDCA is chosen here to introduce hydrogen bonding to the flexible DPP backbones; in addition, due to the presence of the two amide groups in PDCA, hydrogen bonding enables the formation of polymer networks while maintaining its elastic modulus. The authors believe the decrease in elasticity was due to an increase of the amorphous fraction in the polymer film, which enables mechanical stretchability. The chemical structures of the stretchable semiconductor can be found in Fig. 22a with different PDCA amounts added. The dichroic ratio was studied to gain insight into polymer chain alignment on strain; it was found that when 0 % PDCA was added to DPP, initially, the dichroic ratio increased slightly under strain due to polymer chain alignment and then fell back to ~1 due to the relaxation of the polymer chain after crack formation in the film. In contrast, when 10 % PDCA was added, the dichroic ratio increased linearly to 1.8 as the film was stretched to 100% (Fig. 22b). In order to study the charge transport properties of the semiconductor polymer, an OFET based on PDMS substrate was fabricated. As shown in Fig. 22c, when the strain is applied in a perpendicular direction up to 100% in the P3 device, the mobility remains above 1 cm²/V·s from 1.32 cm²/V·s at 0 % strain. In addition, the P3 device shows little degradation in mobility after 100 cycles of stretching between 0 to 100 % strain as shown in Fig. 22e. In addition to its intrinsic stretchable characteristic, dynamic hydrogen-bonding

in the polymer also enables a self-healing ability via post treatments through heat or solvent annealing, which promotes chain movement as illustrated in Fig. 22f. The self-healing ability is further confirmed by AFM images in Fig. 22g. This work successfully designs an intrinsically stretchable semiconductor with self-healing capabilities, which provide robust mechanical properties for wearable electronics applications.

Instead of creating intrinsically stretchable semiconductors through sophisticated molecular design and complicated chemical synthesis, blending elastomers into organic semiconductor polymers is a simple method to improve the overall stretchability of organic electronics. However, because elastomers are typically an insulator, the overall electronic properties of the semiconductor layer are often worsened. Xu *et al.* recently reported a highly stretchable organic semiconductor film that maintains its good charge transport characteristic under large strain.¹⁶⁴ This is a result of the nanoconfinement effect of polymers attributed to enhancing chain dynamics in the amorphous phase of the polymer while constraining growth in the crystallinity phase. Nanoconfinement morphology is achieved by mixing a high-mobility semiconducting polymer DPPT-TT and a soft elastomer (SEBS). Matching of surface energy between the two materials results in nanoscale mixing morphology as shown in Fig. 23a. DPPT-TT forms nanofibrils inside an elastic SEBS polymer matrix. The nanofibrils are formed from phase separation while individual DPPT-TT nanofibrils are connected together, which contributes to good charge transport; the soft SEBS polymer increases mechanical stretchability and prevents cracks from forming (Fig. 23b). Together, the nanoconfinement of the polymer enables high stretchability and good charge transport of the organic semiconductor materials.¹⁶⁴ Another intrinsically stretchable composite semiconductor with high mobility under large strain was reported by Kim *et al.* The composite semiconductor was achieved by blending PDMS rubber with P3HT nanofibril (P3HT-NF).¹⁹² The resulting composite forms a percolated pathway for charge transport and considerably enhances the crystallinity of the P3HT-NF film, which results in enhanced charge mobility.^{171, 193, 194} The film morphology of P3HT-NF percolated PDMS rubber composite under strain is shown in Fig. 23c; when the intrinsically stretchable semiconductor film is first stretched, P3HT-NF starts to straighten to accommodate the strain. When the film is stretched to 50% some rupture is observed, as indicated by yellow arrows in Fig. 23c. However, due to the presence of the PDMS matrix, under 50% strain, most of P3HT-NF remains connected and the film can be stretched or twisted, while still returning to its original shape without forming any cracks (Fig. 23d). Moreover, the P3HT-NF/PDMS stretchable film was made into TFT and the mobility under different strains were studied (Fig. 23e). It is worth noting that once the TFT is stretched to 50% along the direction of channel length, only a slight decrease in mobility from 1.4 to 0.8 cm²/V·s is observed (Fig. 23e). The stable performance under large strain demonstrates P3HT-NF/PDMS has great potential in a wide range of applications.

Other than thin films, organic semiconductor can also be made into long and continuous nanowires by electrospinning process which is known to improve the electrical properties and mechanical properties of the organic semiconductors. Lee *et al.* reported a facile way to achieve an intrinsically stretchable semiconductor by utilizing electrospinning method.¹⁹⁵ The organic semiconductor material was composed of fused thiophene diketopyrrolopyrrole (FT4-DPP)-based polymer and PEO. The high electric field during the electrospinning process results in highly ordered alignment of the FT4-DPP:PEO

nanowires in the longitudinal direction, which then contribute to better charge transport mobility comparing with FT4-DPP:PEO thin films.¹⁹⁶ Due to its high molecular weight, PEO is chosen here as a molecular binder to mix with low molecular weight FT4-DPP to help maintain continuous polymer jet during electrospinning process. In addition, the low elastic modulus and low glass transition temperature of PEO help to decrease the overall elastic modulus of the FT4-DPP:PEO composite nanowires and therefore increase their overall mechanical ductility.¹⁹⁶ In order to achieve higher stretchability and improved stability under high stretching cycles, Lee *et al.* prestretched the elastic substrate, then applied the FT4-DPP:PEO nanowires on the prestretched substrate to create a serpentine-like geometry. Figure 24a shows the schematic illustration of deformable FET with serpentine FT4-DPP:PEO nanowires. Optical images of 100% strain in the length-direction shows the nanowires are continuous and stay connected under 100% strain. Alternately, FT4-DPP nanowires without PEO under strain was also demonstrated in Figure 24b. From the optical microscope image, it can be observed that the nanowire is disconnected under 25% strain. This proves that incorporation of PEO as the polymer binder improves the stretchability of the nanowires. Figure 24c shows the morphological change of the FT4-DPP nanowire under strain. During stretching, PEO acts as the binder to FT4-DPP and main the nanowire overall structure whereas FT4-DPP's lamellar structure unfold and increase the π - π stacking distance which also results in decrease in transport mobility. The stretchable OFET composed of FT4-DPP:PEO nanowires show high field-effect mobility ($>8 \text{ cm}^2\text{V}^{-1}\text{s}^{-1}$) and can be both stretched and compressed under 100% strain. Other semiconducting materials such as P3HT:poly(ϵ -caprolactone) (PCL) and poly(3,3'-didodecylquaterthiophene) (PQT-12):PEO have also been reported to be made into electrospun nanowires to achieve stretchable transistors.^{197, 198}

The semiconductor 1-D network materials have also been explored as the electrical components in stretchable electronics.^{46, 162} Among all, CNTs have been used in the channel layer for intrinsically stretchable OFET; the network microstructure accommodates large strain through sliding and buckling of individual wires without losing the junction. Chortos *et al.* reported an intrinsically stretchable OFET, which could be stretched to 100% strain. The semiconductor CNT was prepared by sorting with poly(3-dodecylthiophene) (P3DDT),¹⁶² and the device retained good transistor characteristics up to 100% strain. A fully stretchable OFET fabricated with all solution process has also been demonstrated. Liang *et al.* reported a good stretchability of SWCNT-based transistor, which can be stretched up to 50% by using the lamination technique. The authors believe that the intrinsic stretchability of the semiconductor channel is credited to the unique morphology, where the elastomeric dielectric copolymer infiltrates into the SWCNT and forms an interpenetrating network. Individual carbon nanotubes are wrapped around by elastomer while maintaining the nanotube-nanotube junction. The SWCNT-elastomer network helps to prevent junction disjoining under large strain and further increases the stretchability and stability of the CNT layer.⁴⁶

Controlling the film morphology of the semiconductor materials through chemical synthesis and blending of elastomers into semiconductor materials has shown great success in developing intrinsically stretchable semiconductors. All these reports indicate that the future of stretchable electronics is promising. However, current organic semiconductor materials still have some limitations. Most of the materials face the challenge of being incapable of

retaining their electrical properties under tensile strain. New materials, new methodologies, and new fabrication processes are in need to develop stretchable organic semiconductors that can achieve high elasticity, high mobility, and high stability simultaneously. A systematic study in how film morphology, intermolecular stacking interaction, and molecular structure affects the semiconductor properties (i.e. mobility, and charge transport capability) should be revealed to provide a guideline in developing intrinsically stretchable organic semiconductors.

4. Intrinsically Stretchable Dielectric materials

Recent progress in soft materials have made it possible to fabricate stretchable electronics that can mimic human muscles or can be mounted to soft surfaces like human skin and smart clothes.¹⁹⁹⁻²⁰⁴ Dielectric materials typically take parts in capacitors and transistors due to their insulating nature or exhibit their electromechanical transducing properties in dielectric elastomers.²⁰⁵⁻²⁰⁷ Their charge-accumulating property opens up a wide range of applications, such as sensors²⁰⁸⁻²¹¹, soft robotics,²¹²⁻²¹⁶ energy harvesting generators,^{207, 217-222} refreshable braille displays,^{216, 223-226} and tunable lenses²²⁷. To gain stretchable high-performance implementations with minimum external energy consumption, high dielectric constant with good stretchability is usually required for dielectric materials. Traditional inorganic dielectrics display high permittivity but lack stretchability, whereas polymeric dielectrics are possible for high strain situations but usually have low dielectric constants. Researchers have now focused on employing morphological controls to impart extensibility for inorganic dielectrics and improve electrical performances for intrinsically stretchable dielectrics. Here, we will introduce several morphological control methods that cover both topics with an emphasis on enhancing electrical performances. For a convenient comparison of the properties for different dielectric materials, the performances of different type of dielectrics and their corresponding morphological control methods are shown in Table 3.

Traditional gate dielectric materials for FETs are rigid organics like SiO_2 and Al_2O_3 , which are brittle and incompatible with stretchable substrates. There are two common approaches used to impart mechanical compliance and robustness to dielectric materials. The first approach involves geometrically patterning the brittle inorganics into wrinkled or wavy structures,^{13, 208, 228-233} and the second combines rigid transistor islands with a stretchable substrate.^{202, 231, 234, 235} For the wrinkled configurations, the dielectrics are stretched from the buckled state to a flat surface before inducing strain along the material bonds themselves. For the rigid island structures, the high strains are accommodated by elongation in the soft substrate rather than the rigid components themselves.

Inorganic dielectrics with wrinkled structures possess high stretchability while maintaining excellent electrical performance as their flat configurations. However, the pre-stretching process required to obtain the wrinkle structures is cumbersome. Also, the inorganic dielectrics typically rely on costly vacuum-based deposition methods for fabrication, which is incompatible with solution printing processes. Furthermore, wavy structures can be incompatible with certain devices that require planar interfaces.²³⁶⁻²³⁸ The electrical performance of the dielectrics with rigid island structures remain consistent with their original values because the stretchability is

imparted by the stretchable regions between islands; however, a larger degree of expansion usually requires a larger area of inactive substrate, which will cause a trade-off between the device density and stretchability.

4.1 Improving Electrical Performance of Polymeric Dielectrics

As we introduced earlier, even though inorganic dielectrics have high dielectric constants, they are too brittle to adapt to stretchable matrices unless they incorporate wavy or island structures. The hunt for truly intrinsically stretchable dielectrics has turned to polymers.^{161, 162, 209, 239-272} Polymers are a natural choice given their inherent stretchability and insulating properties, but the dielectric constant for a pure polymer is usually not comparable to inorganic dielectrics.^{20-30, 43-47, 49} To improve the electrical performances for both transistors and dielectric elastomers, morphological control methods on dielectric materials are used to enhance dielectric constant, reduce elastic modulus and improve electrical breakdown strength for lowering their working voltage and increasing extendibility. For the reverse process, when mechanical energy transfers to electricity, microstructures are useful to increase deformation of dielectrics to gain a higher energy transfer ratio. This review will highlight important works on all four aspects.^{31-42, 48}

4.2 Enhancing Dielectric Constant

There have been attempts to enhance dielectric constant of elastomers by blending them with highly polarizable conjugated polymers or grafting polar side groups to the elastomer backbone.^{273, 274} Carpi et al. mixed poly(3-hexylthiophene) (PHT) into silicone at very low concentrations (1-6 wt%). The best electromechanical strain response result was with 1 wt% PHT due to both the increase in dielectric constant (~2000@1Hz) and the reduction in tensile elastic modulus, which was supported by a 7.6% transverse strain with only an 8 MV m⁻¹ electric field. It was accompanied by a small increase in dielectric loss and a small reduction in tensile elastic modulus. Dunki et al. introduced sulfonyl lateral polar group to polysiloxanes backbone with two post-polymerization synthetic strategies and tuned the dielectric constant from 5 to 22.7.²⁷⁵ Liang et al. used PU-co-polyethylene glycol (PU-co-PEG) as a transparent elastomer dielectric for their transistors.²⁶⁴ The urethane acrylate oligomers contributed to the high stretchability, while the PEG diacrylate helped increase the dielectric constant.^{276, 277} The dielectric constant of this copolymer was as high as 13 at 12Hz, with a > 90% optical transmittance at 550 nm and a > 50% elongation at break. Overall, the electrical performances (on current and mobility) of transistors declined by about 50% at 50% strain. Failure happened at strains over 50% due to the stretching limit of the dielectric. During fatigue testing, the transistors survived 1000 stretching cycles at 20% strain. Eventually, they used the stretchable TFT matrix to drive an OLED, since the cutoff voltage of the drain supply (-2.7V) was in line with the threshold voltage of the OLED. As shown in Fig. 25, the TFT integrated OLED still functioned at 30% strain. Azide-crosslinked SEBS is synthesized as dielectric elastomer by Zhenan Bao's group.^{209, 267, 278, 279} It has a gate dielectric capacitance of 1.75 nF cm⁻². Azide-crosslinked SEBS is slightly more elastic and has a little higher dielectric constant (~2.5 at 100 Hz) than uncrosslinked SEBS. Their transistor arrays could stretch to 100% strain in both x and y directions without cracking, delamination, or wrinkles as supported by the stable performance shown in Fig. 26a & b. The transistors' electrical performance remained stable at up to 600% strain when subjected to pressure, twisting or biaxial stretching. The transistors showed potential in real-life applications with their mechanical robustness since they survived 1000 times of cycle test at 100% strain

(Fig. 26c & d). As a proof of concept for skin electronics, a 10 x 10 stretchable matrix was integrated with resistive tactile sensors, which can be conformably attached to human's skins. In Fig. 26e & f, the on-current map showed the accurate detection of the 6 conductive legs of an artificial ladybug.

Interpenetrating polymer networks (IPN) also help to increase the dielectric constant of silicone-based elastomers: one component enhances the mechanical property, while the other imparts polarity.²⁸⁰ Tugui et al. created a dual-phase continuous microstructure by interpenetrating PDMS with a polyurethane containing tetramethyldisiloxane moieties and carboxyl groups.²⁸¹ The polarity from the urethane groups and pendent carboxyl groups contributed to a high dielectric constant (12 at 1 Hz, 5.9 at 10 000 Hz) when compared to a pure PDMS film. This high dielectric constant induced a 7.1% strain actuation with an electric field of 20 MV m⁻¹ and with its fast response time, it proved suitable for dielectric elastomer generators, which was first proposed by Pelrine et al. in 2001.²⁸¹⁻²⁸⁵

Introducing organic dipole groups into the elastomers lead to a uniform distribution of moieties with high permittivity and it can also lower mechanical stiffness, which is beneficial for higher actuation strain at lower electric fields.^{273, 286-288} However, the polar groups introduced in this method reduce the overall dielectric strength and makes the EAP more susceptible to moisture. Intrinsically stretchable dielectrics can also take the form of inorganic dielectric nanofillers dispersed in polymer substrates. In this setup, the nanofillers dominate the electrical properties with their high dielectric constant and the polymer substrate ensures mechanical compliance.²⁶⁶ Cai et al. introduced a hybrid gate dielectric that mixed 50 nm cubic phase BaTiO₃ nanoparticles in PDMS film.²⁶⁶ BaTiO₃ itself has a permittivity around 200. With BaTiO₃ dispersed at a 26% nanoparticle volume ratio, the hybrid dielectric had a capacitance of 2.9 nF cm⁻², which was independent of frequency between 100 Hz and 1 MHz. The constant small leak current (~40 pA for a 2000 x 200 μm TFT channel) at 60% strain showed good compatibility without pinholes between BaTiO₃ and PDMS. Both TFT and the logic circuits based off this hybrid dielectric could stretch to over 50% strain across thousands of cycles in either parallel or perpendicular directions to the channel without significant electrical performance degradation.

Like the hybrid dielectrics, ceramic or conductive nanofillers can also improve the electromechanical performance of dielectric elastomers. Huang et al. blended a PU matrix with high dielectric constant copper phthalocyanine oligomers (PolyCuPc) and conductive PANI to achieve 9.3% strain with a 20 MV m⁻¹ electric field.²⁸⁹ With ratio of PANI:PolyCuPc:PU = 14:15:85, the dielectric constant reached 800 at 1 Hz. Hu et al. reported a nanocomposite that included a small amount of aluminum nanoparticles with superior actuation performance to pure acrylate copolymer.²⁹⁰ A 4 v/v% loading of Al₂O₃ nanoparticles resulted in a maximum 56% actuation area strain, 140 MV m⁻¹ dielectric strength, and a dielectric constant of 8.5 at 100 Hz. As shown in Fig. 27, dielectric constant changed proportionally with the increase in Al₂O₃ concentration. For other dielectric elastomer options, Polyvinylidene fluoride-trifluoroethylene (P(VDF-TrFE)) is an electrostrictive polymer often studied for its actuation potential.²⁹¹⁻²⁹³ P(VDF-TrFE) shows a high dielectric constant (425 at 1Hz) when mixed with copper-phthalocyanine (CuPc) fillers.²⁹³ Zhang et al. demonstrated a thickness strain of -1.91% with a 13MV m⁻¹ electric field. For a silicone based dielectric elastomer, Bele et al. blended a low concentration

(2 wt%) of Titanium dioxide-based nanotubes into a PDMS matrix and increased dielectric permittivity to 1.33 times (4 at 1 kHz) when compared to PDMS without nanofillers.²⁹⁴ 4.2% lateral strain was performed at 40 kV/mm without significant damage to dielectric strength (>60 kV/mm) and elastic modulus (0.4 MPa). Yin et al. chose thermoplastic polyurethane as the elastomer substrate, mixed in Barium titanate nanoparticles as dielectric constant-enhance fillers and dibutyl phthalate as plasticizers.²⁹⁵ The resulting dielectric elastomer composite, which showed a 28% increase in dielectric constant and a 43% decrease in Young's modulus, was then employed into an energy harvesting generator and harvested energy density up to 1.71 mJ/cm³ with 0.45% efficiency.

Mixing in ceramic nano-fillers with high dielectric constants is an efficient way to increase dielectric constant, but high loads can lead to agglomeration of the nano-fillers, which will eventually impede the flexibility and electromechanical response of elastomers.^{296, 297} An improved method incorporates conductive components at relatively low weight ratios.²⁹⁸⁻³⁰¹ After reaching a critical point, the conductive components are close to each other while still separated by the insulating polymer. Covering the conductive nano-fillers with insulating shells helps prevent them from forming conductive pathways. Wang et al. reported a reduction of 30% of actuation electric field by blending in 0.75 wt% MWCNTs fillers.³⁰² The long aspect ratio of MWCNTs lowered the concentration requirement for forming a percolation network and helped generate more "microcapacitors" within the insulating elastomer matrix to enhance dielectric constant. Graphene is another promising option for conductive nanofillers because of its excellent conductivity and π -conjugated structure.³⁰³⁻³⁰⁵ Zhang et al. mixed 1.5 wt% partially reduced graphene oxide (GO) nanosheets in an elastomer to realize a high dielectric constant of 11 (@1kHz) and a low modulus of 0.51 MPa of the elastomer nanocomposite.³⁰³ The elastomer matrix, polystyrene-*b*-poly(*n*-butyl acrylate)-*b*-polystyrene (SBAS) triblock copolymer, was synthesized with reversible addition/fragment transfer emulsion polymerization with high elasticity and low modulus. The high permittivity is another benefit from the polar ester groups of poly(*n*-butyl acrylate) blocks. Nanofillers with higher aspect ratios are typically more promising to enhance elastomers' dielectric constant. Ji et al. employed high aspect ratio (~700) silver nanofibers (AgNFs) obtained by electrospinning to improve the dielectric constant of cellulose nanofibers-epoxy hybrid films.²¹¹ With an optimal concentration of 1.2 wt%, AgNFs imbedded film showed a high dielectric constant of 9.2 (120kHz) and high transmittance of 90%. Both dielectric constant and transmittance of elastomers with AgNFs are higher than those of same concentration AgNPs (4.0, 29%) and AgNWs (5.5, 90%) imbedded films (Fig. 28a, b & c). A capacitive touch sensitive panel was utilized to visualize the sensitivity of each of the films; AgNF-imbedded films showed the highest capacitance change due to its high dielectric constant. As shown in Fig. 28d, by replacing the glass cover on a commercial phone, this AgNF-imbedded dielectric layer exhibits great potential in future flexible electronics.

Solid nanofiller can significantly enhance the electrical performance of dielectric elastomers, but the compliance mismatch introduced by their rigid natures can harm the elastomers' overall extensibility.³⁰⁶ High permittivity liquid inclusions or liquid dielectric layers therefore shine a light in the realization of dielectric elastomers with high dielectric constant and low mechanical rigidity. Bartlett et al. mixed eutectic Ga-In liquid metal into silicone or polyurethane polymer matrix and brought up the dielectric constant

by 400%.^{307, 308} Mazurek et al. embedded high permittivity glycerol droplets into PDMS matrix and the permittivity of this elastomer increased to 16 at 1 kHz compared with 3.3 for that of pure PDMS.³⁰⁹ Glycerol droplets also worked as softeners to reduce the elastomer's modulus and enhance actuation performance.³¹⁰ Besides introducing liquid inclusions, Shi et al. designed dielectric gels with high dielectric constant (30~50) at 1 K-10 MHz frequency range, and transmittance of 99% with a 100 μ m thick gel.³¹¹ The dielectric gel can be actuated with 172% strain under 4kV/mm electric field. As shown in Fig. 29a, the dielectric gel contains a 3D polymer network and both propylene carbonate and ethylene carbonate as liquid solvents due to their high dielectric constant. A bioinspired lens, whose focal length can be tuned with an applied electric field, was demonstrated (Fig. 29b).

4.3 Lowering Elastic Modulus

For dielectric elastomers, ceramic or conductive nanofillers tend to increase the elastic modulus of elastomers, which is contradictory to the purpose of lowering actuation voltage. Moreover, the weak interfaces between nanofillers and a polymer matrix are usually the main cause of dielectric loss.³¹² Instead, synthesizing ductile long-chain polymer with low elastic modulus can help enhance the elongation at break and save the cumbersome work of physically blending in nanofillers.^{313, 314}

Zhang et al. reported that a low modulus, ductile silicone elastomer can be constructed with a long chain polymethylvinylsiloxane and a lower concentration of cross-linker.³¹² Zhao et al. lowered the modulus of an acrylic-based elastomer from 0.41 MPa to 0.11 MPa by tuning the component ratio of crosslinkers, resulting in an actuation coefficient increase from 14.43 to 51.54.³¹⁵ With a dielectric constant of 5.67 @ 1kHz, the actuation strain of the modified elastomer reached 52.08% at a low electric field of 21.57 kV/mm, which is 4.2 times higher than that of a commercial VHB 4910 tape, given the same electric field (17 kV/mm). Their work was also applied into a bend actuator, which was capable of a 180° bending angle.

4.4 Increasing Electrical Breakdown Strength

Dielectric elastomer has the unique electromechanical transducing property that can be applied to fabricate "artificial muscle". However, the maximum electromechanical performance of dielectric elastomers is capped by their dielectric strength, beyond which the charged species mobilize and conduct electricity.³¹⁶ Localized defects, pull-in effect, and high leakage current can further reduce the film's dielectric strength before intrinsic breakdown is reached. To prevent electromechanical instability (EMI), pre-straining the film can strengthen the film before electrical actuation.³¹⁷⁻³³⁴ However, pre-straining dielectric film is a cumbersome process that requires additional rigid and passive frames, which could introduce stress concentration points leading to failure in the film.^{316, 335} The mass and volume of the additional frame may also lower the devices' work density and power to mass ratio.³³⁶ In order to eliminate the extra operation and frame that are included in the pre-strain process, other morphological control methods now attract great attention to prevent pull-in effect and enhance elastomers' electrical breakdown strength without a physical pre-strain frame.^{224, 337-354}

IPNs are fabricated by cross-linking a pre-strained polymer network (A) that is swollen with another short chain monomer (B).^{338, 339} The IPN fabrication process is shown in Fig. 30.³³⁹ IPN film is released from the support after curing process. The cured polymer network (B) is now locked in compression, which prevents network

(A) from returning to the unstrained state. The pre-strained effect on network (A) is therefore maintained without needing a pre-stretching frame. Suo et al. proposed an IPN model consisting of a long chain network and a short chain network.³³⁷ The long chain polymer imparts the large actuated deformation ability of the system, while the short chain polymer counteracts the positive thinning loop by constraining the polymer network. There are a number of successful results reported using VHB-based IPNs.³³⁸⁻³⁴¹ Tugui et al. studied the effect of the network composition and host network pre-stretch step for a series of bimodal silicone interpenetrating networks.³⁵⁵ Ha et al. utilized poly(1,6-hexanediol diacrylate) as the short chain network to lock a pre-strained VHB film. A IPN film with 18.3 wt% poly(1,6-hexanediol diacrylate) preserved a pre-strain that was up to 275% and generated a 233% actuated strain.^{338, 339} The performance of this IPN films was comparable to a 300% x 300% biaxially pre-strained VHB 4905 acrylic elastomer. However, interpenetrating network polymers still require a complex pre-stretching process to achieve the long chain polymer network. This process can lead to early failure in the dielectric elastomer due to local stress concentrations.

Based on the same model as Suo et al. proposed, Niu et al. developed an easy dielectric elastomers fabrication method that avoids any pre-strain process by tuning the concentration of cross-linkers in the mixture of acrylate comonomers.³⁵⁰ Not only is the entire fabrication process adaptable to conventional coating techniques, but the resultant elastomer has a stress-strain relationship that demonstrates rapid stiffening above a threshold strain, which completely suppresses EMI and imparts high actuated strain. Plasticizers were also introduced into the system to lower the glass transition temperature of the elastomer. As a result, the softer film was less viscoelastic and responded faster. In their work, a dielectric elastomer film with dielectric constant of 5 at 12Hz, a 314% actuated strain or a maximum breakdown field of 236 MV m⁻¹ can be customized while fully suppressing its EMI.

Besides adjusting the concentration of cross-linkers, adding short chain cross-linkers with multi-functional groups is also helpful in rapidly raising the elastomer stiffness at small strain ratios. Ren et al. introduced trimethylolpropane triacrylate (TMPTA) as a trifunctional cross-linker into a BSEP system.^{224, 332, 333, 352-354} The long chain urethane diacrylate contributed to the large actuated deformation, while TMPTA countered the pull-in effect by stiffening the polymer network. Even a small amount of TMPTA (1 wt%) was sufficient to overcome EMI.³⁵⁶ Pei group developed a refreshable and bistable Braille display and rewritable electronic papers based on BSEPs.^{216, 223, 225, 226, 357} Braille dots made from their polymer bonded to electrodes could reversibly switch between stable dome and flat states as shown in Fig. 31.²²⁵ Rewritable papers could show and preserve arbitrary digits without extra energy consumption as shown in Fig. 32.³⁵⁷ Arrays of these dots could then display any Braille character and support 0.6 N of force, creating a strong, tactile surface. By manipulating the concentration and content of cross-linkers, there is no need to incorporate pre-stretching into the dielectric elastomer fabrication process. Instead, UV curable cross-linkers can be mixed with other monomers to achieve a crosslinked network in one step, which simplifies the device fabrication procedure and enables a wider range of applications.

Another type of elastomer with a bottlebrush structure was also reported as an EMI free, as-casted elastomer without needing pre-

actuation stretching.^{350, 351, 358-364} This single component elastomer is created by grafting two or more side chains to the polymer backbones with covalent bonds. The structure of a bottlebrush elastomer is demonstrated in Fig. 33a.³⁶⁵ Elastomers with low modulus and high extensibility are more ideal in biomedical applications, as they permit large stroke and low-voltage actuation.^{214, 227, 366} The side chain structures of the bottlebrush elastomers reduce the entanglement of polymer backbones by densely tethering long side chains, which release the molecular constraint on larger deformation states and result in rapid onset strain-stiffening. Figure 33b compares the true stress-area expansion curve of coiled elastomers, conventional biaxially pre-strained elastomers, and bottlebrush elastomers.³⁵¹ Daniel et al. demonstrated a low modulus (~100 Pa) elastomer with bottlebrush structures,³⁵⁰ where the film was stretchable to 1000% strain. Varnoosfaderani et al. obtained bottlebrush elastomers with a large range of moduli (100 Pa ~ 1 MPa), by adjusting the polymerization degree of both the side chains and the polymer backbones.³⁵¹ Their actuators (dielectric constant = 2.94) managed a > 300% strain actuation with a low electric field below 10 MV m⁻¹. The effective work density and electromechanical efficiency were 10 kJ m⁻³ and 50% respectively. Caspari et al. used modified polysiloxane with butylthioether side chains and achieved a dielectric constant of 5.4 at 1 MHz, with an area actuation strain of 200% with 53 kV/mm electric field.³⁶⁷ The polar side groups help increase the dielectric permittivity to 4.3 when compared with pristine PDMS elastomers (~3) and suppress the electromechanical instability under large actuation strains.

Aromatic voltage stabilizers were explored due to their electron trapping ability by phenyl groups.³⁶⁸ The trapped electrons reduce the electric field strength on cathode by acting as negative space charges, thus reducing further electron migration from cathode, which will delay electrical breakdown. Voltage stabilizers can either be mixed in as additives or designed into elastomers' chemical structures. Razak et al. synthesized soft copolymer elastomers with varying chain lengths of PDMS and polyphenylmethylsiloxane (PPMS) as aromatic voltage stabilizer, with a dielectric constant of 3.4 at 1 MHz.³⁶⁹ With an optimal aromatic group concentration of ~0.84 mmol/g⁻¹, the electrical breakdown strength of PDMS-PPMS copolymer (~72 kV/mm) showed an improvement over pure PDMS elastomer (53 kV/mm). Madsen et al. blended voltage stabilizer copolymers into PDMS-based elastomers followed by crosslinking, which lead to a random dispersion of aromatic domains in a continuous PDMS matrix.³⁷⁰ With the concentration of 1.4 mmol/g⁻¹ of phenyl groups, the electrical breakdown strength of the crosslinked elastomer is 18% higher than a PDMS reference elastomer.

For solid dielectric elastomers, pull-in effect will lead to permanent dielectric breakdown. But for liquid dielectrics, liquid will merge immediately and recover its insulating state under electric breakdown.³⁷¹ Acome et al. fabricated a soft dielectric elastomer with PDMS as a shell and a vegetable-based transformer oil as a liquid dielectric.³⁷¹ As shown in Fig. 34a, when experiencing a pull-in transition step, the electrostatic force on PDMS exceeded its mechanical restoring force and led to the formation of a donut shape without electric breakdown when two electrode sides were pulled together. With a stack of 5 self-healable actuators, a gripper, which is comparable to natural muscles with an actuation stroke of 7mm, was demonstrated to move delicate object as seen in Fig. 34b.

4.5 Fabricating Microstructures for Reverse Energy Transfer

By reversing the energy flow in the actuators, dielectric elastomers can provide a simple way to harvest energy from mechanical energy sources.^{207, 217-221, 291} The concept of dielectric elastomer generators was first suggested by Pelrine et al. in 2001, which led to the creation of several generator configurations.^{285, 291, 372, 373} The basic operating principle is that capacitance changes in the dielectric elastomer between strained states and relaxed states lead to changes in the potential of the stored charges, thus the electrical potential energy.²⁹¹ As shown in Fig. 35a, Li et al. presented a triboelectric nanogenerator with a structure that alternatively stacked a planar “dielectric-conductive-dielectric” layer and a wavy “conductive-dielectric-conductive” layer.^{220, 221} The wavy structure allowed the generator to bend, stretch, and compress, creating a maximum volume charge density of 0.055 C m^{-3} that was used to drive an electronic watch. Microstructures were also created on one side of the dielectrics to increase contact areas. When attached to the bottom of a pair of shoes, the generator powered a pedometer and a fitness tracker while the user was jogging (Fig. 35b). In their subsequent work, a generator with an ultrahigh, 1160% stretchability and 96.2% transparency outputs an open-circuit voltage of 145 V and an instantaneous areal power density of 35 mW m^{-2} .²²² As shown in Fig. 35c, the generator powered 20 LEDs in both the initial state and the stretched states with finger tapping. The transparent generator was also attached to a liquid crystal display and drove the screen with finger presses.

Besides these high electrical and mechanical performance metrics, biocompatibility is another vital metric for the consideration of non-invasive wearable devices. Most popular material selections of dielectric elastomers and stretchable transistors are polyurethane, silicone and acrylate. Based on their manufacturers' Material Safety Data Sheets, most of the commercial polymer products are listed as biocompatible. Direct cytotoxicity experiments on flexible silicon field effect transistors on polyimide, stretchable silicon FETs, InGaN light emitting diodes, and AlInGaPAs LEDs on low modulus silicone all showed no inflammation or systemic immunologic responses.³⁷⁴ Most concerns of the biocompatibility debates come from the inorganic inclusions inside the polymer composites. To date, only a few iron oxide nanoparticles with surface modification have been approved by FDA (Venofer®, Ferrlecit®, INFed®, Dexferrum® and Feraheme®).³⁷⁵ Other nanoparticles, Au, Ag and metal oxide nanoparticles, etc., have been actively investigated in clinical trials. Studies have shown promising results for inorganic nanoparticle cores with biocompatible shells or surface modification.³⁷⁶ Plant extract synthesized metal nanoparticles can also be a novel source for biocompatible inclusions.³⁷⁷

Soft and stretchable electronic devices are novel entries into the medical and wearable markets where irregular interfaces are needed to interact with soft tissues. Artificial muscles also see applications in human muscle rehabilitation and robotics. With the expansion of advanced electronics, pressure to develop dielectric materials with more advanced performance has increased. Here, discussions were focused on specially designed morphological control methods to help dielectric materials reduce the requirement for external energy input while exhibiting larger extendibility. Sensitivity-enhanced capacitors/transistors-based medical and sports devices, actuation electric field-reduced artificial muscles are now more promising to become household implementations.

5. Conclusion

Recent progress in soft materials have made it possible to fabricate stretchable electronics that can be mounted to soft surfaces like human skin and smart clothes. Traditionally, these surfaces have posed difficulties due to their large strain deformation. To enable mechanical stretchability of electronic materials, geometrically patterning the brittle inorganics into wrinkled/wavy structures or combing rigid transistor islands with a stretchable substrate is the general approach. However, in order to make intrinsically stretchable electronic devices, all components need to be stretchable to avoid limitations by their reliance on brittle components. In this review, we have investigated recent achievements of intrinsically stretchable conductors, semiconductors and insulators and their applications in intrinsically stretchable organic electronics. Considering the advantages of a facile manufacturing process, a high strain tolerance, and a low cost, intrinsically stretchable electronics offer new opportunities to stretchable electronic devices. Moreover, these stretchable electronic devices with intrinsically stretchable components will advance future developments in wearable devices, foldable electronics, electronic skins, energy storage, and medical devices. Finally, we also note that morphological/nanostructural systems comprising two distinct materials could encounter modulus mismatching, such as in the AgNW/elastomer composite electrode. While embedding the nanowires in the elastomer matrix deters separation or other failures that may impact the structural integrity. Studies on the stability of the materials and devices under repeated stretching cycles have been reported, but more comprehensive characterization should be carried out, and remedies be developed.

Conflicts of interest

There are no conflicts to declare.

Acknowledgements

The authors wish to acknowledge finance support from the Air Force Office of Scientific Research (Grant no. FA9550-15-1-0340) and the National Robotic Initiative Program of the National Science Foundation (Grant no. 1638163). This work was partially support by the “111 Project” of China (B18030).

References

1. J. Lee, J. A. Wu, M. X. Shi, J. Yoon, S. I. Park, M. Li, Z. J. Liu, Y. G. Huang and J. A. Rogers, *Adv Mater*, 2011, **23**, 986-991.
2. M. Kaltenbrunner, G. Kettlgruber, C. Siket, R. Schwodiauer and S. Bauer, *Adv Mater*, 2010, **22**, 2065-2067.
3. J. J. Liang, L. Li, X. F. Niu, Z. B. Yu and Q. B. Pei, *Nat Photonics*, 2013, **7**, 817-824.
4. J. J. Liang, L. Li, K. Tong, Z. Ren, W. Hu, X. F. Niu, Y. S. Chen and Q. B. Pei, *Acs Nano*, 2014, **8**, 1590-1600.
5. Z. Y. Fan, H. Razavi, J. W. Do, A. Moriwaki, O. Ergen, Y. L. Chueh, P. W. Leu, J. C. Ho, T. Takahashi, L. A. Reichertz, S. Neale, K. Yu, M. Wu, J. W. Ager and A. Javey, *Nat Mater*, 2009, **8**, 648-653.
6. D. J. Lipomi, B. C. K. Tee, M. Vosgueritchian and Z. N. Bao, *Adv Mater*, 2011, **23**, 1771-1775.
7. H. E. Lee, S. Kim, J. Ko, H. I. Yeom, C. W. Byun, S. H. Lee, D. J. Joe, T. H. Im, S. H. K. Park and K. J. Lee, *Adv Funct Mater*, 2016, **26**, 6170-6178.

8. R. Pelrine, R. Kornbluh, Q. B. Pei and J. Joseph, *Science*, 2000, **287**, 836-839.
9. R. Shankar, T. K. Ghosh and R. J. Spontak, *Soft Matter*, 2007, **3**, 1116-1129.
10. P. Brochu and Q. B. Pei, *Macromol Rapid Comm*, 2010, **31**, 10-36.
11. J. D. W. Madden, N. A. Vandesteeg, P. A. Anquetil, P. G. A. Madden, A. Takshi, R. Z. Pytel, S. R. Lafontaine, P. A. Wieringa and I. W. Hunter, *IEEE J Oceanic Eng*, 2004, **29**, 706-728.
12. G. Shin, C. H. Yoon, M. Y. Bae, Y. C. Kim, S. K. Hong, J. A. Rogers and J. S. Ha, *Small*, 2011, **7**, 1181-1185.
13. K. Park, D. K. Lee, B. S. Kim, H. Jeon, N. E. Lee, D. Whang, H. J. Lee, Y. J. Kim and J. H. Ahn, *Advanced Functional Materials*, 2010, **20**, 3577-3582.
14. S. H. Chae, W. J. Yu, J. J. Bae, D. L. Duong, D. Perello, H. Y. Jeong, Q. H. Ta, T. H. Ly, Q. A. Vu, M. Yun, X. F. Duan and Y. H. Lee, *Nat Mater*, 2013, **12**, 403-409.
15. T. Q. Trung, S. Ramasundaram, B. U. Hwang and N. E. Lee, *Adv Mater*, 2016, **28**, 502-509.
16. F. Xu, M. Y. Wu, N. S. Safron, S. S. Roy, R. M. Jacobberger, D. J. Bindl, J. H. Seo, T. H. Chang, Z. Q. Ma and M. S. Arnold, *Nano Lett*, 2014, **14**, 682-686.
17. R. A. Doganov, E. C. T. O'Farrell, S. P. Koenig, Y. T. Yeo, A. Ziletti, A. Carvalho, D. K. Campbell, D. F. Coker, K. Watanabe, T. Taniguchi, A. H. C. Neto and B. Ozyilmaz, *Nat Commun*, 2015, **6**, 6647.
18. M. Kaltenbrunner, T. Sekitani, J. Reeder, T. Yokota, K. Kuribara, T. Tokuhara, M. Drack, R. Schwodiauer, I. Graz, S. Bauer-Gogonea, S. Bauer and T. Someya, *Nature*, 2013, **499**, 458-463.
19. K. Takei, T. Takahashi, J. C. Ho, H. Ko, A. G. Gillies, P. W. Leu, R. S. Fearing and A. Javey, *Nat Mater*, 2010, **9**, 821-826.
20. S. Wagner, S. P. Lacour, J. Jones, P. H. I. Hsu, J. C. Sturm, T. Li and Z. G. Suo, *Physica E*, 2004, **25**, 326-334.
21. S. C. B. Mannsfeld, B. C. K. Tee, R. M. Stoltenberg, C. V. H. H. Chen, S. Barman, B. V. O. Muir, A. N. Sokolov, C. Reese and Z. N. Bao, *Nat Mater*, 2010, **9**, 859-864.
22. N. Paine, J. S. Mehlhng, J. Holley, N. A. Radford, G. Johnson, C. L. Fok and L. Sentis, *J Field Robot*, 2015, **32**, 378-396.
23. J. C. Nawroth, H. Lee, A. W. Feinberg, C. M. Ripplinger, M. L. McCain, A. Grosberg, J. O. Dabiri and K. K. Parker, *Nat Biotechnol*, 2012, **30**, 792-797.
24. E. Buselli, A. M. Smith, L. M. Grover, A. Levi, R. Allman, V. Mattoli, A. Menciassi and L. Beccai, *Microelectron Eng*, 2011, **88**, 1676-1680.
25. G. Kovacs, P. Lochmatter and M. Wissler, *Smart Materials & Structures*, 2007, **16**, S306-S317.
26. J. H. Lee, K. Y. Lee, M. K. Gupta, T. Y. Kim, D. Y. Lee, J. Oh, C. Ryu, W. J. Yoo, C. Y. Kang, S. J. Yoon, J. B. Yoo and S. W. Kim, *Adv Mater*, 2014, **26**, 765-769.
27. C. K. Jeong, J. Lee, S. Han, J. Ryu, G. T. Hwang, D. Y. Park, J. H. Park, S. S. Lee, M. Byun, S. H. Ko and K. J. Lee, *Adv Mater*, 2015, **27**, 2866-2875.
28. S. Park, H. Kim, M. Vosgueritchian, S. Cheon, H. Kim, J. H. Koo, T. R. Kim, S. Lee, G. Schwartz, H. Chang and Z. A. Bao, *Adv Mater*, 2014, **26**, 7324-7332.
29. F. Yi, L. Lin, S. M. Niu, P. K. Yang, Z. N. Wang, J. Chen, Y. S. Zhou, Y. L. Zi, J. Wang, Q. L. Liao, Y. Zhang and Z. L. Wang, *Adv Funct Mater*, 2015, **25**, 3688-3696.
30. K. I. Park, C. K. Jeong, N. K. Kim and K. J. Lee, *Nano Converg*, 2016, **3**, 12.
31. C. L. Choong, M. B. Shim, B. S. Lee, S. Jeon, D. S. Ko, T. H. Kang, J. Bae, S. H. Lee, K. E. Byun, J. Im, Y. J. Jeong, C. E. Park, J. J. Park and U. I. Chung, *Adv Mater*, 2014, **26**, 3451-3458.
32. X. Huang, Y. H. Liu, H. Y. Cheng, W. J. Shin, J. A. Fan, Z. J. Liu, C. J. Lu, G. W. Kong, K. Chen, D. Patnaik, S. H. Lee, S. Hage-Ali, Y. G. Huang and J. A. Rogers, *Adv Funct Mater*, 2014, **24**, 3846-3854.
33. B. U. Hwang, J. H. Lee, T. Q. Trung, E. Roh, D. I. Kim, S. W. Kim and N. E. Lee, *Acs Nano*, 2015, **9**, 8801-8810.
34. E. Roh, B. U. Hwang, D. Kim, B. Y. Kim and N. E. Lee, *Acs Nano*, 2015, **9**, 6252-6261.
35. T. Someya, T. Sekitani, S. Iba, Y. Kato, H. Kawaguchi and T. Sakurai, *P Natl Acad Sci USA*, 2004, **101**, 9966-9970.
36. J. H. Park, J. Seo, C. Kim, D. J. Joe, H. E. Lee, T. H. Im, J. Y. Seok, C. K. Jeong, B. S. Ma, H. K. Park, T. S. Kim and K. J. Lee, *Adv Sci (Weinh)*, 2018, **5**, 1801146.
37. R. Ma, B. Kang, S. Cho, M. Choi and S. Baik, *Acs Nano*, 2015, **9**, 10876-10886.
38. T. Yamada, Y. Hayamizu, Y. Yamamoto, Y. Yomogida, A. Izadi-Najafabadi, D. N. Futaba and K. Hata, *Nat Nanotechnol*, 2011, **6**, 296-301.
39. K. L. Lin, J. Chae and K. Jain, *IEEE T Adv Packaging*, 2010, **33**, 592-601.
40. D. H. Kim, N. S. Lu, R. Ma, Y. S. Kim, R. H. Kim, S. D. Wang, J. Wu, S. M. Won, H. Tao, A. Islam, K. J. Yu, T. I. Kim, R. Chowdhury, M. Ying, L. Z. Xu, M. Li, H. J. Chung, H. Keum, M. McCormick, P. Liu, Y. W. Zhang, F. G. Omenetto, Y. G. Huang, T. Coleman and J. A. Rogers, *Science*, 2011, **333**, 838-843.
41. M. Gonzalez, F. Axisa, M. V. Bulcke, D. Brosteaux, B. Vandeveld and J. Vanfleteren, *Microelectron Reliab*, 2008, **48**, 825-832.
42. M. Kaltenbrunner, T. Sekitani, J. Reeder, T. Yokota, K. Kuribara, T. Tokuhara, M. Drack, R. Schwodiauer, I. Graz, S. Bauer-Gogonea, S. Bauer and T. Someya, *Nature*, 2013, **499**, 458-463.
43. D. J. Lipomi and Z. A. Bao, *Energ Environ Sci*, 2011, **4**, 3314-3328.
44. N. Bowden, S. Brittain, A. G. Evans, J. W. Hutchinson and G. M. Whitesides, *Nature*, 1998, **393**, 146-149.
45. C. Dagdeviren, Y. Shi, P. Joe, R. Ghaffari, G. Balooch, K. Usgaonkar, O. Gur, P. L. Tran, J. R. Crosby, M. Meyer, Y. W. Su, R. C. Webb, A. S. Tedesco, M. J. Slepian, Y. G. Huang and J. A. Rogers, *Nat Mater*, 2015, **14**, 728-736.
46. J. J. Liang, L. Li, D. Chen, T. Hajagos, Z. Ren, S. Y. Chou, W. Hu and Q. B. Pei, *Nat Commun*, 2015, **6**, 7647.
47. P. Lee, J. Lee, H. Lee, J. Yeo, S. Hong, K. H. Nam, D. Lee, S. S. Lee and S. H. Ko, *Adv Mater*, 2012, **24**, 3326-3332.
48. T. Q. Trung and N. E. Lee, *Adv Mater*, 2017, **29**, 1603167.
49. J. Y. Oh, S. Rondeau-Gagne, Y. C. Chiu, A. Chortos, F. Lissel, G. J. N. Wang, B. C. Schroeder, T. Kurosawa, J. Lopez, T. Katsumata, J. Xu, C. X. Zhu, X. D. Gu, W. G. Bae, Y. Kim, L. H. Jin, J. W. Chung, J. B. H. Tok and Z. N. Bao, *Nature*, 2016, **539**, 411-415.
50. S. J. Benight, C. Wang, J. B. H. Tok and Z. A. Bao, *Prog Polym Sci*, 2013, **38**, 1961-1977.
51. J. A. Rogers, T. Someya and Y. G. Huang, *Science*, 2010, **327**, 1603-1607.
52. Y. Kim, J. Zhu, B. Yeom, M. Di Prima, X. L. Su, J. G. Kim, S. J. Yoo, C. Uher and N. A. Kotov, *Nature*, 2013, **500**, 59-63.
53. R. Ma, J. Lee, D. Choi, H. Moon and S. Baik, *Nano Lett*, 2014,

- 14, 1944-1951.
54. R. H. Kim, M. H. Bae, D. G. Kim, H. Y. Cheng, B. H. Kim, D. H. Kim, M. Li, J. Wu, F. Du, H. S. Kim, S. Kim, D. Estrada, S. W. Hong, Y. G. Huang, E. Pop and J. A. Rogers, *Nano Lett*, 2011, **11**, 3881-3886.
55. S. I. Park, Y. J. Xiong, R. H. Kim, P. Elvikis, M. Meitl, D. H. Kim, J. Wu, J. Yoon, C. J. Yu, Z. J. Liu, Y. G. Huang, K. Hwang, P. Ferreira, X. L. Li, K. Choquette and J. A. Rogers, *Science*, 2009, **325**, 977-981.
56. M. S. White, M. Kaltenbrunner, E. D. Glowacki, K. Gutnichenko, G. Kettlgruber, I. Graz, S. Aazou, C. Ulbricht, D. A. M. Egbe, M. C. Miron, Z. Major, M. C. Scharber, T. Sekitani, T. Someya, S. Bauer and N. S. Sariciftci, *Nat Photonics*, 2013, **7**, 811-816.
57. M. B. Schubert and J. H. Werner, *Mater Today*, 2006, **9**, 42-50.
58. D. Son, J. Lee, S. Qiao, R. Ghaffari, J. Kim, J. E. Lee, C. Song, S. J. Kim, D. J. Lee, S. W. Jun, S. Yang, M. Park, J. Shin, K. Do, M. Lee, K. Kang, C. S. Hwang, N. S. Lu, T. Hyeon and D. H. Kim, *Nat Nanotechnol*, 2014, **9**, 397-404.
59. I. You, B. Kim, J. Park, K. Koh, S. Shin, S. Jung and U. Jeong, *Adv Mater*, 2016, **28**, 6359-6364.
60. A. Pantelopoulou and N. G. Bourbakis, *IEEE T Syst Man Cy C*, 2010, **40**, 1-12.
61. Z. B. Yu, Q. W. Zhang, L. Li, Q. Chen, X. F. Niu, J. Liu and Q. B. Pei, *Adv Mater*, 2011, **23**, 664-668.
62. F. Xu and Y. Zhu, *Adv Mater*, 2012, **24**, 5117-5122.
63. M. Amjadi, A. Pichitpajongkit, S. Lee, S. Ryu and I. Park, *Acs Nano*, 2014, **8**, 5154-5163.
64. D. J. Lipomi, M. Vosgueritchian, B. C. K. Tee, S. L. Hellstrom, J. A. Lee, C. H. Fox and Z. N. Bao, *Nat Nanotechnol*, 2011, **6**, 788-792.
65. L. Xiao, Z. Chen, C. Feng, L. Liu, Z. Q. Bai, Y. Wang, L. Qian, Y. Y. Zhang, Q. Q. Li, K. L. Jiang and S. S. Fan, *Nano Lett*, 2008, **8**, 4539-4545.
66. K. S. Kim, Y. Zhao, H. Jang, S. Y. Lee, J. M. Kim, K. S. Kim, J. H. Ahn, P. Kim, J. Y. Choi and B. H. Hong, *Nature*, 2009, **457**, 706-710.
67. Z. P. Chen, W. C. Ren, L. B. Gao, B. L. Liu, S. F. Pei and H. M. Cheng, *Nat Mater*, 2011, **10**, 424-428.
68. B. O'Brien, J. Thode, I. Anderson, E. Calius, E. Haemmerle and S. Xie, *Proc Spie*, 2007, **6524**, 652415.
69. B. L. Groenendaal, F. Jonas, D. Freitag, H. Pielartzik and J. R. Reynolds, *Adv Mater*, 2000, **12**, 481-494.
70. A. G. MacDiarmid, *Angew Chem Int Edit*, 2001, **40**, 2581-2590.
71. J. Park, S. D. Wang, M. Li, C. Ahn, J. K. Hyun, D. S. Kim, D. K. Kim, J. A. Rogers, Y. G. Huang and S. Jeon, *Nat Commun*, 2012, **3**, 916.
72. C. Keplinger, J. Y. Sun, C. C. Foo, P. Rothmund, G. M. Whitesides and Z. G. Suo, *Science*, 2013, **341**, 984-987.
73. J. Y. Sun, C. Keplinger, G. M. Whitesides and Z. G. Suo, *Adv Mater*, 2014, **26**, 7608-7614.
74. E. C. Garnett, W. S. Cai, J. J. Cha, F. Mahmood, S. T. Connor, M. G. Christoforo, Y. Cui, M. D. McGehee and M. L. Brongersma, *Nat Mater*, 2012, **11**, 241-249.
75. L. B. Hu, H. S. Kim, J. Y. Lee, P. Peumans and Y. Cui, *Acs Nano*, 2010, **4**, 2955-2963.
76. S. Sorel, D. Bellet and J. N. Coleman, *Acs Nano*, 2014, **8**, 4805-4814.
77. L. Li, Z. B. Yu, W. L. Hu, C. H. Chang, Q. Chen and Q. B. Pei, *Adv Mater*, 2011, **23**, 5563-5567.
78. R. Zhu, C. H. Chung, K. C. Cha, W. B. Yang, Y. B. Zheng, H. P. Zhou, T. B. Song, C. C. Chen, P. S. Weiss, G. Li and Y. Yang, *Acs Nano*, 2011, **5**, 9877-9882.
79. A. Kumar and C. W. Zhou, *Acs Nano*, 2010, **4**, 11-14.
80. W. L. Hu, X. F. Niu, L. Li, S. R. Yun, Z. B. Yu and Q. B. Pei, *Nanotechnology*, 2012, **23**, 344002.
81. J. V. van de Groep, P. Spinelli and A. Polman, *Nano Lett*, 2012, **12**, 3138-3144.
82. C. H. Chung, T. B. Song, B. Bob, R. Zhu, H. S. Duan and Y. Yang, *Adv Mater*, 2012, **24**, 5499-5504.
83. C. H. Kim, S. H. Cha, S. C. Kim, M. Song, J. Lee, W. S. Shin, S. J. Moon, J. H. Bahng, N. A. Kotov and S. H. Jin, *Acs Nano*, 2011, **5**, 3319-3325.
84. S. Hong, H. Lee, J. Lee, J. Kwon, S. Han, Y. D. Suh, H. Cho, J. Shin, J. Yeo and S. H. Ko, *Adv Mater*, 2015, **27**, 4744-4751.
85. T. Akter and W. S. Kim, *Acs Appl Mater Inter*, 2012, **4**, 1855-1859.
86. C. Lee, Y. Oh, I. S. Yoon, S. H. Kim, B. K. Ju and J. M. Hong, *Sci Rep-Uk*, 2018, **8**, 2763.
87. Y. Yang, S. Ding, T. Araki, J. T. Jiu, T. Sugahara, J. Wang, J. Vanfleteren, T. Sekitani and K. Suganuma, *Nano Res*, 2016, **9**, 401-414.
88. Z. B. Yu, L. Li, Q. W. Zhang, W. L. Hu and Q. B. Pei, *Adv Mater*, 2011, **23**, 4453-4457.
89. L. Li, J. J. Liang, S. Y. Chou, X. D. Zhu, X. F. Niu, Z. B. Yu and Q. B. Pei, *Sci Rep-Uk*, 2014, **4**, 4307.
90. L. Li, Z. B. Yu, C. H. Chang, W. L. Hu, X. F. Niu, Q. Chen and Q. B. Pei, *Phys Chem Chem Phys*, 2012, **14**, 14249-14254.
91. D. Chen, J. J. Liang, C. Liu, G. Saldanha, F. C. Zhao, K. Tong, J. Liu and Q. B. Pei, *Adv Funct Mater*, 2015, **25**, 7512-7520.
92. S. Yun, X. F. Niu, Z. B. Yu, W. L. Hu, P. Brochu and Q. B. Pei, *Adv Mater*, 2012, **24**, 1321-1327.
93. W. L. Hu, X. F. Niu, R. Zhao and Q. B. Pei, *Appl Phys Lett*, 2013, **102**, 083303.
94. C. K. Gong, J. J. Liang, W. Hu, X. F. Niu, S. W. Ma, H. T. Hahn and Q. B. Pei, *Adv Mater*, 2013, **25**, 4186-4191.
95. J. P. Li, S. H. Qi, J. J. Liang, L. Li, Y. Xiong, W. Hu and Q. B. Pei, *Acs Appl Mater Inter*, 2015, **7**, 14140-14149.
96. W. Yuan, L. B. Hu, Z. B. Yu, T. L. Lam, J. Biggs, S. M. Ha, D. J. Xi, B. Chen, M. K. Senesky, G. Gruner and Q. B. Pei, *Advanced Materials*, 2008, **20**, 621-+.
97. Y. Li, S. S. Chen, M. C. Wu and J. Q. Sun, *Adv Mater*, 2012, **24**, 4578-4582.
98. B. J. Blaiszik, S. L. B. Kramer, S. C. Olugebefola, J. S. Moore, N. R. Sottos and S. R. White, *Annu Rev Mater Res*, 2010, **40**, 179-211.
99. Q. Wang, J. L. Mynar, M. Yoshida, E. Lee, M. Lee, K. Okuro, K. Kinbara and T. Aida, *Nature*, 2010, **463**, 339-343.
100. B. C. K. Tee, C. Wang, R. Allen and Z. N. Bao, *Nat Nanotechnol*, 2012, **7**, 825-832.
101. H. Sun, X. You, Y. S. Jiang, G. Z. Guan, X. Fang, J. Deng, P. N. Chen, Y. F. Luo and H. S. Peng, *Angew Chem Int Edit*, 2014, **53**, 9526-9531.
102. H. Wang, B. W. Zhu, W. C. Jiang, Y. Yang, W. R. Leow, H. Wang and X. D. Chen, *Adv Mater*, 2014, **26**, 3638-3643.
103. J. S. Bae, Y. S. Lee, J. P. Li, J. J. Liang, D. Chen, Q. B. Pei and S. B. Lee, *Adv Mater Technol-Uk*, 2018, **3**, 1700364.
104. J. Y. Lee, S. T. Connor, Y. Cui and P. Peumans, *Nano Lett*, 2008, **8**, 689-692.
105. W. Hu, R. Wang, Y. Lu and Q. Pei, *J. Mater. Chem. C*, 2014, **2**, 1298-1305.
106. S. Soltanian, R. Rahmadian, B. Gholamkhash, N. M. Kiasari,

- F. Ko and P. Servati, *Adv Energy Mater*, 2013, **3**, 1332-1337.
107. F. Carpi, P. Chiarelli, A. Mazzoldi and D. De Rossi, *Sensor Actuat a-Phys*, 2003, **107**, 85-95.
108. L. Gorton, *Electroanal*, 1995, **7**, 23-45.
109. X. F. Niu, H. Stoyanov, W. Hu, R. Leo, P. Brochu and Q. B. Pei, *J Polym Sci Pol Phys*, 2013, **51**, 197-206.
110. A. O'Halloran, F. O'Malley and P. McHugh, *J Appl Phys*, 2008, **104**, 071101.
111. E. Biddiss and T. Chau, *Med Eng Phys*, 2008, **30**, 403-418.
112. L. B. Hu, W. Yuan, P. Brochu, G. Gruner and Q. B. Pei, *Appl Phys Lett*, 2009, **94**, 161108.
113. P. Brochu, H. Stoyanov, R. Chang, X. F. Niu, W. Hu and Q. B. Pei, *Adv Energy Mater*, 2014, **4**, 1300659.
114. C. Feng, K. Liu, J. S. Wu, L. Liu, J. S. Cheng, Y. Y. Zhang, Y. H. Sun, Q. Q. Li, S. S. Fan and K. L. Jiang, *Adv Funct Mater*, 2010, **20**, 885-891.
115. T. Chen, H. S. Peng, M. Durstock and L. M. Dai, *Sci Rep-Uk*, 2014, **4**, 3612.
116. M. Zhang, S. L. Fang, A. A. Zakhidov, S. B. Lee, A. E. Aliev, C. D. Williams, K. R. Atkinson and R. H. Baughman, *Science*, 2005, **309**, 1215-1219.
117. K. Liu, Y. H. Sun, P. Liu, X. Y. Lin, S. S. Fan and K. L. Jiang, *Adv Funct Mater*, 2011, **21**, 2721-2728.
118. S. K. Lee, B. J. Kim, H. Jang, S. C. Yoon, C. Lee, B. H. Hong, J. A. Rogers, J. H. Cho and J. H. Ahn, *Nano Lett*, 2011, **11**, 4642-4646.
119. M. S. Lee, K. Lee, S. Y. Kim, H. Lee, J. Park, K. H. Choi, H. K. Kim, D. G. Kim, D. Y. Lee, S. Nam and J. U. Park, *Nano Lett*, 2013, **13**, 2814-2821.
120. U. Kim, J. Kang, C. Lee, H. Y. Kwon, S. Hwang, H. Moon, J. C. Koo, J. D. Nam, B. H. Hong, J. B. Choi and H. R. Choi, *Nanotechnology*, 2013, **24**, 145501.
121. Z. Y. Liu, K. Parvez, R. J. Li, R. H. Dong, X. L. Feng and K. Mullen, *Adv Mater*, 2015, **27**, 669-675.
122. N. Liu, A. Chortos, T. Lei, L. H. Jin, T. R. Kim, W. G. Bae, C. X. Zhu, S. H. Wang, R. Pfattner, X. Y. Chen, R. Sinclair and Z. A. Bao, *Sci Adv*, 2017, **3**, e1700159.
123. X. Crispin, F. L. E. Jakobsson, A. Crispin, P. C. M. Grim, P. Andersson, A. Volodin, C. van Haesendonck, M. Van der Auweraer, W. R. Salaneck and M. Berggren, *Chem Mater*, 2006, **18**, 4354-4360.
124. D. J. Lipomi, J. A. Lee, M. Vosgueritchian, B. C. K. Tee, J. A. Bolander and Z. A. Bao, *Chem Mater*, 2012, **24**, 373-382.
125. M. Dobbelin, R. Marcilla, M. Salsamendi, C. Pozo-Gonzalo, P. M. Carrasco, J. A. Pomposo and D. Mecerreyes, *Chem Mater*, 2007, **19**, 2147-2149.
126. C. Badre, L. Marquant, A. M. Alsayed and L. A. Hough, *Adv Funct Mater*, 2012, **22**, 2723-2727.
127. B. H. Fan, X. G. Mei and J. Y. Ouyang, *Macromolecules*, 2008, **41**, 5971-5973.
128. Y. J. Xia, H. M. Zhang and J. Y. Ouyang, *J Mater Chem*, 2010, **20**, 9740-9747.
129. Y. Y. Lee, J. H. Lee, J. Y. Cho, N. R. Kim, D. H. Nam, I. S. Choi, K. T. Nam and Y. C. Joo, *Adv Funct Mater*, 2013, **23**, 4020-4027.
130. C. Teng, X. Y. Lu, Y. Zhu, M. X. Wan and L. Jiang, *Rsc Adv*, 2013, **3**, 7219-7223.
131. H. E. Yin, C. H. Wu, K. S. Kuo, W. Y. Chiu and H. J. Tai, *J Mater Chem*, 2012, **22**, 3800-3810.
132. U. Lang, N. Naujoks and J. Dual, *Synthetic Met*, 2009, **159**, 473-479.
133. Y. Y. Lee, H. Y. Kang, S. H. Gwon, G. M. Choi, S. M. Lim, J. Y. Sun and Y. C. Joo, *Adv Mater*, 2016, **28**, 1636-1643.
134. M. Y. Teo, N. Kim, S. Kee, B. S. Kim, G. Kim, S. Hong, S. Jung and K. Lee, *Acs Appl Mater Inter*, 2017, **9**, 819-826.
135. Y. Wang, C. X. Zhu, R. Pfattner, H. P. Yan, L. H. Jin, S. C. Chen, F. Molina-Lopez, F. Lissel, J. Liu, N. I. Rabiah, Z. Chen, J. W. Chung, C. Linder, M. F. Toney, B. Murmann and Z. Bao, *Sci Adv*, 2017, **3**, e1602076.
136. M. D. Dickey, *Adv Mater*, 2017, **29**, 1606425.
137. M. D. Dickey, *Acs Appl Mater Inter*, 2014, **6**, 18369-18379.
138. S. Zhu, J. H. So, R. Mays, S. Desai, W. R. Barnes, B. Pourdeyhimi and M. D. Dickey, *Adv Funct Mater*, 2013, **23**, 2308-2314.
139. A. C. Siegel, D. A. Bruzewicz, D. B. Weibel and G. M. Whitesides, *Adv Mater*, 2007, **19**, 727-733.
140. K. Entesari and A. P. Saghati, *Ieee Microw Mag*, 2016, **17**, 50-75.
141. S. Cheng and Z. G. Wu, *Lab Chip*, 2012, **12**, 2782-2791.
142. Q. Zhang, D. J. Roach, L. C. Geng, H. S. Chen, H. J. Qi and D. N. Fang, *Smart Mater Struct*, 2018, **27**, 035019.
143. S. W. Jin, J. Park, S. Y. Hong, H. Park, Y. R. Jeong, J. Park, S. S. Lee and J. S. Ha, *Sci Rep-Uk*, 2015, **5**, 11695.
144. Y. S. Xie, S. Xu, Z. L. Xu, H. C. Wu, C. Deng and X. W. Wang, *Carbon*, 2016, **98**, 381-390.
145. K. J. Henderson, T. C. Zhou, K. J. Otton and K. R. Shull, *Macromolecules*, 2010, **43**, 6193-6201.
146. D. Mawad, E. Stewart, D. L. Officer, T. Romeo, P. Wagner, K. Wagner and G. G. Wallace, *Adv Funct Mater*, 2012, **22**, 2692-2699.
147. X. Y. Ma, W. P. Cai, S. Zhang, J. H. Guo, X. Peng, Z. T. Qiu, J. Ying and J. K. Wang, *New J Chem*, 2018, **42**, 692-698.
148. Q. Wu, J. J. Wei, B. Xu, X. H. Liu, H. B. Wang, W. Wang, Q. G. Wang and W. G. Liu, *Sci Rep-Uk*, 2017, **7**, 41566.
149. M. Kaltenbrunner, M. S. White, E. D. Glowacki, T. Sekitani, T. Someya, N. S. Sariciftci and S. Bauer, *Nat Commun*, 2012, **3**, 770.
150. S. Xu, Z. Yan, K. I. Jang, W. Huang, H. Fu, J. Kim, Z. Wei, M. Flavin, J. McCracken, R. Wang, A. Badea, Y. Liu, D. Xiao, G. Zhou, J. Lee, H. U. Chung, H. Cheng, W. Ren, A. Banks, X. Li, U. Paik, R. G. Nuzzo, Y. Huang, Y. Zhang and J. A. Rogers, *Science*, 2015, **347**, 154-159.
151. S. Xu, Y. Zhang, J. Cho, J. Lee, X. Huang, L. Jia, J. A. Fan, Y. Su, J. Su, H. Zhang, H. Cheng, B. Lu, C. Yu, C. Chuang, T. I. Kim, T. Song, K. Shigeta, S. Kang, C. Dagdeviren, I. Petrov, P. V. Braun, Y. Huang, U. Paik and J. A. Rogers, *Nat Commun*, 2013, **4**, 1543.
152. M. Isobe and K. Okumura, *Sci Rep-Uk*, 2016, **6**, 24758.
153. A. Lamoureux, K. Lee, M. Shlian, S. R. Forrest and M. Shtein, *Nat Commun*, 2015, **6**, 8092.
154. T. C. Shyu, P. F. Damasceno, P. M. Dodd, A. Lamoureux, L. Xu, M. Shlian, M. Shtein, S. C. Glotzer and N. A. Kotov, *Nat Mater*, 2015, **14**, 785-789.
155. S. Savagatrup, D. Rodriguez, A. D. Printz, A. B. Sieval, J. C. Hummelen and D. J. Lipomi, *Chem Mater*, 2015, **27**, 3902-3911.
156. S. Savagatrup, A. S. Makaram, D. J. Burke and D. J. Lipomi, *Adv Funct Mater*, 2014, **24**, 1169-1181.
157. S. Savagatrup, A. D. Printz, H. S. Wu, K. M. Rajan, E. J. Sawyer, A. V. Zaretski, C. J. Bettinger and D. J. Lipomi, *Synthetic Met*, 2015, **203**, 208-214.
158. L. Li, J. Liang, H. Gao, Y. Li, X. Niu, X. Zhu, Y. Xiong and Q. Pei, *ACS Applied Materials and Interfaces*, 2017, **9**, 40523-40532.

159. T. Kim, J. H. Kim, T. E. Kang, C. Lee, H. Kang, M. Shin, C. Wang, B. Ma, U. Jeong, T. S. Kim and B. J. Kim, *Nat Commun*, 2015, **6**, 8547.
160. Z. Yu, X. Niu, Z. Liu and Q. Pei, *Adv Mater*, 2011, **23**, 3989-3994.
161. A. Chortos, J. Lim, J. W. To, M. Vosgueritchian, T. J. Dusseault, T. H. Kim, S. Hwang and Z. Bao, *Adv Mater*, 2014, **26**, 4253-4259.
162. A. Chortos, G. I. Koleilat, R. Pfattner, D. Kong, P. Lin, R. Nur, T. Lei, H. Wang, N. Liu, Y. C. Lai, M. G. Kim, J. W. Chung, S. Lee and Z. Bao, *Adv Mater*, 2016, **28**, 4441-4448.
163. H. C. Wu, S. J. Benight, A. Chortos, W. Y. Lee, J. Mei, J. W. F. To, C. Lu, M. He, J. B. H. Tok, W. C. Chen and Z. Bao, *Chem Mater*, 2014, **26**, 4544-4551.
164. J. Xu, S. H. Wang, G. J. N. Wang, C. X. Zhu, S. C. Luo, L. H. Jin, X. D. Gu, S. C. Chen, V. R. Feig, J. W. F. To, S. Rondeau-Gagne, J. Park, B. C. Schroeder, C. Lu, J. Y. Oh, Y. M. Wang, Y. H. Kim, H. Yan, R. Sinclair, D. S. Zhou, G. Xue, B. Murmann, C. Linder, W. Cai, J. B. H. Tok, J. W. Chung and Z. N. Bao, *Science*, 2017, **355**, 59-64.
165. F. Liu, Y. Gu, J. W. Jung, W. H. Jo and T. P. Russell, *Journal of Polymer Science, Part B: Polymer Physics*, 2012, **50**, 1018-1044.
166. B. O'Connor, R. J. Kline, B. R. Conrad, L. J. Richter, D. Gundlach, M. F. Toney and D. M. DeLongchamp, *Adv Funct Mater*, 2011, **21**, 3697-3705.
167. R. Peng, B. Pang, D. Hu, M. Chen, G. Zhang, X. Wang, H. Lu, K. Cho and L. Qiu, *J. Mater. Chem. C*, 2015, **3**, 3599-3606.
168. C. Müller, S. Goffri, D. W. Breiby, J. W. Andreasen, H. D. Chanzy, R. A. J. Janssen, M. M. Nielsen, C. P. Radano, H. Sirringhaus, P. Smith and N. Stingelin-Stutzmann, *Adv Funct Mater*, 2007, **17**, 2674-2679.
169. D. J. Lipomi, H. Chong, M. Vosgueritchian, J. G. Mei and Z. A. Bao, *Sol Energ Mat Sol C*, 2012, **107**, 355-365.
170. H. Gao, S. Chen, J. Liang and Q. Pei, *ACS Applied Materials and Interfaces*, 2016, **8**, 32504-32511.
171. E. Song, B. Kang, H. H. Choi, D. H. Sin, H. Lee, W. H. Lee and K. Cho, *Adv Electron Mater*, 2016, **2**, 1500250.
172. D. Choi, H. Kim, N. Persson, P. H. Chu, M. Chang, J. H. Kang, S. Graham and E. Reichmanis, *Chem Mater*, 2016, **28**, 1196-1204.
173. A. J. Granero, P. Wagner, K. Wagner, J. M. Razal, G. G. Wallace and M. In Het Panhuis, *Adv Funct Mater*, 2011, **21**, 955-962.
174. Z. B. Yu, M. L. Wang, G. T. Lei, J. Liu, L. Li and Q. B. Pei, *J Phys Chem Lett*, 2011, **2**, 367-372.
175. Z. B. Yu, M. L. Sun and Q. B. Pei, *J Phys Chem B*, 2009, **113**, 8481-8486.
176. Y. Shao, G. C. Bazan and A. J. Heeger, *Adv Mater*, 2007, **19**, 365-370.
177. P. Matyba, H. Yamaguchi, G. Eda, M. Chhowalla, L. Edman and N. D. Robinson, *Acs Nano*, 2010, **4**, 637-642.
178. B. O'Connor, E. P. Chan, C. Chan, B. R. Conrad, L. J. Richter, R. J. Kline, M. Heeney, I. McCulloch, C. L. Soles and D. M. DeLongchamp, *Acs Nano*, 2010, **4**, 7538-7544.
179. H. C. Wu, C. C. Hung, C. W. Hong, H. S. Sun, J. T. Wang, G. Yamashita, T. Higashihara and W. C. Chen, *Macromolecules*, 2016, **49**, 8540-8548.
180. M. L. Hammock, A. Chortos, B. C. K. Tee, J. B. H. Tok and Z. A. Bao, *Adv Mater*, 2013, **25**, 5997-6037.
181. M. Gsänger, D. Bialas, L. Huang, M. Stolte and F. Würthner, *Adv Mater*, 2016, **28**, 3615-3645.
182. H. F. Wen, H. C. Wu, J. Aimi, C. C. Hung, Y. C. Chiang, C. C. Kuo and W. C. Chen, *Macromolecules*, 2017, **50**, 4982-4992.
183. W. Zhao, T. Cao and J. M. White, *Adv Funct Mater*, 2004, **14**, 783-790.
184. A. R. Davis, J. A. Maegerlein and K. R. Carter, *Journal of the American Chemical Society*, 2011, **133**, 20546-20551.
185. G. J. N. Wang, L. Shaw, J. Xu, T. Kurosawa, B. C. Schroeder, J. Y. Oh, S. J. Benight and Z. Bao, *Adv Funct Mater*, 2016, **26**, 7254-7262.
186. J. Li, Y. Zhao, H. S. Tan, Y. Guo, C. A. Di, G. Yu, Y. Liu, M. Lin, S. H. Lim, Y. Zhou, H. Su and B. S. Ong, *Sci Rep-Uk*, 2012, **2**, 754.
187. I. Kang, H. J. Yun, D. S. Chung, S. K. Kwon and Y. H. Kim, *Journal of the American Chemical Society*, 2013, **135**, 14896-14899.
188. H. R. Tseng, L. Ying, B. B. Y. Hsu, L. A. Perez, C. J. Takacs, G. C. Bazan and A. J. Heeger, *Nano Lett*, 2012, **12**, 6353-6357.
189. B. Nketia-Yawson, H. S. Lee, D. Seo, Y. Yoon, W. T. Park, K. Kwak, H. J. Son, B. Kim and Y. Y. Noh, *Adv Mater*, 2015, **27**, 3045-3052.
190. L. Qiu, X. Wang, W. H. Lee, J. A. Lim, J. S. Kim, D. Kwak and K. Cho, *Chem Mater*, 2009, **21**, 4380-4386.
191. G. Lu, H. Tang, Y. Qu, G. Li and X. Yang, *Macromolecules*, 2007, **40**, 6579-6584.
192. H. J. Kim, K. Sim, A. Thukral and C. Yu, *Sci Adv*, 2017, **3**, e1701114.
193. M. Shin, J. Y. Oh, K. E. Byun, Y. J. Lee, B. Kim, H. K. Baik, J. J. Park and U. Jeong, *Adv Mater*, 2015, **27**, 1255-1261.
194. Y. Lee, J. Y. Oh, S. Y. Son, T. Park and U. Jeong, *ACS Applied Materials and Interfaces*, 2015, **7**, 27694-27702.
195. Y. Lee, H. Y. Zhou and T. W. Lee, *Journal of Materials Chemistry C*, 2018, **6**, 3538-3550.
196. Y. Lee, J. Y. Oh, T. R. Kim, X. D. Gu, Y. Kim, G. J. N. Wang, H. C. Wu, R. Pfattner, J. W. F. To, T. Katsumata, D. Son, J. Kang, J. R. Matthews, W. J. Niu, M. Q. He, R. Sinclair, Y. Cui, J. B. H. Tok, T. W. Lee and Z. N. Bao, *Adv Mater*, 2018, **30**, 1704401.
197. M. Shin, J. H. Song, G. H. Lim, B. Lim, J. J. Park and U. Jeong, *Adv Mater*, 2014, **26**, 3706-3711.
198. M. Y. Lee, J. Hong, E. K. Lee, H. Yu, H. Kim, J. U. Lee, W. Lee and J. H. Oh, *Adv Funct Mater*, 2016, **26**, 1445-1453.
199. S. Raspopovic, M. Capogrosso, F. M. Petrini, M. Bonizzato, J. Rigosa, G. Di Pino, J. Carpaneto, M. Controzzi, T. Boretius and E. Fernandez, *Science translational medicine*, 2014, **6**, 222ra219.
200. J. Kim, M. Lee, H. J. Shim, R. Ghaffari, H. R. Cho, D. Son, Y. H. Jung, M. Soh, C. Choi and S. Jung, *Nat Commun*, 2014, **5**, 5747.
201. P. Maiolino, M. Maggiali, G. Cannata, G. Metta and L. Natale, *IEEE Sens J*, 2013, **13**, 3910-3917.
202. T. Sekitani, Y. Noguchi, K. Hata, T. Fukushima, T. Aida and T. Someya, *Science*, 2008, **321**, 1468-1472.
203. V. J. Lumelsky, M. S. Shur and S. Wagner, *IEEE Sens J*, 2001, **1**, 41-51.
204. W. Roentgen, *Ann. Phys. Chem*, 1880, **11**, 771-786.
205. P. H. Vargantwar, A. E. Özçam, T. K. Ghosh and R. J. Spontak, *Advanced Functional Materials*, 2012, **22**, 2100-2113.
206. F. Carpi, I. Anderson, S. Bauer, G. Frediani, G. Gallone, M. Gei, C. Graaf, C. Jean-Mistral, W. Kaal and G. Kofod, *Smart Materials and Structures*, 2015, **24**, 105025.
207. D. Chen and Q. Pei, *Chemical reviews*, 2017, **117**, 11239-11268.

208. M. Kaltenbrunner, T. Sekitani, J. Reeder, T. Yokota, K. Kuribara, T. Tokuhara, M. Drack, R. Schwödiauer, I. Graz and S. Bauer-Gogonea, *Nature*, 2013, **499**, 458.
209. S. Wang, J. Xu, W. Wang, G.-J. N. Wang, R. Rastak, F. Molina-Lopez, J. W. Chung, S. Niu, V. R. Feig and J. Lopez, *Nature*, 2018, **555**, 83.
210. X. Shuai, P. Zhu, W. Zeng, Y. Hu, X. Liang, Y. Zhang, R. Sun and C. P. Wong, *ACS Appl Mater Interfaces*, 2017, **9**, 26314-26324.
211. S. Ji, J. Jang, E. Cho, S. H. Kim, E. S. Kang, J. Kim, H. K. Kim, H. Kong, S. K. Kim, J. Y. Kim and J. U. Park, *Adv Mater*, 2017, **29**, 1700538.
212. Q. Pei, M. A. Rosenthal, R. Pelrine, S. Stanford and R. D. Kornbluh, 2003.
213. J. Zhao, J. Niu, D. McCoul, J. Leng and Q. Pei, *Meccanica*, 2015, **50**, 2815-2824.
214. D. Rus and M. T. Tolley, *Nature*, 2015, **521**, 467.
215. M. Duduta, D. R. Clarke and R. J. Wood, 2017.
216. Y. Bar-Cohen, X. Niu, F. Carpi, P. Brochu, B. Salazar and Q. Pei, 2011, **7976**, 797610.
217. D. Yurchenko, Z. H. Lai, G. Thomson, D. V. Val and R. V. Bobryk, *Applied Energy*, 2017, **208**, 456-470.
218. S. Yang, X. Zhao and P. Sharma, *Soft Matter*, 2017, **13**, 4552-4558.
219. P. Brochu, H. Stoyanov, R. Chang, X. Niu, W. Hu and Q. Pei, *Advanced Energy Materials*, 2014, **4**, 1300659.
220. S. Li, J. Wang, W. Peng, L. Lin, Y. Zi, S. Wang, G. Zhang and Z. L. Wang, *Advanced Energy Materials*, 2017, **7**, 1602832.
221. X. Chen, X. Pu, T. Jiang, A. Yu, L. Xu and Z. L. Wang, *Advanced Functional Materials*, 2017, **27**, 1603788.
222. X. Pu, M. Liu, X. Chen, J. Sun, C. Du, Y. Zhang, J. Zhai, W. Hu and Z. L. Wang, *Science advances*, 2017, **3**, e1700015.
223. Z. Yu, W. Yuan, P. Brochu, B. Chen, Z. Liu and Q. Pei, *Applied Physics Letters*, 2009, **95**, 192904.
224. X. Niu, X. Yang, P. Brochu, H. Stoyanov, S. Yun, Z. Yu and Q. Pei, *Advanced Materials*, 2012, **24**, 6513-6519.
225. Y. Bar-Cohen, X. Niu, P. Brochu, H. Stoyanov, S. R. Yun and Q. Pei, 2012, **8340**, 83400R.
226. Y. Bar-Cohen, Z. Ren, X. Niu, D. Chen, W. Hu and Q. Pei, 2014, **9056**, 905621.
227. F. Carpi, G. Frediani, S. Turco and D. De Rossi, *Advanced Functional Materials*, 2011, **21**, 4152-4158.
228. D. H. Kim, J. Xiao, J. Song, Y. Huang and J. A. Rogers, *Advanced Materials*, 2010, **22**, 2108-2124.
229. D. Y. Khang, J. A. Rogers and H. H. Lee, *Advanced Functional Materials*, 2009, **19**, 1526-1536.
230. J. A. Rogers, T. Someya and Y. Huang, *science*, 2010, **327**, 1603-1607.
231. D.-H. Kim, J. Song, W. M. Choi, H.-S. Kim, R.-H. Kim, Z. Liu, Y. Y. Huang, K.-C. Hwang, Y.-w. Zhang and J. A. Rogers, *Proceedings of the National Academy of Sciences*, 2008, **105**, 18675-18680.
232. S. H. Chae, W. J. Yu, J. J. Bae, D. L. Duong, D. Perello, H. Y. Jeong, Q. H. Ta, T. H. Ly, Q. A. Vu and M. Yun, *Nature materials*, 2013, **12**, 403.
233. F. Xu, M.-Y. Wu, N. S. Safron, S. S. Roy, R. M. Jacobberger, D. J. Bindl, J.-H. Seo, T.-H. Chang, Z. Ma and M. S. Arnold, *Nano letters*, 2014, **14**, 682-686.
234. I. M. Graz, D. P. Cotton, A. Robinson and S. P. Lacour, *Applied Physics Letters*, 2011, **98**, 124101.
235. Y. Mengüç, Y.-L. Park, H. Pei, D. Vogt, P. M. Aubin, E. Winchell, L. Fluke, L. Stirling, R. J. Wood and C. J. Walsh, *The International Journal of Robotics Research*, 2014, **33**, 1748-1764.
236. D. J. Lipomi and Z. Bao, *Energy & Environmental Science*, 2011, **4**, 3314-3328.
237. D. J. Lipomi, B. C. K. Tee, M. Vosgueritchian and Z. Bao, *Advanced Materials*, 2011, **23**, 1771-1775.
238. H. L. Filiatrault, G. C. Porteous, R. S. Carmichael, G. J. Davidson and T. B. Carmichael, *Advanced Materials*, 2012, **24**, 2673-2678.
239. X. Wang, Y. Gu, Z. Xiong, Z. Cui and T. Zhang, *Advanced materials*, 2014, **26**, 1336-1342.
240. J. Ge, L. Sun, F. R. Zhang, Y. Zhang, L. A. Shi, H. Y. Zhao, H. W. Zhu, H. L. Jiang and S. H. Yu, *Advanced materials*, 2016, **28**, 722-728.
241. J. Jang, S. H. Kim, S. Nam, D. S. Chung, C. Yang, W. M. Yun, C. E. Park and J. B. Koo, *Applied Physics Letters*, 2008, **92**, 126.
242. J. Jang, S. Nam, J. Hwang, J.-J. Park, J. Im, C. E. Park and J. M. Kim, *Journal of Materials Chemistry*, 2012, **22**, 1054-1060.
243. J.-H. Bae, W.-H. Kim, H. Kim, C. Lee and S.-D. Lee, *Journal of Applied Physics*, 2007, **102**, 063508.
244. P. Egerton, E. Pitts and A. Reiser, *Macromolecules*, 1981, **14**, 95-100.
245. A. N. Sokolov, B. C. Tee, C. J. Bettinger, J. B.-H. Tok and Z. Bao, *Accounts of chemical research*, 2011, **45**, 361-371.
246. E. Orgiu, I. Manunza, M. Sanna, P. Cosseddu and A. Bonfiglio, *Thin Solid Films*, 2008, **516**, 1533-1537.
247. M.-m. Ling, Z. Bao and D. Li, *Applied physics letters*, 2006, **88**, 033502.
248. N. T. Tien, T. Q. Trung, Y. G. Seoul, D. I. Kim and N.-E. Lee, *ACS nano*, 2011, **5**, 7069-7076.
249. M. Zirkl, A. Haase, A. Fian, H. Schön, C. Sommer, G. Jakopic, G. Leising, B. Stadlober, I. Graz and N. Gaar, *Advanced Materials*, 2007, **19**, 2241-2245.
250. J. Shi, M. B. Chan-Park and C. M. Li, *ACS applied materials & interfaces*, 2011, **3**, 1880-1886.
251. R. R. Kohlmeier, A. Javadi, B. Pradhan, S. Pilla, K. Setyowati, J. Chen and S. Gong, *The Journal of Physical Chemistry C*, 2009, **113**, 17626-17629.
252. K. Oh, J. Y. Lee, S.-S. Lee, M. Park, D. Kim and H. Kim, *Composites science and technology*, 2013, **83**, 40-46.
253. J. Lee, M. J. Panzer, Y. He, T. P. Lodge and C. D. Frisbie, *Journal of the American Chemical Society*, 2007, **129**, 4532-4533.
254. S.-K. Lee, S. H. Kabir, B. K. Sharma, B. J. Kim, J. H. Cho and J.-H. Ahn, *Nanotechnology*, 2013, **25**, 014002.
255. J. Pu, Y. Zhang, Y. Wada, J. Tse-Wei Wang, L.-J. Li, Y. Iwasa and T. Takenobu, *Applied Physics Letters*, 2013, **103**, 023505.
256. J. H. Cho, J. Lee, Y. He, B. Kim, T. P. Lodge and C. D. Frisbie, *Advanced materials*, 2008, **20**, 686-690.
257. J. H. Cho, J. Lee, Y. Xia, B. Kim, Y. He, M. J. Renn, T. P. Lodge and C. D. Frisbie, *Nature materials*, 2008, **7**, 900.
258. Y. Xia, W. Zhang, M. Ha, J. H. Cho, M. J. Renn, C. H. Kim and C. D. Frisbie, *Advanced Functional Materials*, 2010, **20**, 587-594.
259. M. Ha, Y. Xia, A. A. Green, W. Zhang, M. J. Renn, C. H. Kim, M. C. Hersam and C. D. Frisbie, *ACS nano*, 2010, **4**, 4388-4395.
260. S. J. Dünki, M. Dascalu, F. A. Nüesch and D. M. Opris, 2016.
261. F. B. Madsen, A. E. Daugaard, S. Hvilsted, M. Y. Benslimane

- and A. L. Skov, *Smart Materials and Structures*, 2013, **22**, 104002.
262. Q. Cao, S. H. Hur, Z. T. Zhu, Y. Sun, C. J. Wang, M. A. Meitl, M. Shim and J. A. Rogers, *Advanced Materials*, 2006, **18**, 304-309.
263. C. Reese, W.-J. Chung, M.-m. Ling, M. Roberts and Z. Bao, *Applied physics letters*, 2006, **89**, 202108.
264. J. Liang, L. Li, D. Chen, T. Hajagos, Z. Ren, S.-Y. Chou, W. Hu and Q. Pei, *Nature communications*, 2015, **6**, 7647.
265. J. Y. Oh, S. Rondeau-Gagne, Y. C. Chiu, A. Chortos, F. Lissel, G. N. Wang, B. C. Schroeder, T. Kurosawa, J. Lopez, T. Katsumata, J. Xu, C. Zhu, X. Gu, W. G. Bae, Y. Kim, L. Jin, J. W. Chung, J. B. Tok and Z. Bao, *Nature*, 2016, **539**, 411-415.
266. L. Cai, S. Zhang, J. Miao, Z. Yu and C. Wang, *ACS Nano*, 2016, **10**, 11459-11468.
267. J. Xu, S. Wang, G.-J. N. Wang, C. Zhu, S. Luo, L. Jin, X. Gu, S. Chen, V. R. Feig and J. W. To, *Science*, 2017, **355**, 59-64.
268. S. K. Lee, B. J. Kim, H. Jang, S. C. Yoon, C. Lee, B. H. Hong, J. A. Rogers, J. H. Cho and J. H. Ahn, *Nano Lett*, 2011, **11**, 4642-4646.
269. A. Sekiguchi, F. Tanaka, T. Saito, Y. Kuwahara, S. Sakurai, D. N. Futaba, T. Yamada and K. Hata, *Nano Lett*, 2015, **15**, 5716-5723.
270. K. H. Lee, M. S. Kang, S. Zhang, Y. Gu, T. P. Lodge and C. D. Frisbie, *Adv Mater*, 2012, **24**, 4457-4462.
271. F. Xu, M. Y. Wu, N. S. Safron, S. S. Roy, R. M. Jacobberger, D. J. Bindl, J. H. Seo, T. H. Chang, Z. Ma and M. S. Arnold, *Nano Lett*, 2014, **14**, 682-686.
272. M. Shin, J. H. Song, G. H. Lim, B. Lim, J. J. Park and U. Jeong, *Adv Mater*, 2014, **26**, 3706-3711.
273. F. Carpi, G. Gallone, F. Galantini and D. De Rossi, *Advanced Functional Materials*, 2008, **18**, 235-241.
274. C. Ellingford, C. Bowen, T. McNally and C. Wan, *Macromol Rapid Commun*, 2018, **39**, e1800340.
275. S. J. Dünki, E. Cuervo-Reyes and D. M. Opris, *Polym Chem-Uk*, 2017, **8**, 715-724.
276. H. Liu, L. Zhang, D. Yang, N. Ning, Y. Yu, L. Yao, B. Yan and M. Tian, *Journal of Physics D: Applied Physics*, 2012, **45**, 485303.
277. C. Mali, S. Chavan, K. Kanse, A. Kumbharkhane and S. Mehrotra, 2007.
278. R.-Q. Png, P.-J. Chia, J.-C. Tang, B. Liu, S. Sivaramakrishnan, M. Zhou, S.-H. Khong, H. S. Chan, J. H. Burroughes and L.-L. Chua, *Nature materials*, 2010, **9**, 152.
279. L.-H. Liu and M. Yan, *Accounts of chemical research*, 2010, **43**, 1434-1443.
280. C. M. Roland, 2013, DOI: 10.1007/978-3-642-36199-9_91-1, 1-9.
281. C. Tugui, S. Vlad, M. Iacob, C. D. Varganici, L. Pricop and M. Cazacu, *Polymer Chemistry*, 2016, **7**, 2709-2719.
282. E. Bortot and M. Gei, *Extreme Mechanics Letters*, 2015, **5**, 62-73.
283. T. Li, S. Qu and W. Yang, *Journal of Applied Physics*, 2012, **112**, 034119.
284. G. Kang, K.-S. Kim and S. Kim, *Review of Scientific Instruments*, 2011, **82**, 046101.
285. R. Pelrine, R. D. Kornbluh, J. Eckerle, P. Jeuck, S. Oh, Q. Pei and S. Stanford, 2001.
286. B. Kussmaul, S. Risse, G. Kofod, R. Waché, M. Wegener, D. N. McCarthy, H. Krüger and R. Gerhard, *Advanced Functional Materials*, 2011, **21**, 4589-4594.
287. S. Risse, B. Kussmaul, H. Krüger and G. Kofod, *RSC Advances*, 2012, **2**, 9029-9035.
288. B. Kussmaul, S. Risse, M. Wegener, G. Kofod and H. Krüger, *Smart Materials and Structures*, 2012, **21**, 064005.
289. C. Huang, Q. Zhang, G. debotton and K. Bhattacharya, *Appl Phys Lett*, 2004, **84**, 4391-4393.
290. W. Hu, S. N. Zhang, X. Niu, C. Liu and Q. Pei, *Journal of Materials Chemistry C*, 2014, **2**, 1658.
291. P. Brochu and Q. Pei, *Macromol Rapid Commun*, 2010, **31**, 10-36.
292. D. Chen and Q. Pei, *Chem Rev*, 2017, **117**, 11239-11268.
293. S. A. Harich, D. Dai, C. C. Wang, X. Yang, S. D. Chao and R. T. Skodje, *Nature*, 2002, **419**, 281-284.
294. A. Bele, C. Tugui, L. Sacarescu, M. Iacob, G. Stiubianu, M. Dascalu, C. Racles and M. Cazacu, *Materials & Design*, 2018, **141**, 120-131.
295. G. Yin, Y. Yang, F. Song, C. Renard, Z.-M. Dang, C.-Y. Shi and D. Wang, *Acs Appl Mater Inter*, 2017, **9**, 5237-5243.
296. H. Stoyanov, M. Kolloosche, S. Risse, D. N. McCarthy and G. Kofod, *Soft Matter*, 2011, **7**, 194-202.
297. G. Gallone, F. Carpi, D. De Rossi, G. Levita and A. Marchetti, *Materials Science and Engineering: C*, 2007, **27**, 110-116.
298. C. Huang, Q. Zhang and J. Su, *Applied Physics Letters*, 2003, **82**, 3502-3504.
299. Q. Zhang, H. Li, M. Poh, F. Xia, Z.-Y. Cheng, H. Xu and C. Huang, *Nature*, 2002, **419**, 284.
300. B. Guiffard, L. Seveyrat, G. Sebald and D. Guyomar, *Journal of Physics D: Applied Physics*, 2006, **39**, 3053.
301. F. Galantini, S. Bianchi, V. Castelvetro and G. Gallone, *Smart Materials and Structures*, 2013, **22**, 055025.
302. Y. Wang and L. Z. Sun, *Appl Phys Lett*, 2017, **111**, 161904.
303. F. Zhang, T. Li and Y. Luo, *Compos Sci Technol*, 2018, **156**, 151-157.
304. M. Panahi-Sarmad and M. Razzaghi-Kashani, *Smart Mater Struct*, 2018, **27**, 085021.
305. S.-Q. Wu, J.-W. Wang, J. Shao, L. Wei, R.-K. Ge and H. Ren, *Materials & Design*, 2018, **146**, 208-218.
306. A. Fassler and C. Majidi, *Adv Mater*, 2015, **27**, 1928-1932.
307. M. D. Bartlett, N. Kazem, M. J. Powell-Palm, X. Huang, W. Sun, J. A. Malen and C. Majidi, *Proc Natl Acad Sci U S A*, 2017, **114**, 2143-2148.
308. M. D. Bartlett, A. Fassler, N. Kazem, E. J. Markvicka, P. Mandal and C. Majidi, *Adv Mater*, 2016, **28**, 3726-3731.
309. P. Mazurek, L. Yu, R. Gerhard, W. Wirges and A. L. Skov, *J Appl Polym Sci*, 2016, **133**.
310. P. Mazurek, S. Hvilsted and A. L. Skov, *Polymer*, 2016, **87**, 1-7.
311. L. Shi, R. Yang, S. Lu, K. Jia, C. Xiao, T. Lu, T. Wang, W. Wei, H. Tan and S. Ding, *NPG Asia Materials*, 2018, DOI: 10.1038/s41427-018-0077-7.
312. Q.-P. Zhang, J.-H. Liu, H.-D. Liu, F. Jia, Y.-L. Zhou and J. Zheng, *Appl Phys Lett*, 2017, **111**, 152901.
313. B. Li, J. Zhang, H. Chen and D. Li, *Physical review E*, 2016, **93**, 052506.
314. E. Delebecq, N. Hermeline, A. Flers and F. o. Ganachaud, *Acs Appl Mater Inter*, 2012, **4**, 3353-3363.
315. Y. Zhao, J.-W. Zha, L.-J. Yin, Z.-S. Gao, Y.-Q. Wen and Z.-M. Dang, *Polymer*, 2018, **137**, 269-275.
316. P. Brochu and Q. Pei, *Macromolecular rapid communications*, 2010, **31**, 10-36.
317. R. Pelrine, R. Kornbluh, Q. Pei and J. Joseph, *Science*, 2000, **287**, 836-839.
318. R. Pelrine, R. Kornbluh and G. Kofod, *Advanced Materials*,

- 2000, **12**, 1223-1225.
319. G. Kofod, P. Sommer-Larsen, R. Kornbluh and R. Pelrine, *Journal of intelligent material systems and structures*, 2003, **14**, 787-793.
320. J.-S. Plante and S. Dubowsky, *International journal of solids and structures*, 2006, **43**, 7727-7751.
321. G. Kofod, R. D. Kornbluh, R. Pelrine and P. Sommer-Larsen, 2001.
322. X. Zhao and Z. Suo, *Appl Phys Lett*, 2007, **91**, 061921.
323. R. Palakodeti and M. Kessler, *Materials Letters*, 2006, **60**, 3437-3440.
324. H. R. Choi, K. Jung, N. H. Chuc, M. Jung, I. Koo, J. Koo, J. Lee, J. Lee, J. Nam and M. Cho, 2005.
325. P. Lochmatter, G. Kovacs and M. Wissler, *Smart Materials and Structures*, 2007, **16**, 477.
326. M. Wissler and E. Mazza, *Sensors and Actuators A: Physical*, 2005, **120**, 184-192.
327. Q. Pei, R. Pelrine, S. Stanford, R. Kornbluh and M. Rosenthal, *Synthetic Metals*, 2003, **135**, 129-131.
328. N. Goulbourne, E. Mockensturm and M. Frecker, *International Journal of Solids and Structures*, 2007, **44**, 2609-2626.
329. N. Goulbourne, E. Mockensturm and M. Frecker, *Journal of Applied Mechanics*, 2005, **72**, 899-906.
330. P. Lochmatter and G. Kovacs, *Sensors and Actuators A: Physical*, 2008, **141**, 577-587.
331. L. Patrick, K. Gabor and M. Silvain, *Sensors and actuators A: Physical*, 2007, **135**, 748-757.
332. E. M. Mockensturm and N. Goulbourne, *International Journal of Non-Linear Mechanics*, 2006, **41**, 388-395.
333. M. Wissler and E. Mazza, *Sensors and Actuators A: Physical*, 2007, **134**, 494-504.
334. M. Wissler and E. Mazza, *Sensors and Actuators A: Physical*, 2007, **138**, 384-393.
335. Y. Bar-Cohen, X. Niu, R. Leo, D. Chen, W. Hu and Q. Pei, 2013, **8687**, 86871M.
336. J. D. Madden, N. A. Vandesteeg, P. A. Anquetil, P. G. Madden, A. Takshi, R. Z. Pytel, S. R. Lafontaine, P. A. Wieringa and I. W. Hunter, *IEEE Journal of oceanic engineering*, 2004, **29**, 706-728.
337. Z. Suo and J. Zhu, *Applied Physics Letters*, 2009, **95**, 232909.
338. S. M. Ha, W. Yuan, Q. Pei, R. Pelrine and S. Stanford, *Advanced Materials*, 2006, **18**, 887-891.
339. S. M. Ha, W. Yuan, Q. Pei, R. Pelrine and S. Stanford, *Smart Materials and Structures*, 2007, **16**, S280.
340. S. M. Ha, M. Wissler, R. Pelrine, S. Stanford, G. M. Kovacs and Q. Pei, 2007.
341. S. M. Ha, I. S. Park, M. Wissler, R. Pelrine, S. Stanford, K. J. Kim, G. M. Kovacs and Q. Pei, 2008.
342. S. Arora, T. Ghosh and J. Muth, *Sensors and Actuators A: Physical*, 2007, **136**, 321-328.
343. C. G. Cameron, J. P. Szabo, S. Johnstone, J. Massey and J. Leidner, *Sensors and Actuators A: Physical*, 2008, **147**, 286-291.
344. N. H. Chuc, J. Park, D. V. Thuy, H. S. Kim, J. Koo, Y. Lee, J. Nam and H. R. Choi, 2007.
345. G. M. Kovacs, S. M. Ha, S. Michel, R. Pelrine and Q. Pei, 2008.
346. G. Kovacs and L. Düring, 2009.
347. T. E. Herod and J. B. Schlenoff, *Chemistry of materials*, 1993, **5**, 951-955.
348. T. Lam, H. Tran, W. Yuan, Z. Yu, S. Ha, R. Kaner and Q. Pei, 2008.
349. G. Kovacs, P. Lochmatter and M. Wissler, *Smart Materials and Structures*, 2007, **16**, S306.
350. X. Niu, H. Stoyanov, W. Hu, R. Leo, P. Brochu and Q. Pei, *Journal of Polymer Science Part B: Polymer Physics*, 2013, **51**, 197-206.
351. M. Vatankeh - Varnoosfaderani, W. F. Daniel, A. P. Zhushma, Q. Li, B. J. Morgan, K. Matyjaszewski, D. P. Armstrong, R. J. Spontak, A. V. Dobrynin and S. S. Sheiko, *Advanced Materials*, 2017, **29**.
352. S. Yun, X. Niu, Z. Yu, W. Hu, P. Brochu and Q. Pei, *Advanced materials*, 2012, **24**, 1321-1327.
353. Z. Yu, X. Niu, P. Brochu, W. Yuan, H. Li, B. Chen and Q. Pei, 2010.
354. Z. Ren, W. Hu, C. Liu, S. Li, X. Niu and Q. Pei, *Macromolecules*, 2015, **49**, 134-140.
355. C. Tugui, G. Stiubianu, M. Iacob, C. Ursu, A. Bele, S. Vlad and M. Cazacu, *Journal of Materials Chemistry C*, 2015, **3**, 8963-8969.
356. J. Yi, J. M. Lee and W. I. Park, *Sensors and Actuators B: Chemical*, 2011, **155**, 264-269.
357. Y. Xie, Y. Meng, W. X. Wang, E. Zhang, J. S. Leng and Q. B. Pei, *Adv Funct Mater*, 2018, **28**, 1802430.
358. N. Inkson, R. Graham, T. McLeish, D. Groves and C. Fernyhough, *Macromolecules*, 2006, **39**, 4217-4227.
359. M. Kapnistos, D. Vlassopoulos, J. Roovers and L. Leal, *Macromolecules*, 2005, **38**, 7852-7862.
360. L. J. Fetters, D. J. Lohse, C. A. García-Franco, P. Brant and D. Richter, *Macromolecules*, 2002, **35**, 10096-10101.
361. H. Yamazaki, M. Takeda, Y. Kohno, H. Ando, K. Urayama and T. Takigawa, *Macromolecules*, 2011, **44**, 8829-8834.
362. T. Pakula, Y. Zhang, K. Matyjaszewski, H.-i. Lee, H. Boerner, S. Qin and G. C. Berry, *Polymer*, 2006, **47**, 7198-7206.
363. M. Hu, Y. Xia, G. B. McKenna, J. A. Kornfield and R. H. Grubbs, *Macromolecules*, 2011, **44**, 6935-6943.
364. S. J. Dalsin, M. A. Hillmyer and F. S. Bates, *Macromolecules*, 2015, **48**, 4680-4691.
365. W. F. Daniel, J. Burdyńska, M. Vatankeh-Varnoosfaderani, K. Matyjaszewski, J. Paturej, M. Rubinstein, A. V. Dobrynin and S. S. Sheiko, *Nature materials*, 2016, **15**, 183.
366. S. Shian, R. M. Diebold and D. R. Clarke, *Optics express*, 2013, **21**, 8669-8676.
367. P. Caspari, S. J. Dünki, F. A. Nüesch and D. M. Opris, *Journal of Materials Chemistry C*, 2018, **6**, 2043-2053.
368. Y. Yamano, *IEEE Transactions on dielectrics and electrical insulation*, 2006, **13**, 773-781.
369. A. H. A. Razak and A. L. Skov, *Rsc Adv*, 2017, **7**, 468-477.
370. P. J. Madsen, L. Yu, S. Boucher and A. L. Skov, *Rsc Adv*, 2018, **8**, 23077-23088.
371. E. Acome, S. Mitchell, T. Morrissey, M. Emmett, C. Benjamin, M. King, M. Radakovitz and C. Keplinger, *Science*, 2018, **359**, 61-65.
372. P. Brochu and Q. Pei, in *Electroactivity in Polymeric Materials*, Springer, 2012, pp. 1-56.
373. C. Jean-Mistral, S. Basrour and J.-J. Chaillout, 2008.
374. G. Park, H. J. Chung, K. Kim, S. A. Lim, J. Kim, Y. S. Kim, Y. Liu, W. H. Yeo, R. H. Kim, S. S. Kim, J. S. Kim, Y. H. Jung, T. I. Kim, C. Yee, J. A. Rogers and K. M. Lee, *Adv Healthc Mater*, 2014, **3**, 515-525.
375. D. Bobo, K. J. Robinson, J. Islam, K. J. Thurecht and S. R. Corrie, *Pharm Res*, 2016, **33**, 2373-2387.
376. K. Zarschler, L. Rocks, N. Licciardello, L. Boselli, E. Polo, K.

- P. Garcia, L. De Cola, H. Stephan and K. A. Dawson, *Nanomedicine*, 2016, **12**, 1663-1701.
377. R. Rajan, K. Chandran, S. L. Harper, S. I. Yun and P. T. Kalaichelvan, *Ind Crop Prod*, 2015, **70**, 356-373.
378. J. J. Park, W. J. Hyun, S. C. Mun, Y. T. Park and O. O. Park, *Acs Appl Mater Inter*, 2015, **7**, 6317-6324.
379. H. Wu, L. B. Hu, M. W. Rowell, D. S. Kong, J. J. Cha, J. R. McDonough, J. Zhu, Y. A. Yang, M. D. McGehee and Y. Cui, *Nano Lett*, 2010, **10**, 4242-4248.
380. L. Cai, L. Song, P. Luan, Q. Zhang, N. Zhang, Q. Gao, D. Zhao, X. Zhang, M. Tu, F. Yang, W. Zhou, Q. Fan, J. Luo, W. Zhou, P. M. Ajayan and S. Xie, *Sci Rep*, 2013, **3**, 3048.
381. M. Vosgueritchian, D. J. Lipomi and Z. A. Bao, *Adv Funct Mater*, 2012, **22**, 421-428.
382. P. Mazurek, L. Yu, R. Gerhard, W. Wirges and A. L. Skov, *Journal of Applied Polymer Science*, 2016, **133**, 44153.
383. M. Vatankhah - Varnoosfaderani, W. F. Daniel, A. P. Zhushma, Q. Li, B. J. Morgan, K. Matyjaszewski, D. P. Armstrong, R. J. Spontak, A. V. Dobrynin and S. S. Sheiko, *Advanced Materials*, 2017, **29**, 1604209.

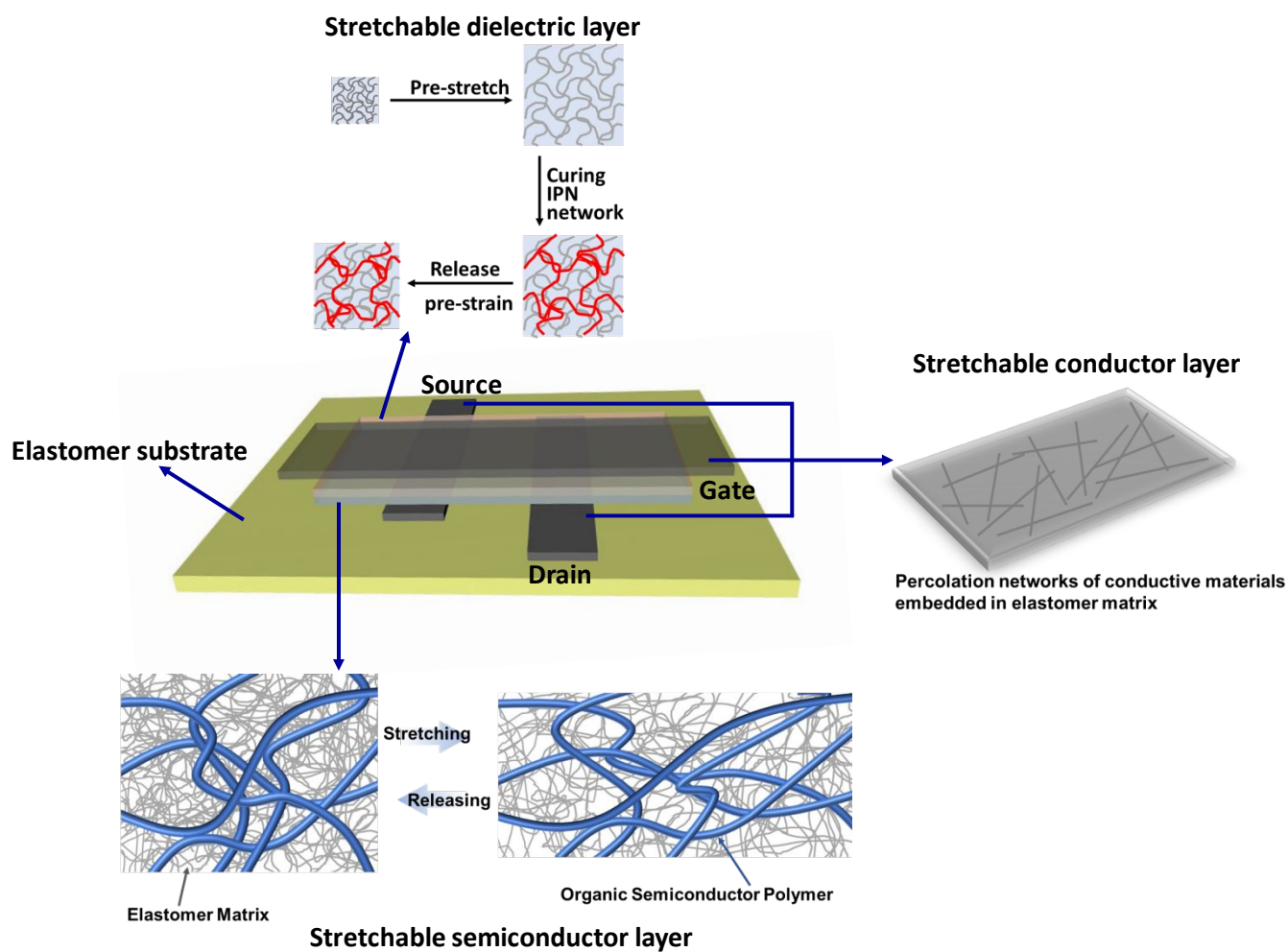


Figure 1. Schematic of an intrinsically stretchable TFT comprising elastomeric conductors, semiconductors, dielectric materials and substrate, all made stretchable via morphological/nanostructural controls.

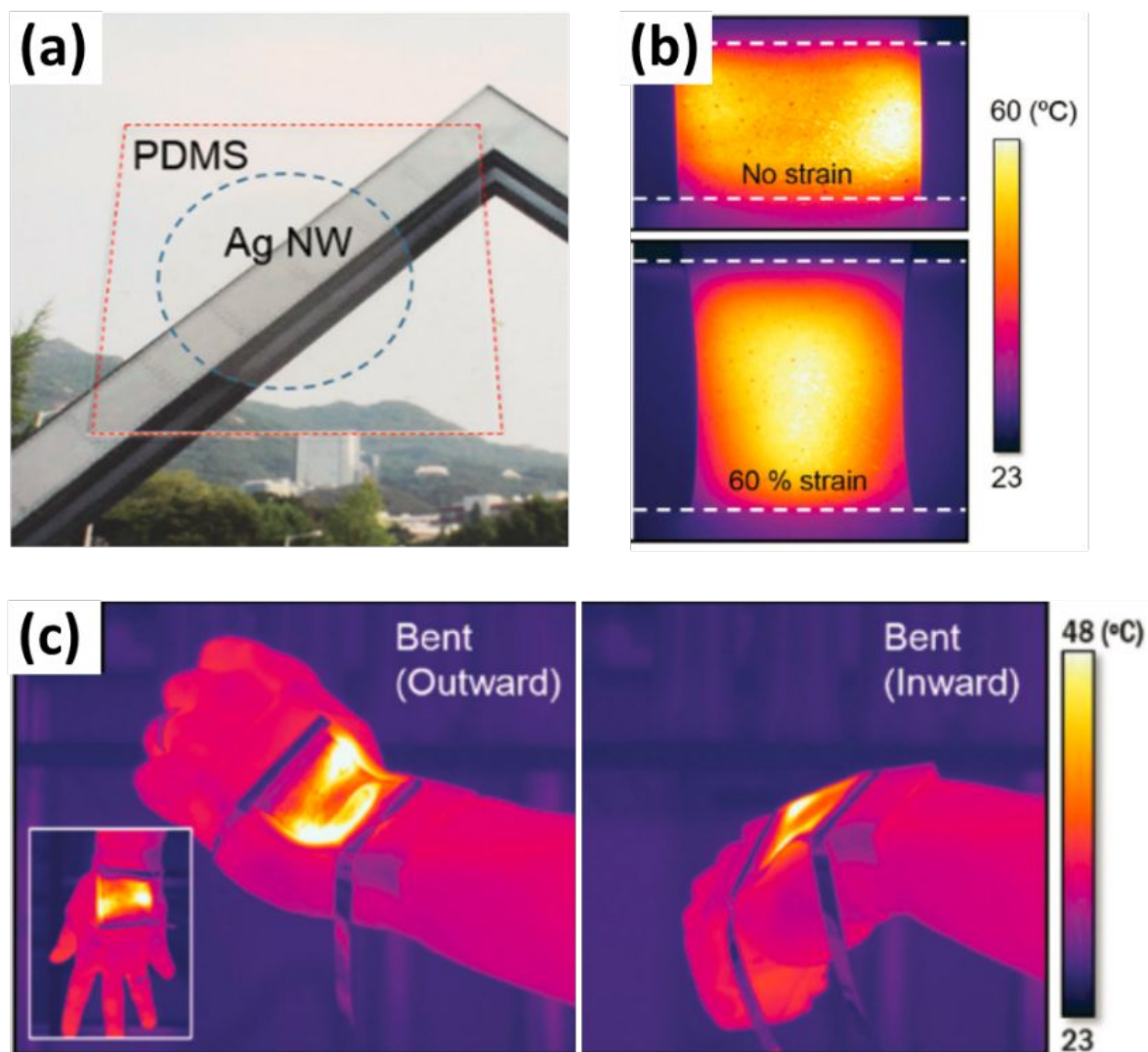


Figure 2. Performance of transparent and stretchable AgNWs/PDMS heater. (a) Photograph of transparent and stretchable AgNWs percolation network on PDMS substrate. The blue dotted circle represents the AgNWs network. (b) Infrared images of AgNWs/PDMS heater operated at 60 °C before and after stretching with 60% strain. (c) Temperature profiles of a transparent and stretchable AgNWs/PDMS heat attached onto a human wrist under the conditions of outward (Left) and inward bending (Right). Inset shows top view of the infrared image of heater on the wrist. Adapted with permission.⁸⁴ Copyright 2015, Wiley-VCH.

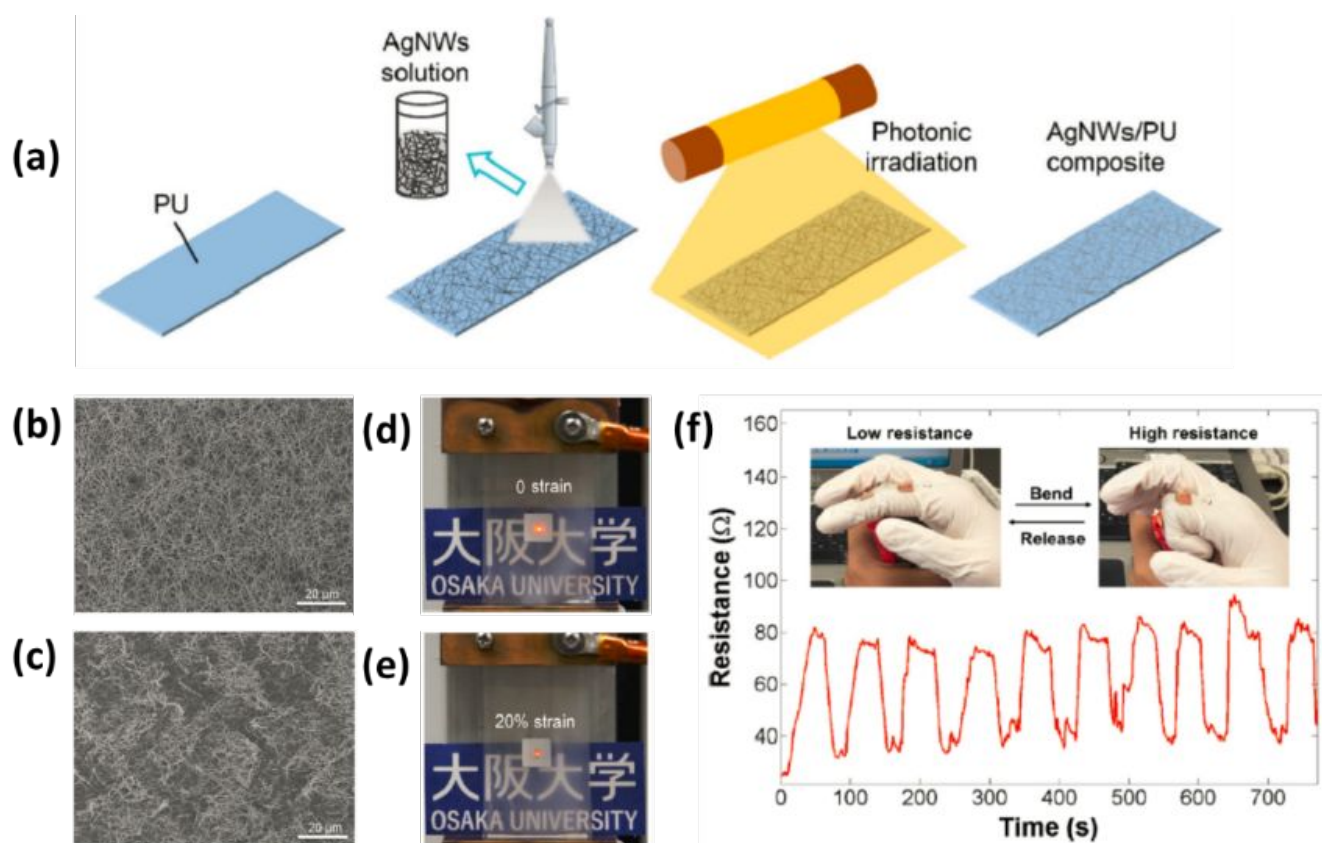


Figure 3. (a) Fabrication of AgNWs/PU composite electrode by high intensity pulsed light. SEM images of stretchable AgNWs/PU conductor (b) before stretching and (c) after stretching at 100% strain. LED integrated conductor based on stretchable AgNWs/PU electrode (d) before stretching and (e) after stretching at 20% strain. (f) Human motion detection of finger joint by stretchable AgNWs/PU composite electrode. Adapted with permission.⁸⁷ Copyright 2016, Springer.

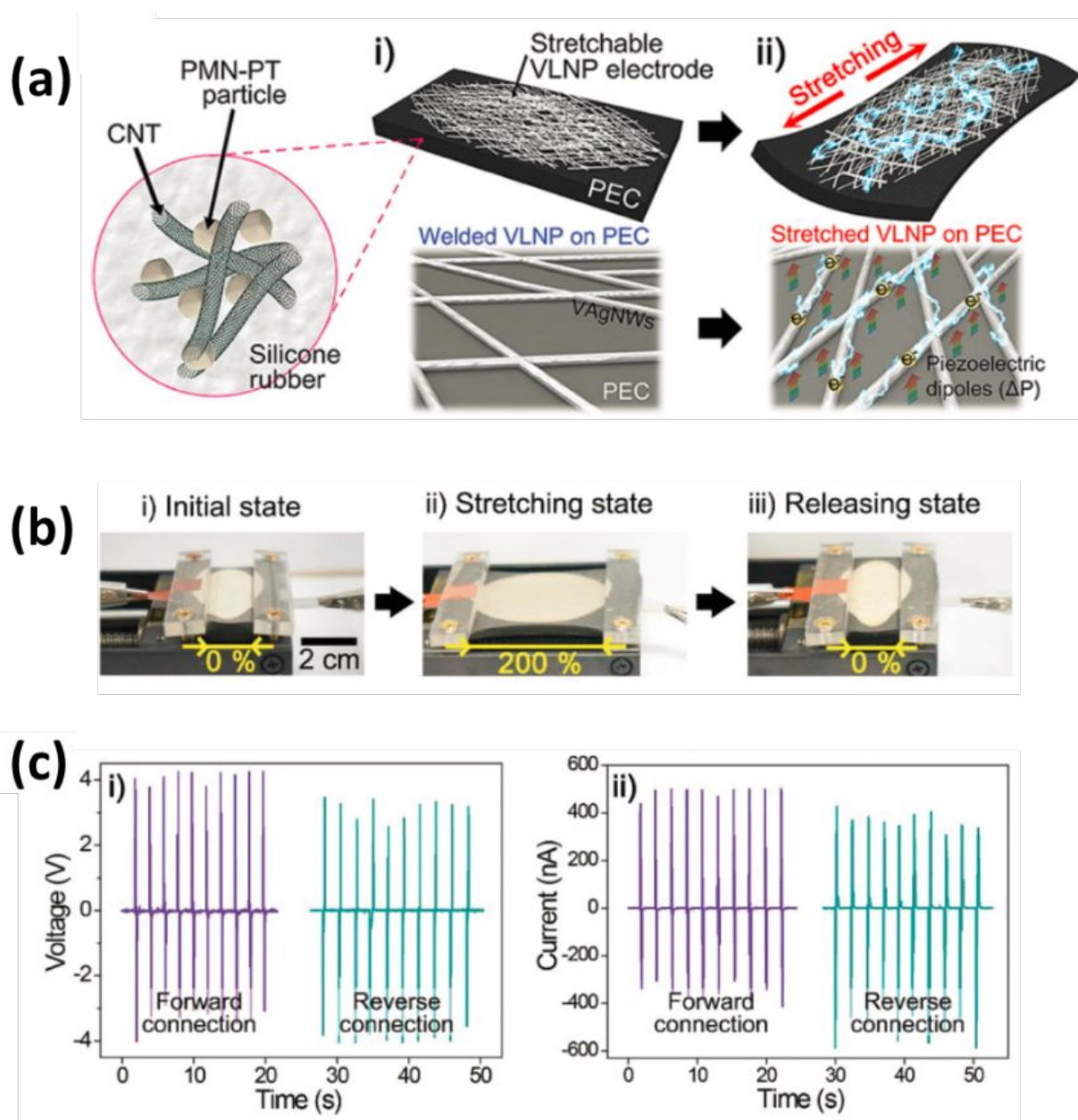


Figure 4. (a) Schematic of stretchable energy harvester. i) Piezoelectric elastic composite made of ecoflex silicone rubber, PMN-PT particles and MWCNTs with both sides of stretchable very long AgNWs percolation network before stretching. ii) The generation of electricity under the stretching state. The magnified schematics of stretchable very long AgNWs percolation network before and after stretching are presented at the bottom panels. (b) Photographs of stretchable energy harvester under the states of before stretching, after stretching at 200% strain and releasing. (c) The generation of i) the output open-circuit voltage and ii) the short-circuit current in the forward and reverse connections from stretchable energy harvester. Adapted with permission.²⁷ Copyright 2015, Wiley-VCH.

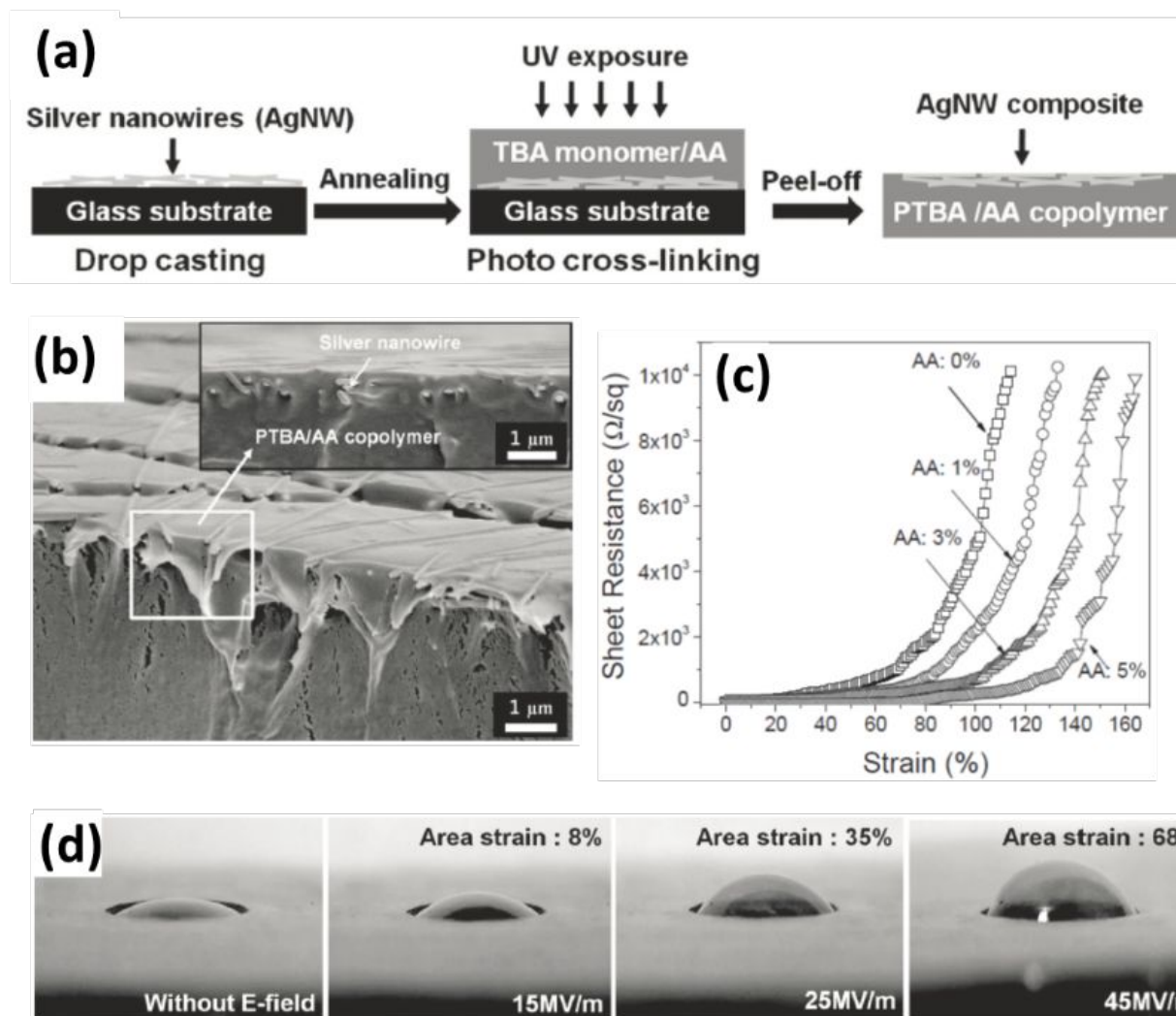


Figure 5. (a) Preparation of AgNW percolation network embedded in the shape memorable electroactive polymer of poly(TBA-co-AA). (b) SEM image of cross-section of AgNWs-poly(TBA-co-AA) electrode. (c) Sheet resistance change of AgNWs composite electrode as a function of strain and the concentration of AA. (d) Photographs of area strain of BSEP actuator as a function of electric fields. Adapted with permission.⁹² Copyright 2015, Wiley-VCH.

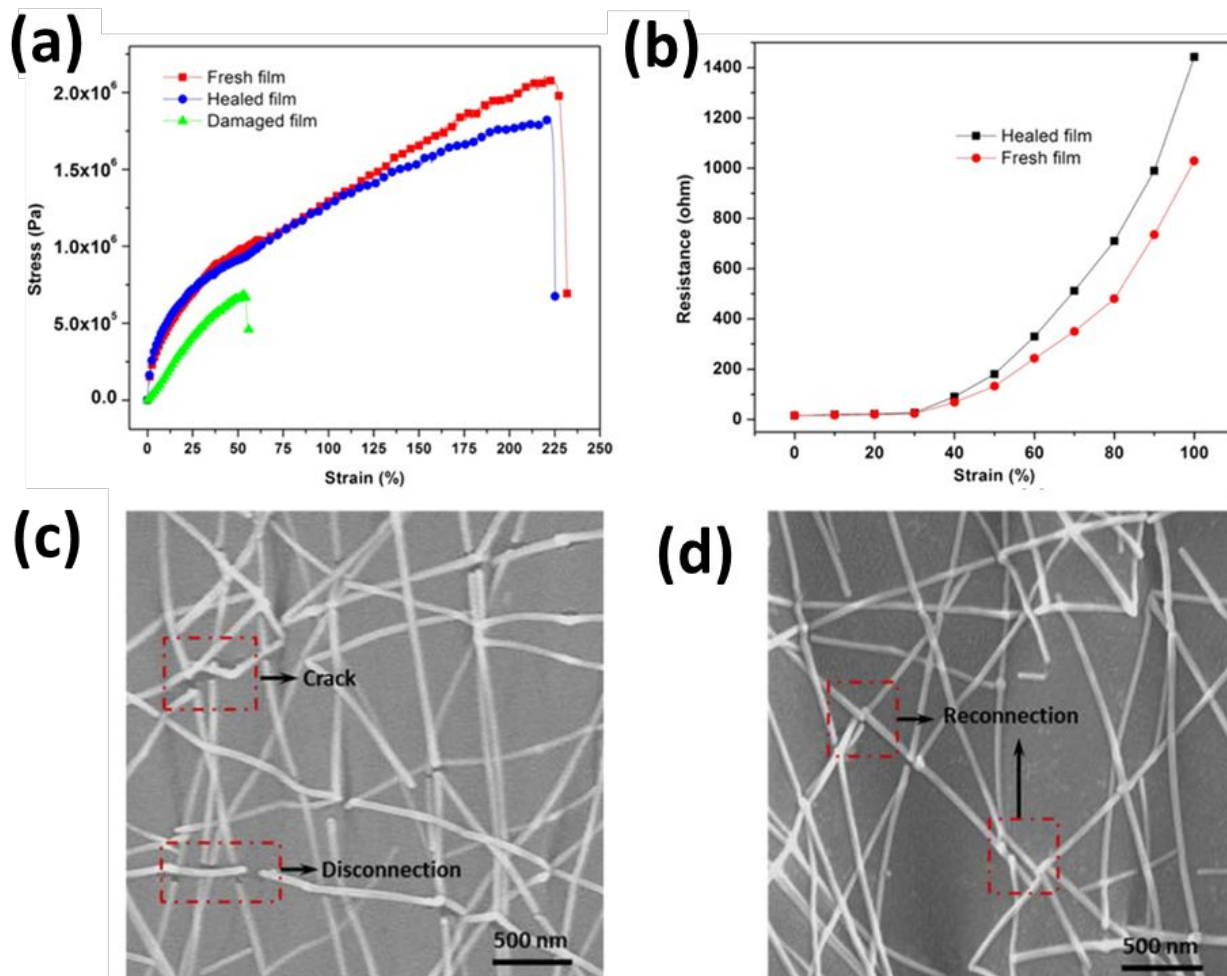


Figure 6. (a) Mechanical stress-strain responses of fresh AgNWs composite electrode, blade cut sample with 40 μm depth, and healed electrode by heating at 100 $^{\circ}\text{C}$ for 3 min as a function of strain. (b) Resistance change of fresh and healed AgNWs composite electrodes as a function of strain. SEM images of top view of (c) AgNWs composite film after 100 times of stretching-relaxing between 0% and 60% strain and (d) After healing by heating treatment at 100 $^{\circ}\text{C}$ for 70s. Adapted with permission.⁹⁵ Copyright 2015, American Chemical Society.

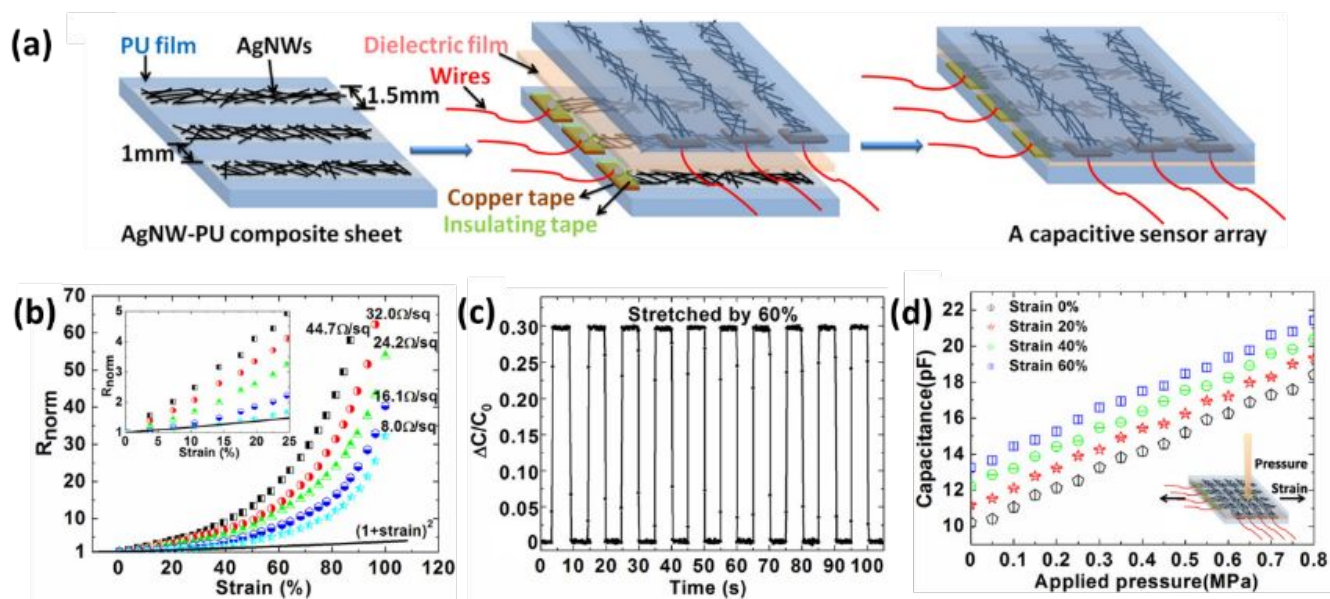


Figure 7. (a) Schematic of the preparation of stretchable transparent capacitive sensor by sandwiching acrylic elastomer layer between AgNWs network electrodes embedded in PU substrate. (b) Normalized resistance changes of AgNWs composite electrodes with different initial sheet resistance as a function of strain. (c) Capacitance changes of device stretched between 0% and 60% during cyclic test. (d) Capacitance changes of device at different tensile strain as a function of applied pressure. Adapted with permission.⁹³ Copyright 2013, American Institute of Physics.

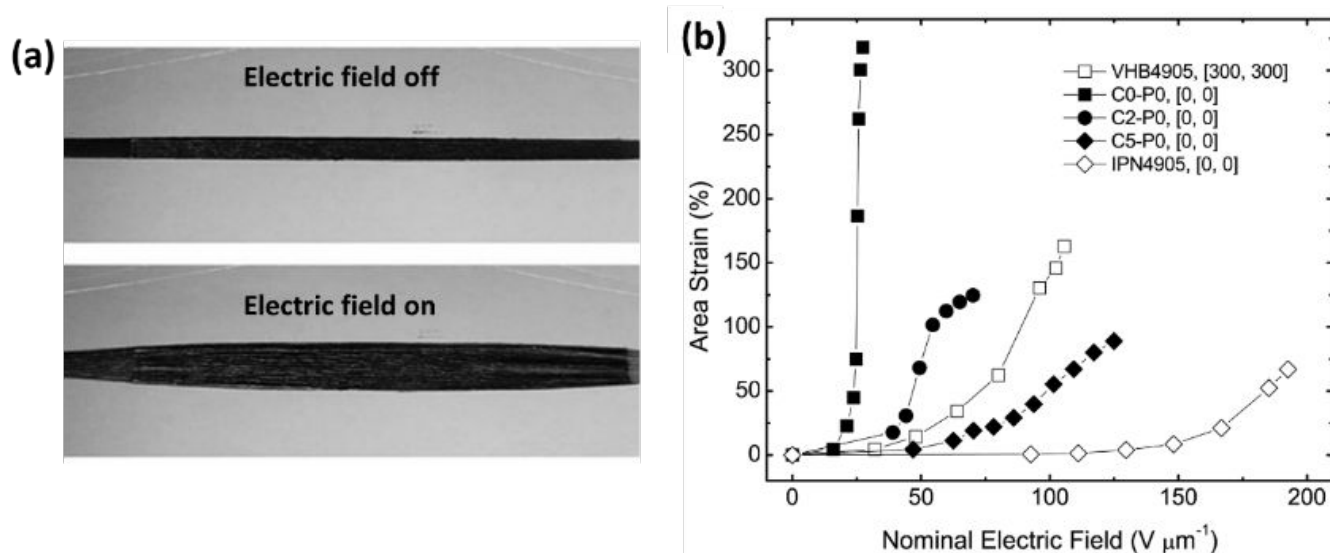


Figure 8. (a) Prestrained HS3 silicone film with both sides of carbon grease electrodes for the electric field off (top) and on (bottom), 117% relative strain was obtained under a field of 128 MV/m in the central region of actuator (bottom). Adapted with permission.⁸ Copyright 2000, American Association for the Advancement of Science. (b) Area strain of actuators with different crosslinker concentrations as a function of applied electric field. Adapted with permission.¹⁰⁹ Copyright 2013, Wiley-VCH.

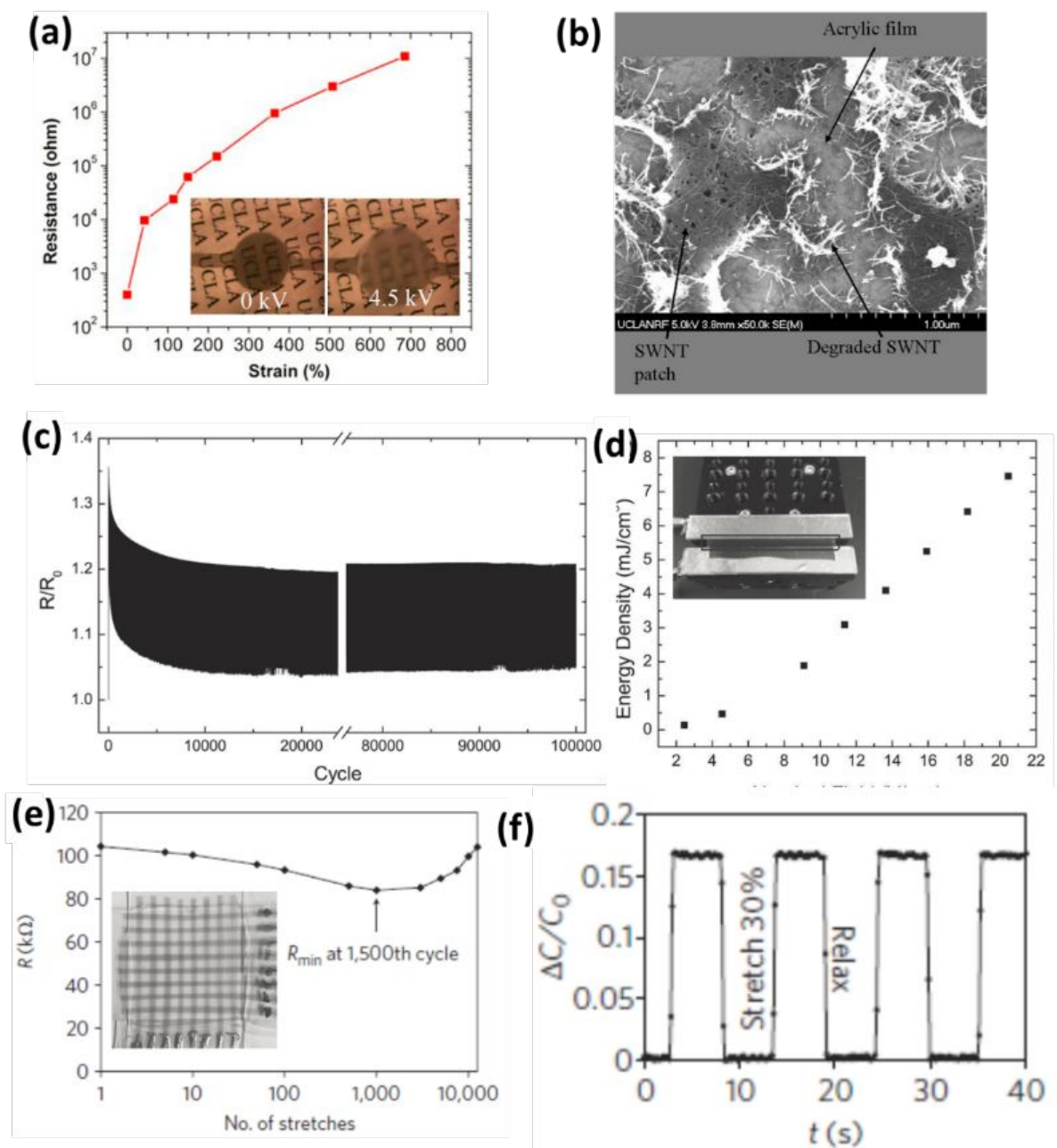


Figure 9. (a) Resistance change of spray-coated SWNTs electrode on 3M VHB 4905 as a function of strain. Inset: Photographs of actuator under the different applied voltage. Adapted with permission.¹¹² Copyright 2009, American Institute of Physics. (b) SEM image of self-cleared SWNTs surface near the fault. Adapted with permission.⁹⁶ Copyright 2008, Wiley-VCH. (c) Cyclic test of silicone-carbon nanotubes composite electrode between 0% and 100% strain at a strain rate of $1000\% \text{ s}^{-1}$. (d) Energy density of capacitive energy harvester as a function of applied electric field. Inset: An energy harvester attached to the linear stage. Adapted with permission.¹¹³ Copyright 2014, Wiley-VCH. (e) Resistance change of SWNTs on PDMS substrate as a function of stretching cycles. Inset: Photograph of a skin-like pressure and strain sensor. (f) Cyclic test of capacitance change under the stretching between 0% and 30% strain. Adapted with permission.⁶⁴ Copyright 2011, Nature Publishing Group.

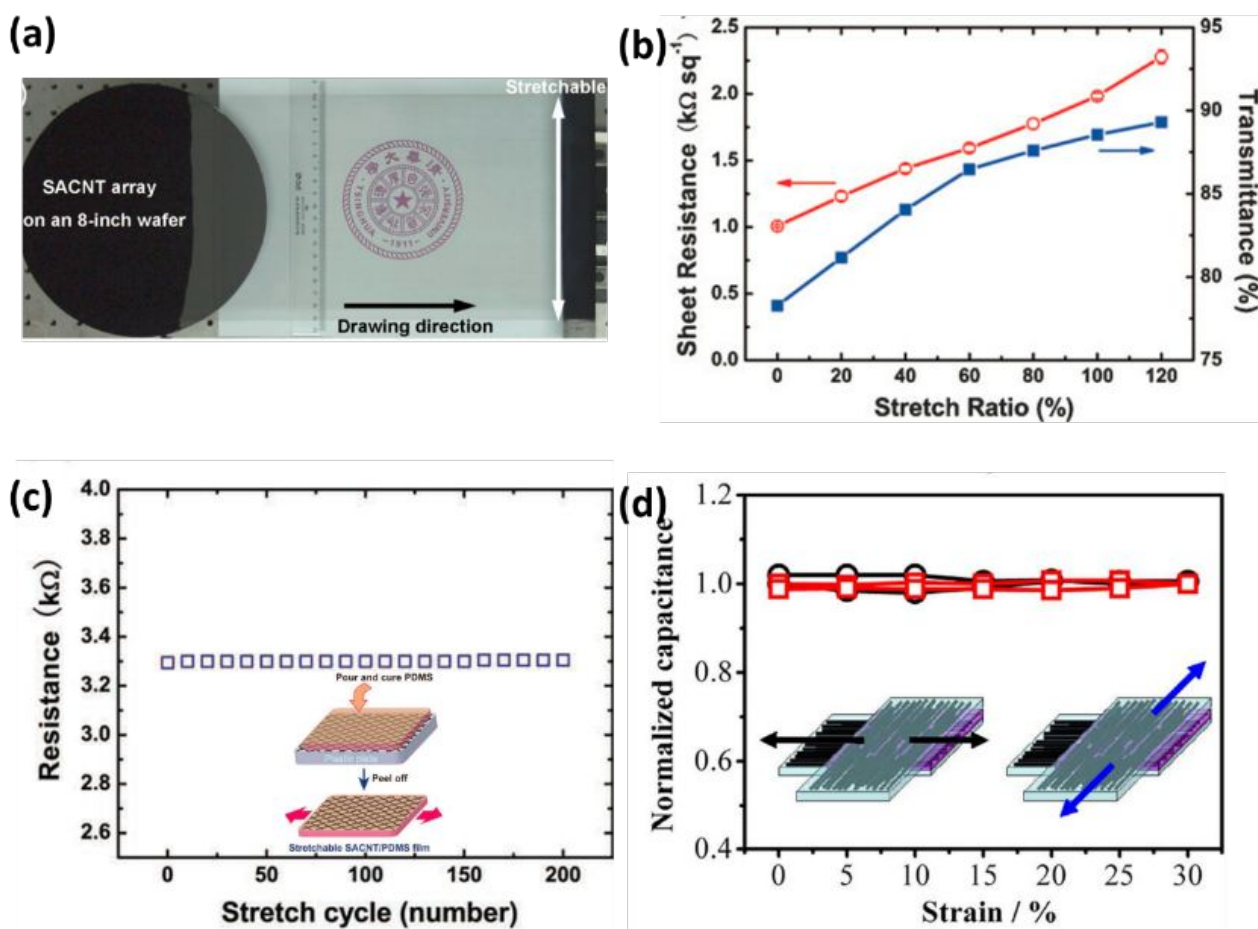


Figure 10. (a) Superaligned CNTs film drawn out from a superaligned CNTs array on 8-inch silicon wafer. (b) Sheet resistance and transmittance of freestanding superaligned CNTs film as a function of strain. Adapted with permission.¹¹⁴ Copyright 2010, Wiley-VCH. (c) Resistance change of superaligned CNTs/PDMS composite film as a function of cyclic test. Inset: Schematic of fabrication of superaligned CNTs/PDMS composite film. Adapted with permission.¹¹⁷ Copyright 2011, Wiley-VCH. (d) Capacitance change of device as a function of tensile strain in both directions. Inset: Schematic of supercapacitor with biaxially stretching. Adapted with permission.¹¹⁵ Copyright 2014, Nature Publishing Group.

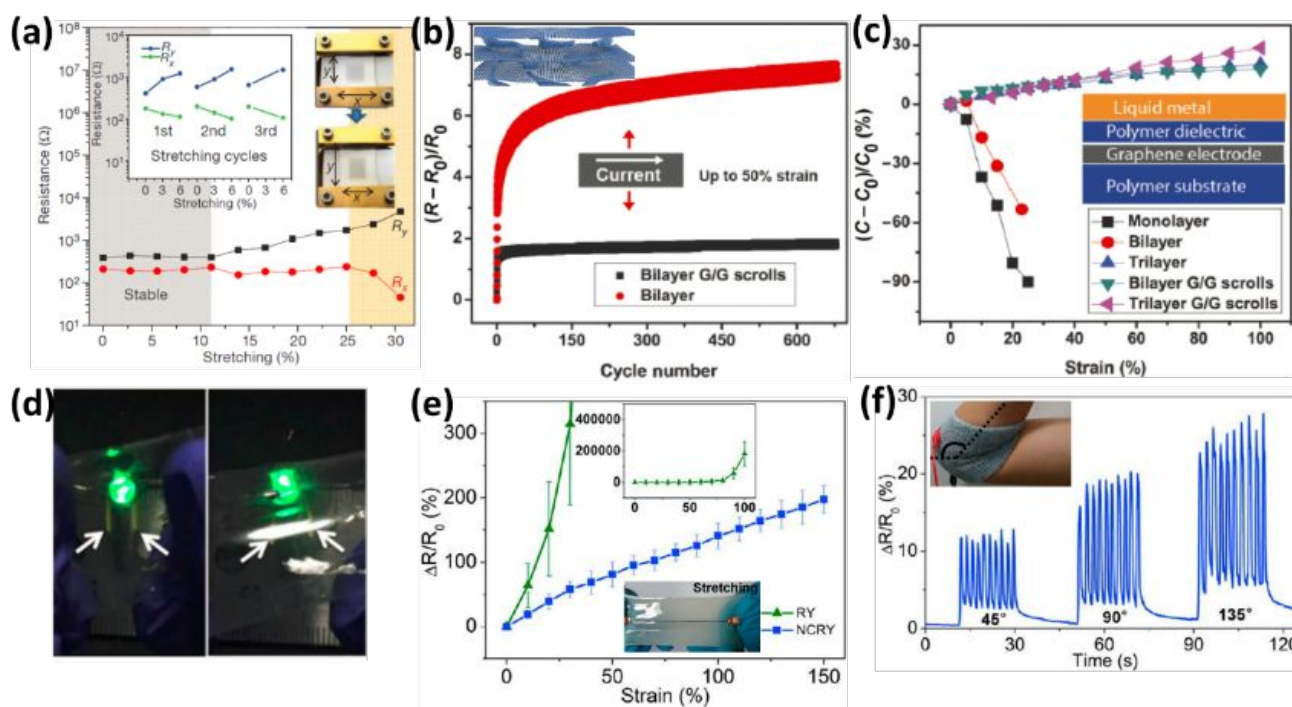


Figure 11. (a) Resistance change of graphene on prestrained PDMS substrate as a function of strain. Insets: Resistance change of graphene on unstretched PDMS substrate and photographs of stretching directions. Adapted with permission.⁶⁶ Copyright 2009, Nature Publishing Group. (b) Resistance change of bilayer graphene and MGG as a function of stretching cycles. Inset: Schematic of MGGs a stretchable electrode. (c) Capacitance change of devices with monolayer, bilayer, trilayer graphene and MGGs electrodes as a function of strain. (d) The all-carbon stretchable and transparent transistor for the switching of LED under 0% (left) and 100% (right) strain. Adapted with permission.¹²² Copyright 2017, American Association for the Advancement of Science. (e) Resistance change of the RY and NCRY sensors as a function of strain. Inset: Photograph of PDMS coated RY sensor under stretching. (f) Resistance change of NCRY sensor under the bending motions. Inset: Photograph of NCRY sensor sewed on the elbow wrap at the angle of 135°. Adapted with permission.³⁷⁸ Copyright 2015, American Chemical Society.

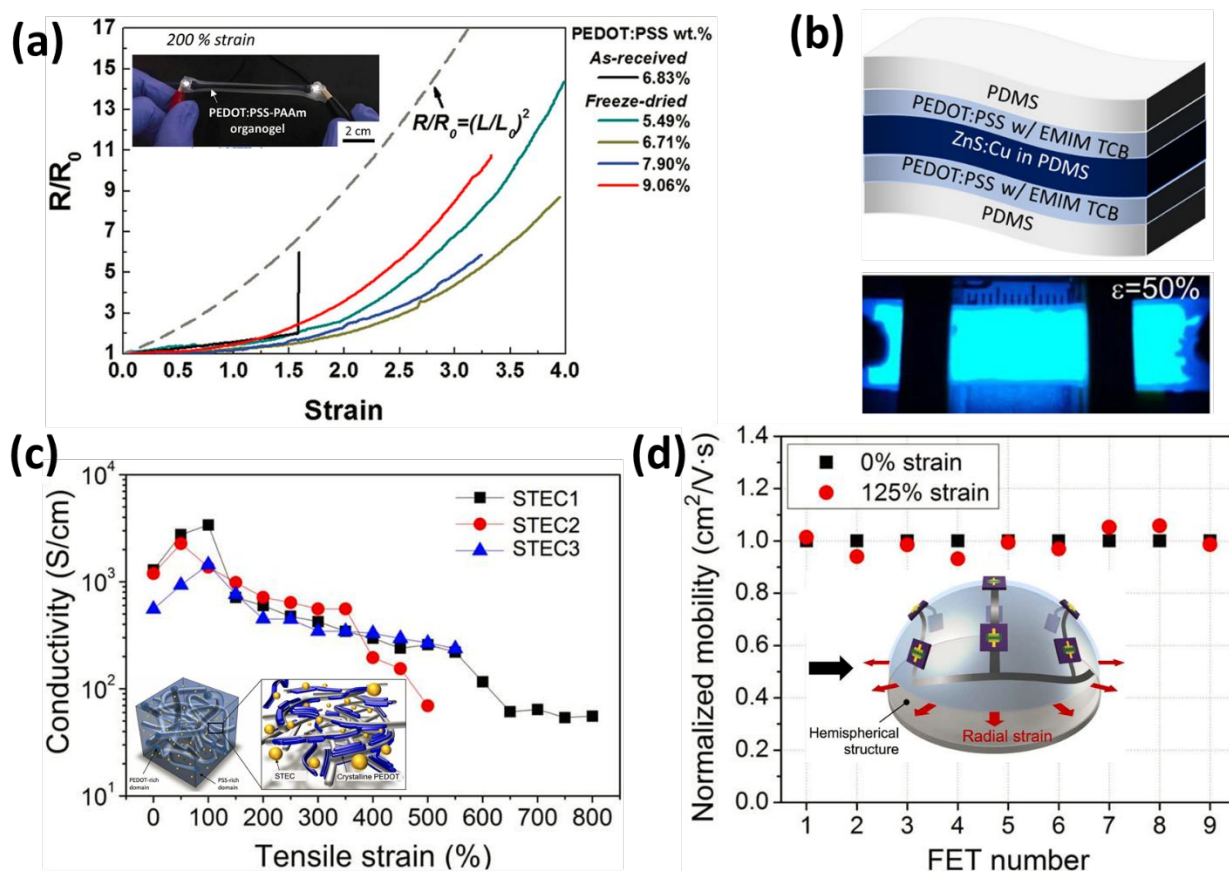


Figure 12. (a) Resistance change of PEDOT:PSS/acrylamide organogels with different weight ratios. Inset: Photograph of two LED lights circuit interconnected with PEDOT:PSS/acrylamide organogel on the Ecoflex substrate under the strain of 200%. Adapted with permission.¹³³ Copyright 2015, Wiley-VCH. (b) Schematic of electroluminescent device sandwiched ZnS:Cu phosphor microparticles/PDMS layer between both PEDOT:PSS/EMIM TCB transparent electrodes (top). Photograph of electroluminescent device under strain of 50% (Bottom). Adapted with permission.¹³⁴ Copyright 2016, American Chemical Society. (c) Conductivity change of PEDOT:PSS composite with various STEC enhancers. Inset: Schematic of PEDOT:PSS composite film with STEC enhancers. (d) The mobility change of 3 x 3 arrays of field-effect transistors interconnected with PEDOT:PSS/STEC between 0% and 125% strain. Inset: Nine rigid field-effect transistor devices under uniformly stretching in all directions. Adapted with permission.¹³⁵ Copyright 2017, American Association for the Advancement of Science.

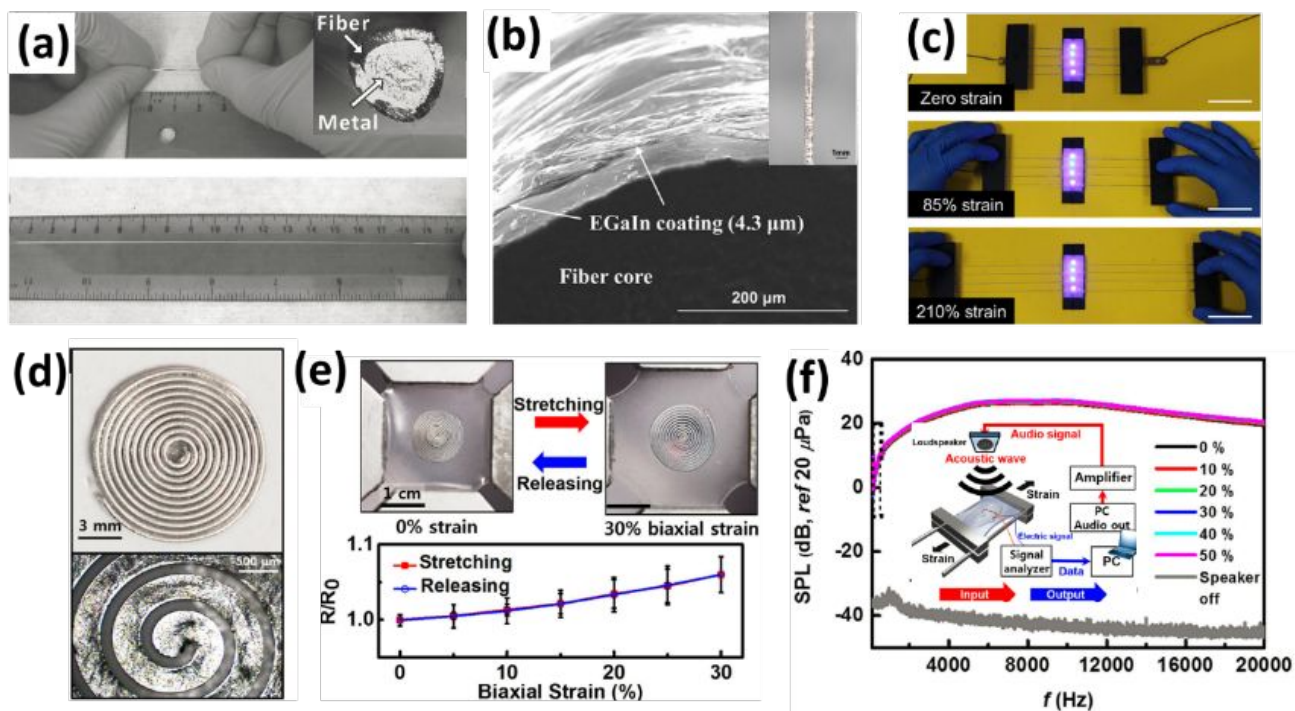


Figure 13. (a) Photograph of stretchable conductive fiber by injecting EGaIn into the core of stretchable hollow fiber before and after stretching. Inset: Cross section of stretchable conductive fiber. Adapted with permission.¹³⁸ Copyright 2013, Wiley-VCH. (b) SEM image of stretchable conductive fiber by dip-coating of EGaIn. Inset: The stretchable fiber coated with EGaIn. (c) Optical images of change in LED light intensity under stretching up to 210% when the stretchable conductive fibers were applied as the interconnects. Adapted with permission.¹⁴² Copyright 2018, IOP publishing. (d) Optical images of stretchable conductive liquid metal coil by injecting Galinstan into a micro-patterned elastomer channel. (d) Photographs of liquid metal coil under biaxial stretching and releasing (Top). Then resistance change of coil as a function of biaxial strain (Bottom). (e) SPL change of microphone as a function of strain. Inset: Schematic of setup for performance measurement of microphone. Adapted with permission.¹⁴³ Copyright 2015, Nature Publishing Group.

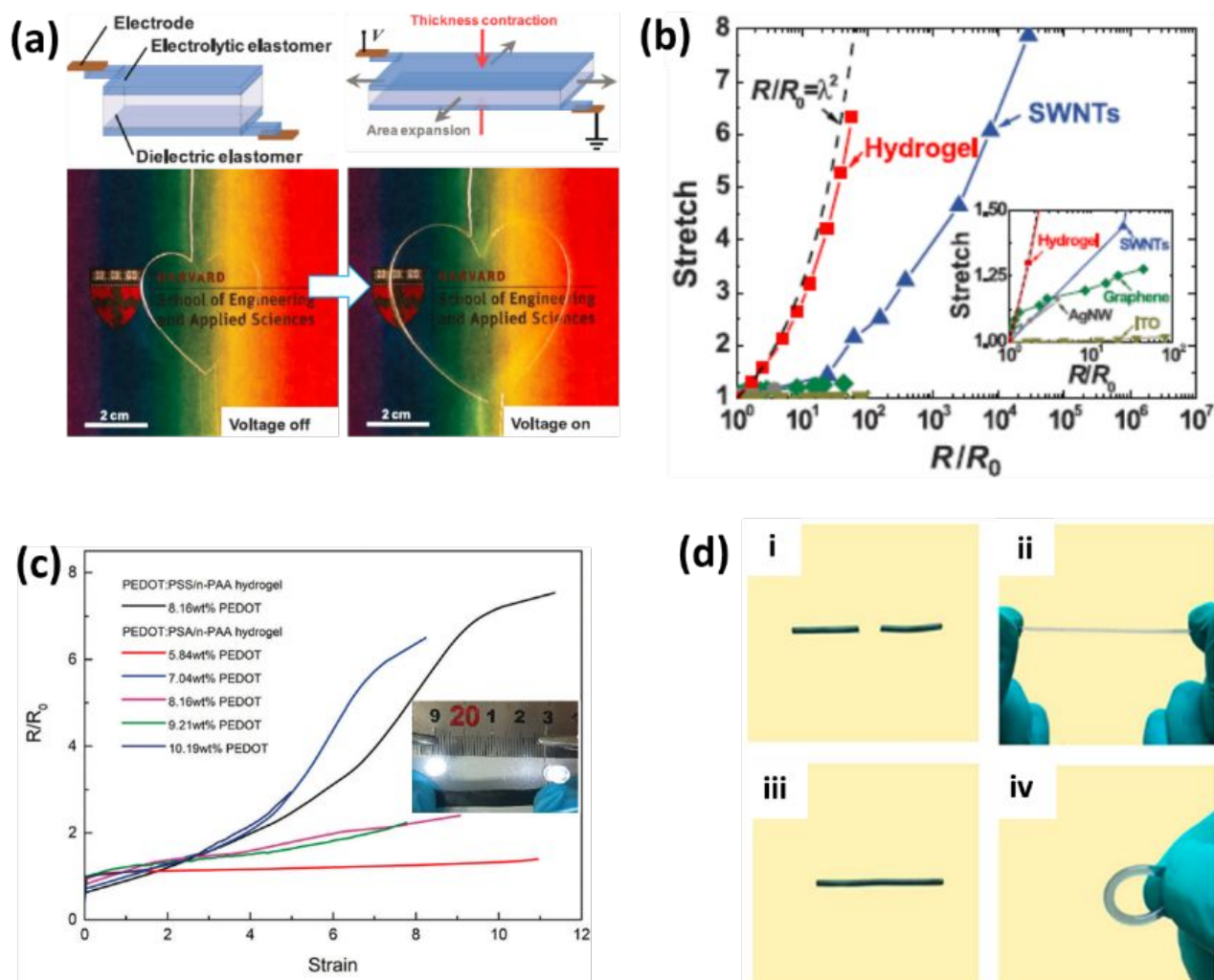


Figure 14. (a) The transparent, high speed and large strain actuator by sandwiching a dielectric elastomer layer between two ionic electrodes of polyacrylamide hydrogel containing a NaCl electrolyte with 100 μm thick before and after applying voltage. (b) Resistance change of hydrogel/electrolyte conductor and electronic conductors as a function of strain. Adapted with permission.⁷² Copyright 2013, American Association for the Advancement of Science. (c) Resistance change of the PEDOT:PSA/n-PAA and PEDOT:PSS/n-PAA hydrogels with different weight ratios as a function of strain. Inset: Two LED lights interconnected with PEDOT:PSA/n-PAA hydrogel at 200% strain. Adapted with permission.¹⁴⁷ Copyright 2018, Royal Society of Chemistry. (d) Photographs of the self-healing performance of PNAGA-PAMPS-PEDOT/PSS hydrogel. Adapted with permission.¹⁴⁸ Copyright 2017, Nature Publishing Group.

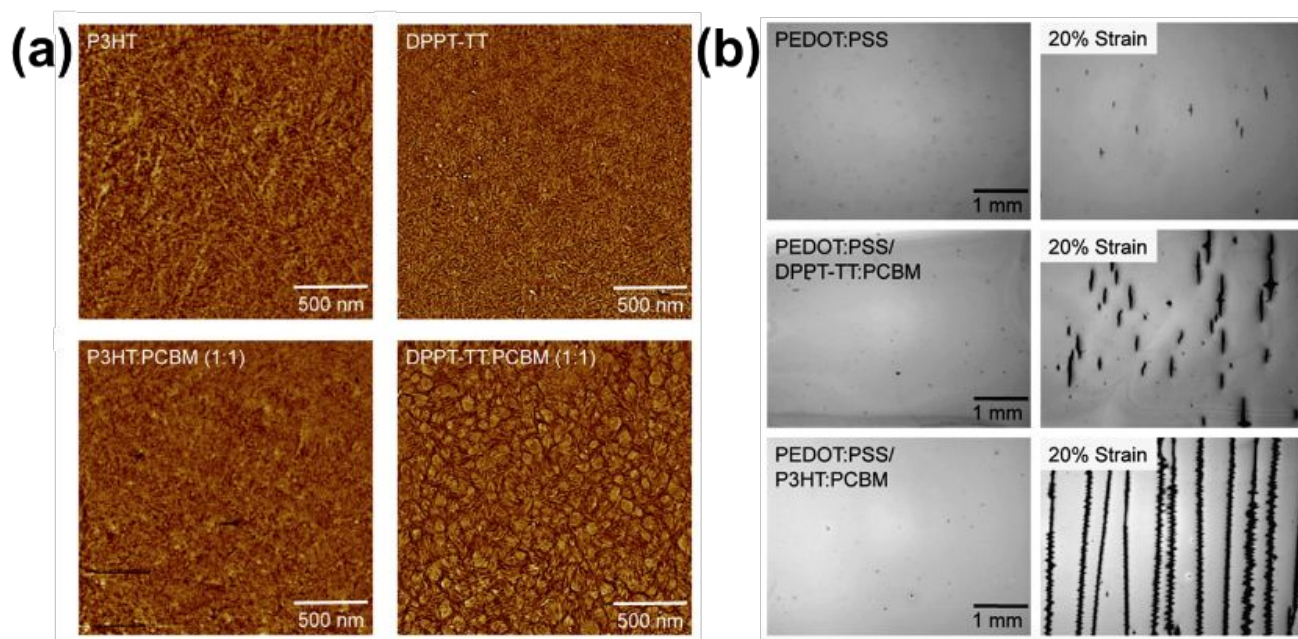


Figure 15. (a) Atomic force microscope (AFM) images of the two pristine conjugated polymers (P3HT and DPPT-TT) and their topography morphology after blending with PCBM (P3HT:PCBM and DPPT-TT:PCBM). (b) Optical microscope images of PEDOT:PSS, PEDOT:PSS/DPPT-TT:PCBM, and PEDOT:PSS/P3HT:PCBM at 0 % and 20 % strain. Adapted with permission.¹⁶⁹ Copyright 2012, Elsevier B.V..

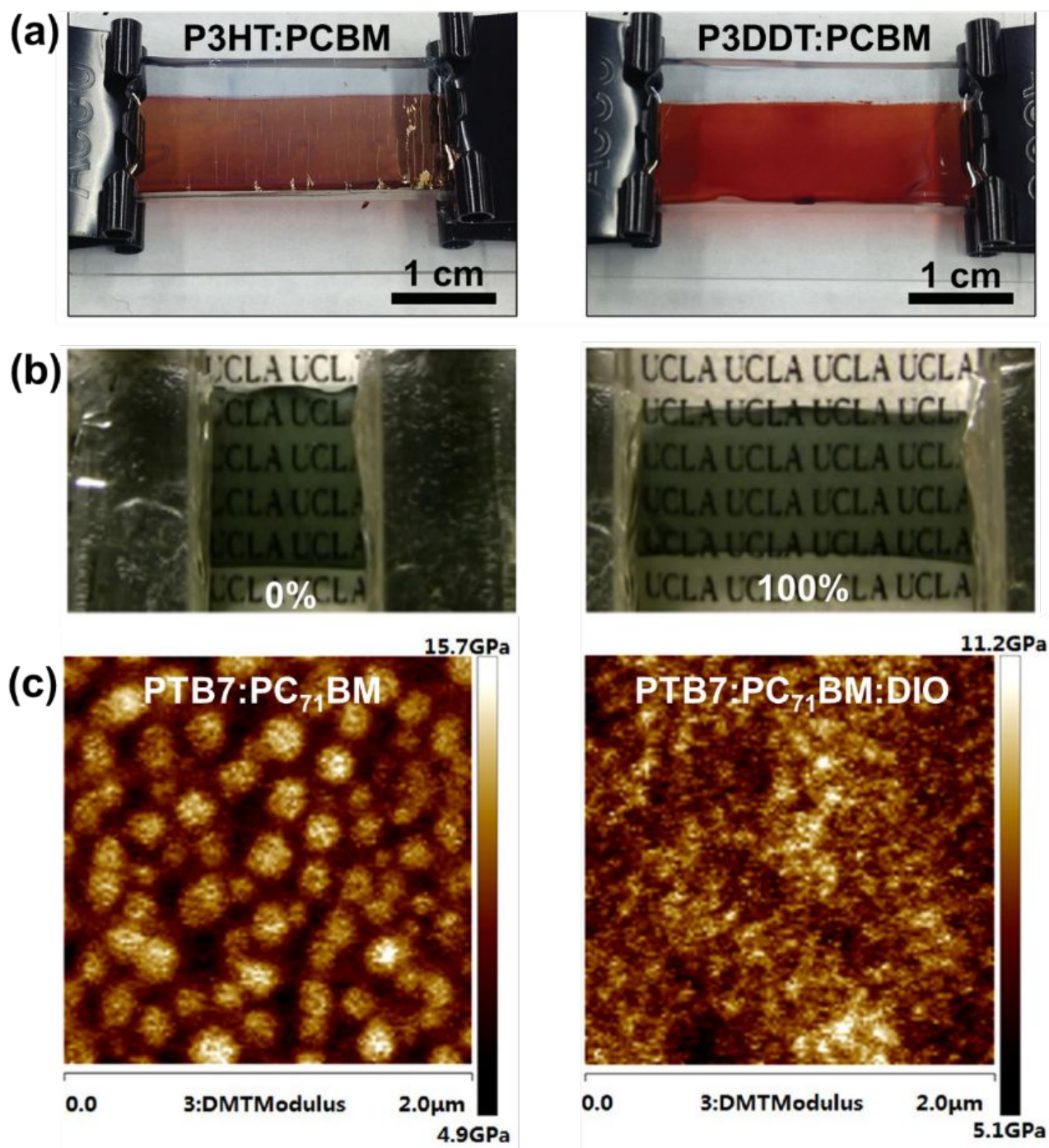


Figure 16. (a) Optical images of P3HT:PCBM and P3DDT:PCBM films under 10% strain. Adapted with permission.¹⁵⁶ Copyright 2013, Wiley-VCH. (b) Optical images of the OPV stretched up to 100%. (c) AFM images of young's modulus map of a PTB7:PC₇₁BM film and a PTB7:PC₇₁BM:DIO film. Adapted with permission.¹⁵⁸ Copyright 2017, American Chemical Society.

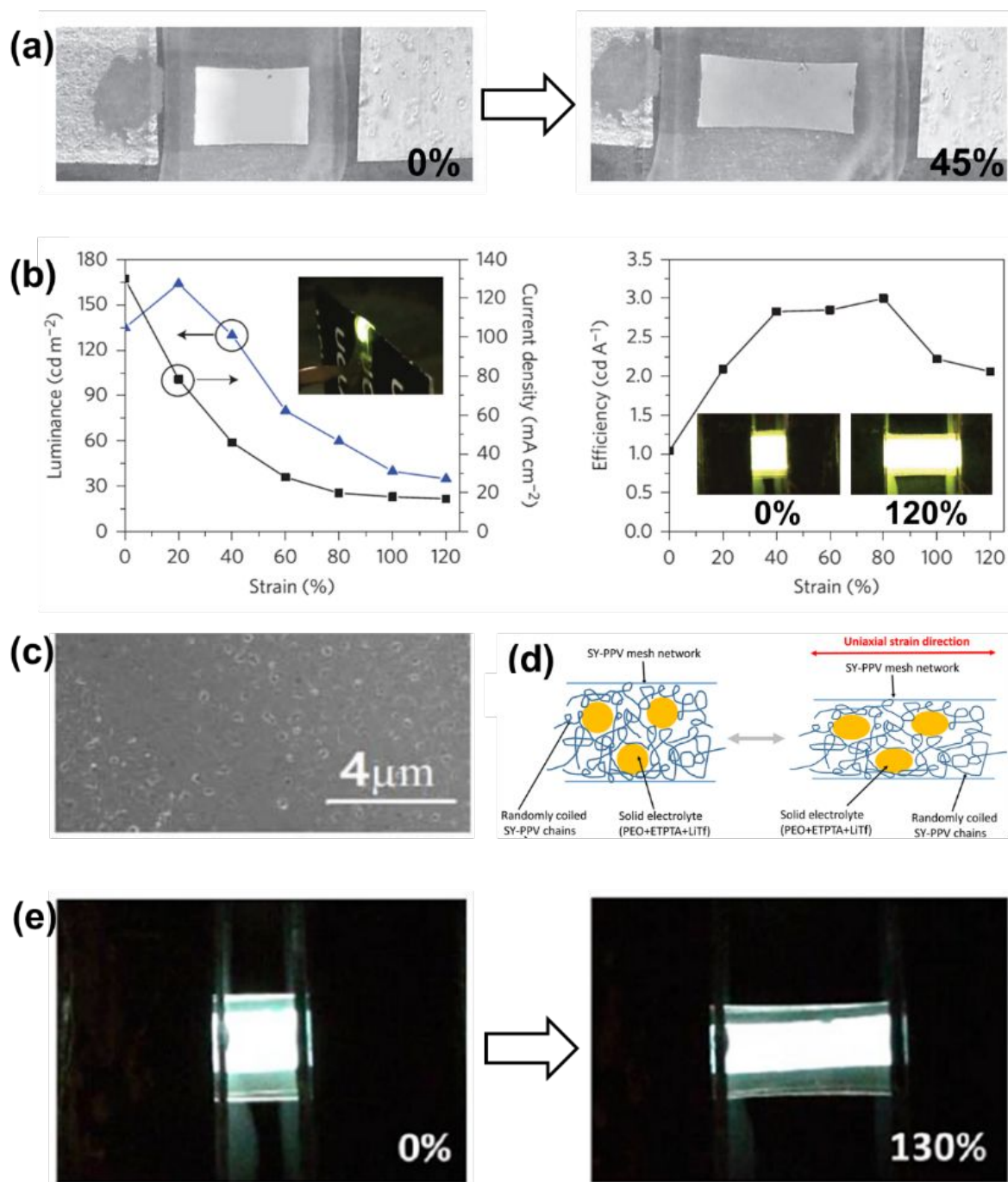


Figure 17. (a) Optical images of a blue OLEC under 0% and 45% strain at 8V. Adapted with permission.¹⁶⁰ Copyright 2011, Wiley-VCH. (b) Device performance of a yellow OLEC device at 12 V under different strain. A photograph of a yellow OLEC wrapped around a 400 μm cardboard is shown in the left inset. The right insets show optical images of a yellow OLEC under 0% and 120% strain. Adapted with permission.³ Copyright 2015, Nature Publishing Group. (c) A SEM image of the SuperYellow:ETPTA:PEO:LiTf blend film (100:15:15:4 by weight percent). (d) Schematic illustration of a SuperYellow:ETPTA:PEO:LiTf blend film under strain. Adapted with permission.¹⁷⁰ Copyright 2016, American Chemical Society. (e) Optical images of a white OLED under 0% and 130% strain driven at 14 V. Adapted with permission.⁴ Copyright 2014, American Chemical Society.

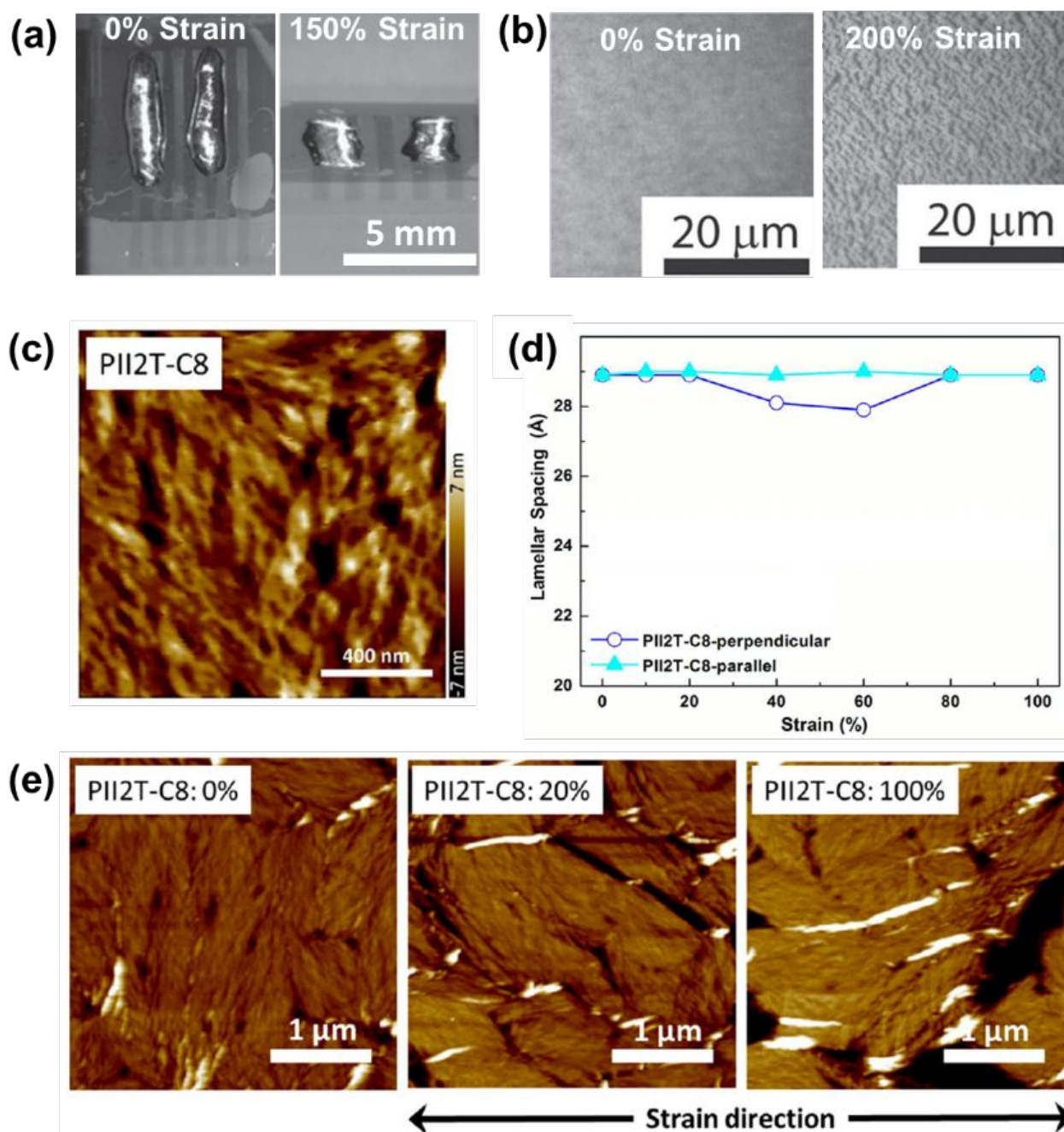


Figure 18. (a) Optical images of a PU/P3HT/PU OFET under 0% and 150% strain. (b) The film morphology of P3HT under 0% and 200% strain. Adapted with permission.¹⁶¹ Copyright 2014, Wiley-VCH. (c) AFM topography images of the polymer film with PII2T main chain and carbosilane side chain (PII2T-C8). The well packing structure of the nanofibrillar morphology can be observed. (d) Lamellar packing spacing of the PII2T-C8 thin film under different applied strain (0-100 %). (e) AFM topography images of the PII2T-C8 thin film under strain. Adapted with permission.¹⁷⁹ Copyright 2016, American Chemical Society.

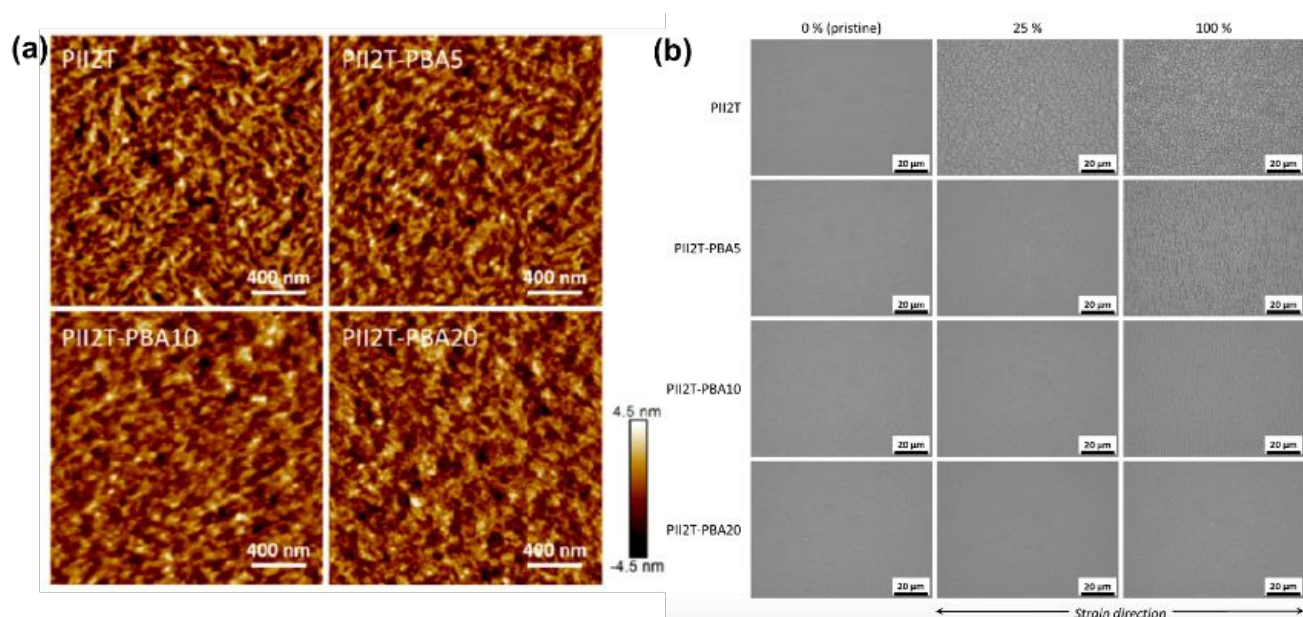


Figure 19. (a) AFM topography images of the pristine PII2T film, the polymer film of PII2T incorporated with 5 % PBA side chain (PII2T-PBA5), the polymer film of PII2T incorporated with 10 % PBA side chain (PII2T-PBA10), and the polymer film of PII2T incorporated with 20 % PBA side chain (PII2T-PBA20). (b) Optical images of pristine PII2T, PII2T-PBA5, PII2T-PBA10, PII2T-PBA20 under 0 %, 25 %, and 100 % strain. Adapted with permission.¹⁸² Copyright 2017, American Chemical Society.

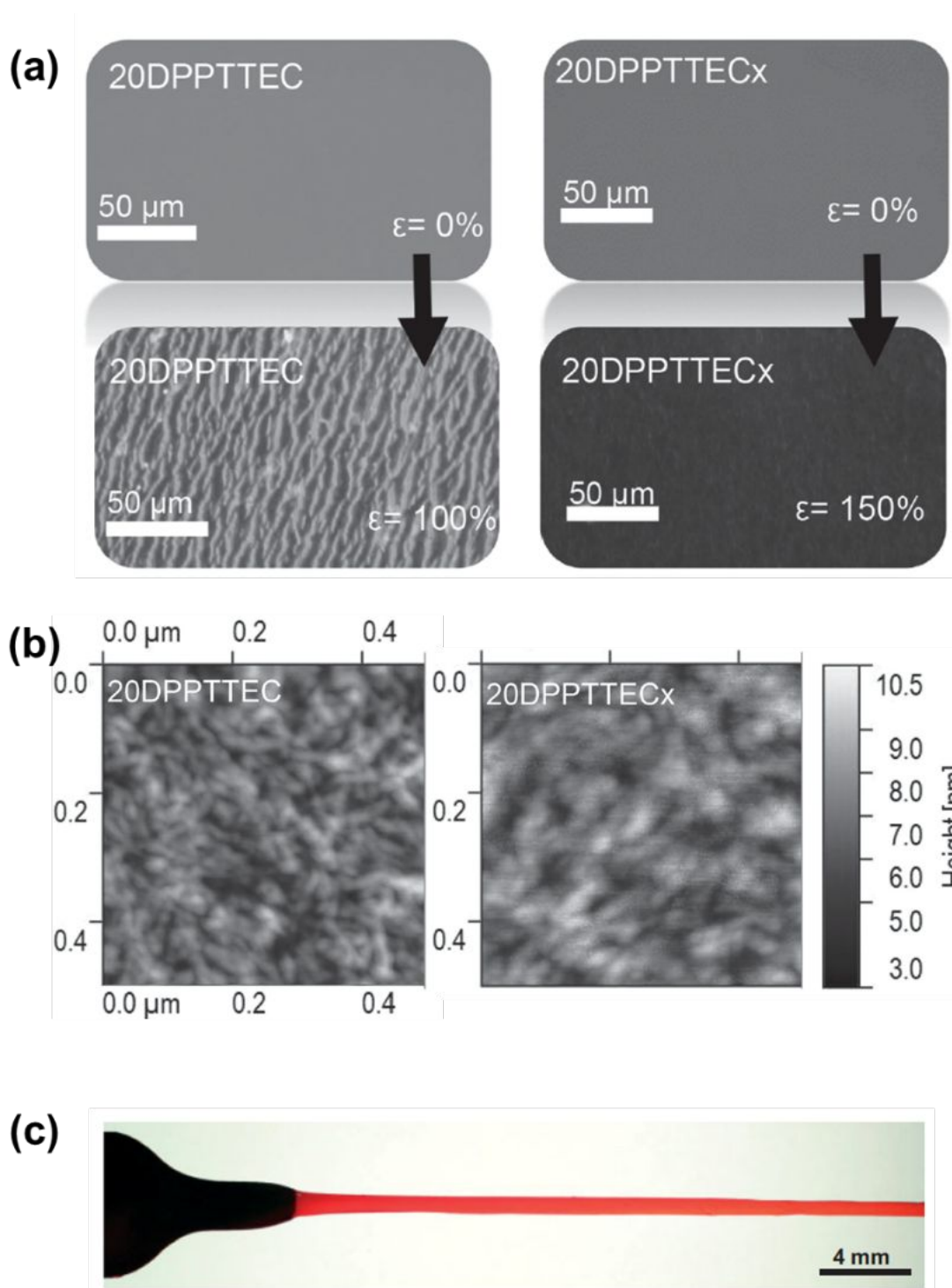


Figure 20. (a) Optical microscope images of both 20DPPTTEC, and 20DPPTTECx film at 0% and 20% strain. (b) AFM topography images of 20DPPTTEC and 20DPPTTECx. The non-crosslinked film shows high crystallinity domain whereas the crosslinked film shows decrease in nanofibrillar packing. Adapted with permission.¹⁸⁵ Copyright 2016, Wiley-VCH. (c) The optical image of the P3HT-PE film stretched up to 600%. Necking was observed in the image which is due to plastic deformation of the film. Adapted with permission.¹⁶⁸ Copyright 2007, Wiley-VCH.

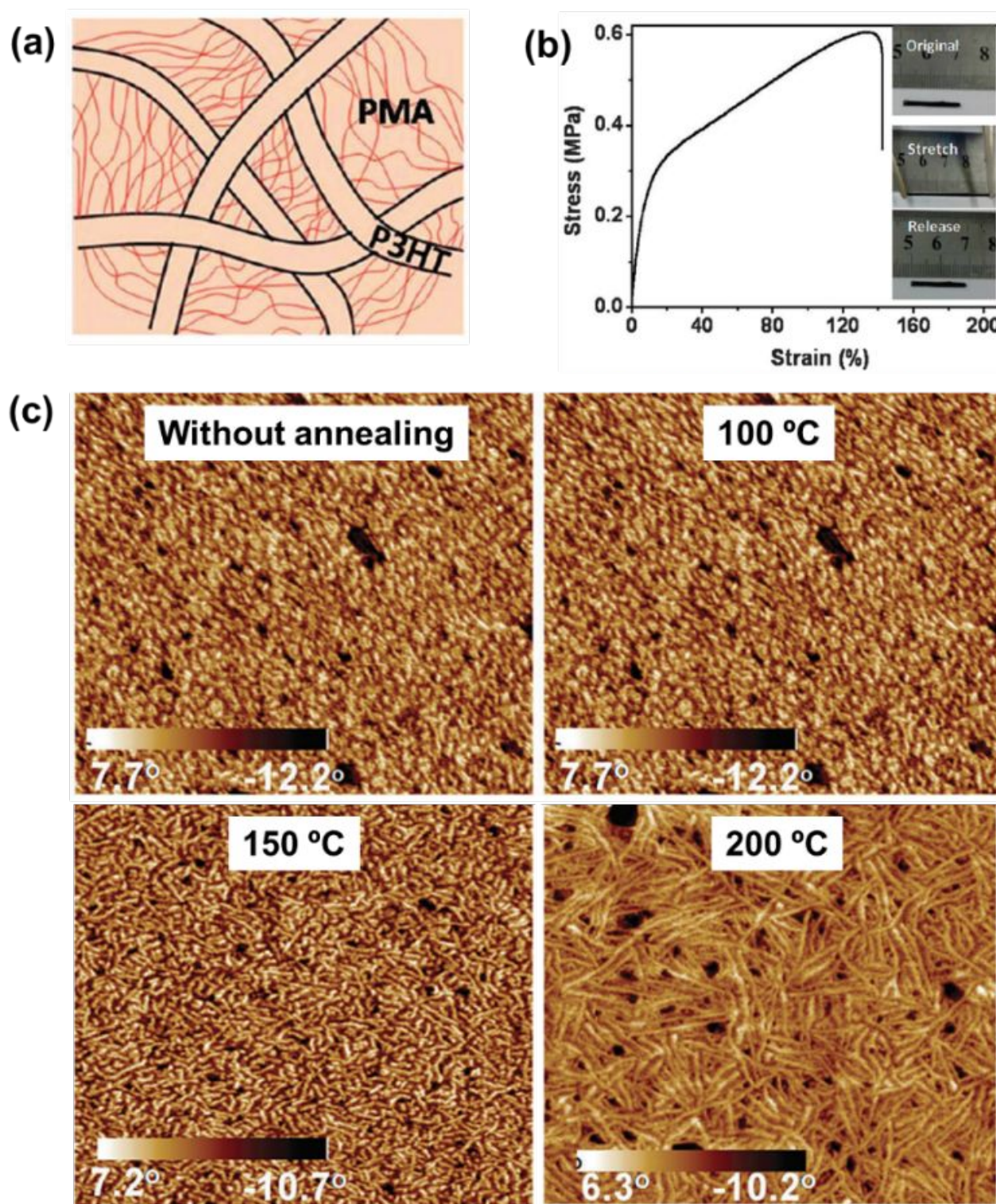


Figure 21. (a) The schematic illustration of the morphology of the P3HT-PMA-P3HT triblock copolymer. (b) The stress-strain curve of the P3HT-PMA-P3HT triblock copolymer. (c) AFM topography images of the P3HT-PMA-P3HT film under different annealing temperatures. Adapted with permission.¹⁶⁷ Copyright 2015, Royal Society of Chemistry.

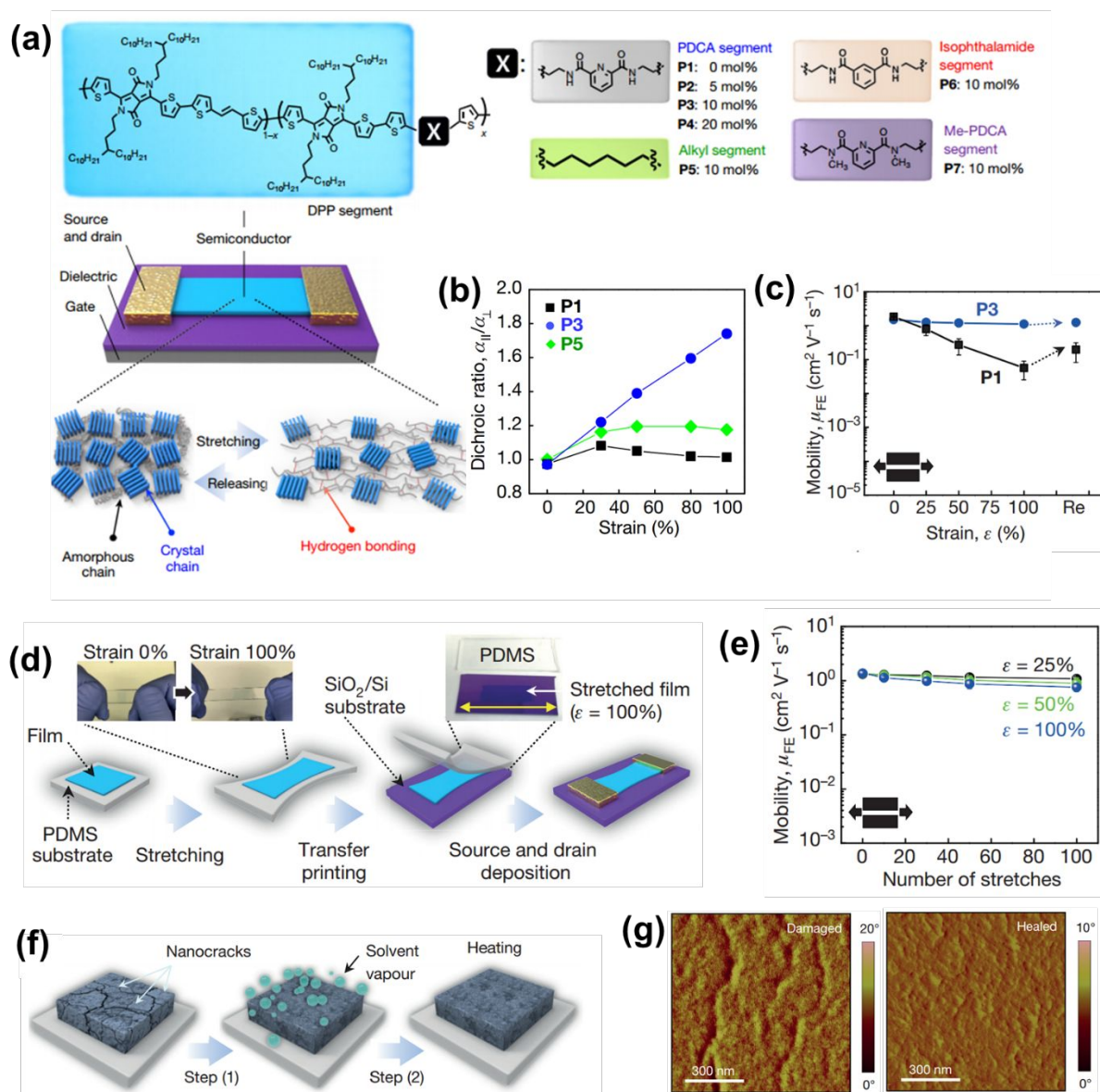


Figure 22. (a) Chemical structure of P1 to P6 semiconductor polymers and the schematic illustration of the stretching mechanism of the semiconductor film through hydrogen bonding. (b) Dichroic ratio of P1, P3, and P5 polymers under strain (0–100%). (c) Field effect mobility of P1 and P3 polymers under various strain. (d) Schematic illustration of the fabrication process of the TFT. (e) Schematic illustration of the polymer healing process through solvent vapor treatment. (f) Field-effect mobility versus stretching-releasing cycles under various strain. Adapted with permission.⁴⁹ Copyright 2016, Nature Publishing Group.

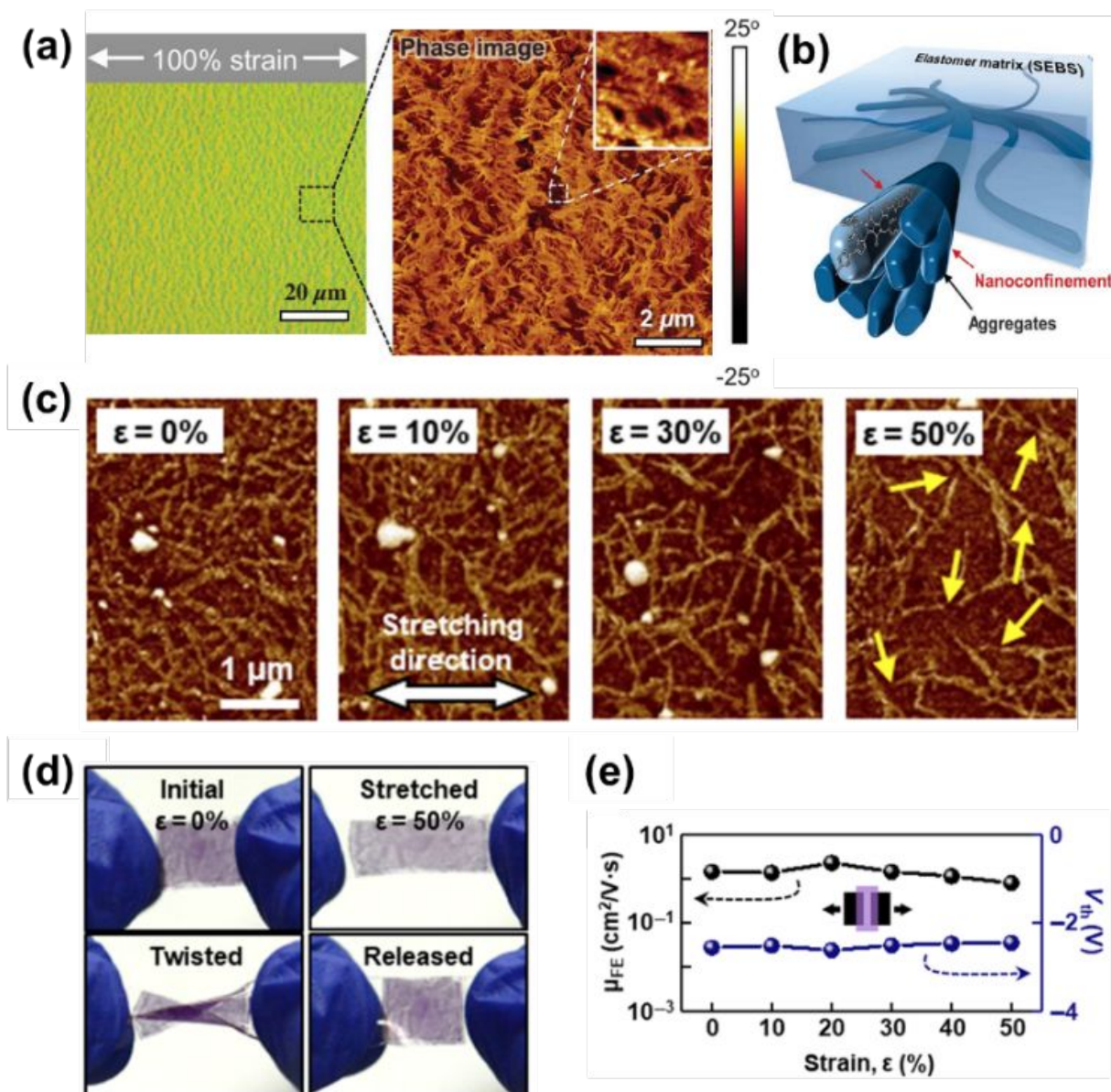


Figure 23. (a) Optical microscope image of the DPPT-TT/SEBS film under 100% strain and its AFM images. (b) A schematic illustration of the nanoconfinement morphology embedded inside a soft elastomer matrix. Adapted with permission.¹⁶⁴ Copyright 2017, American Society for the Advancement of Science. (c) AFM phase images of P3HT-NF percolated PDMS rubber composite under various strain (0 – 50%). The yellow arrows point at the rupture location of P3HT-NF.⁵⁰ (d) Photographs of P3HT-NF percolated PDMS composite film under different types of mechanical deformation.⁵⁰ (e) Mobility and threshold voltage under various mechanical strain.⁵⁰ Adapted with permission.⁵⁰ Copyright 2017, American Society for the Advancement of Science.

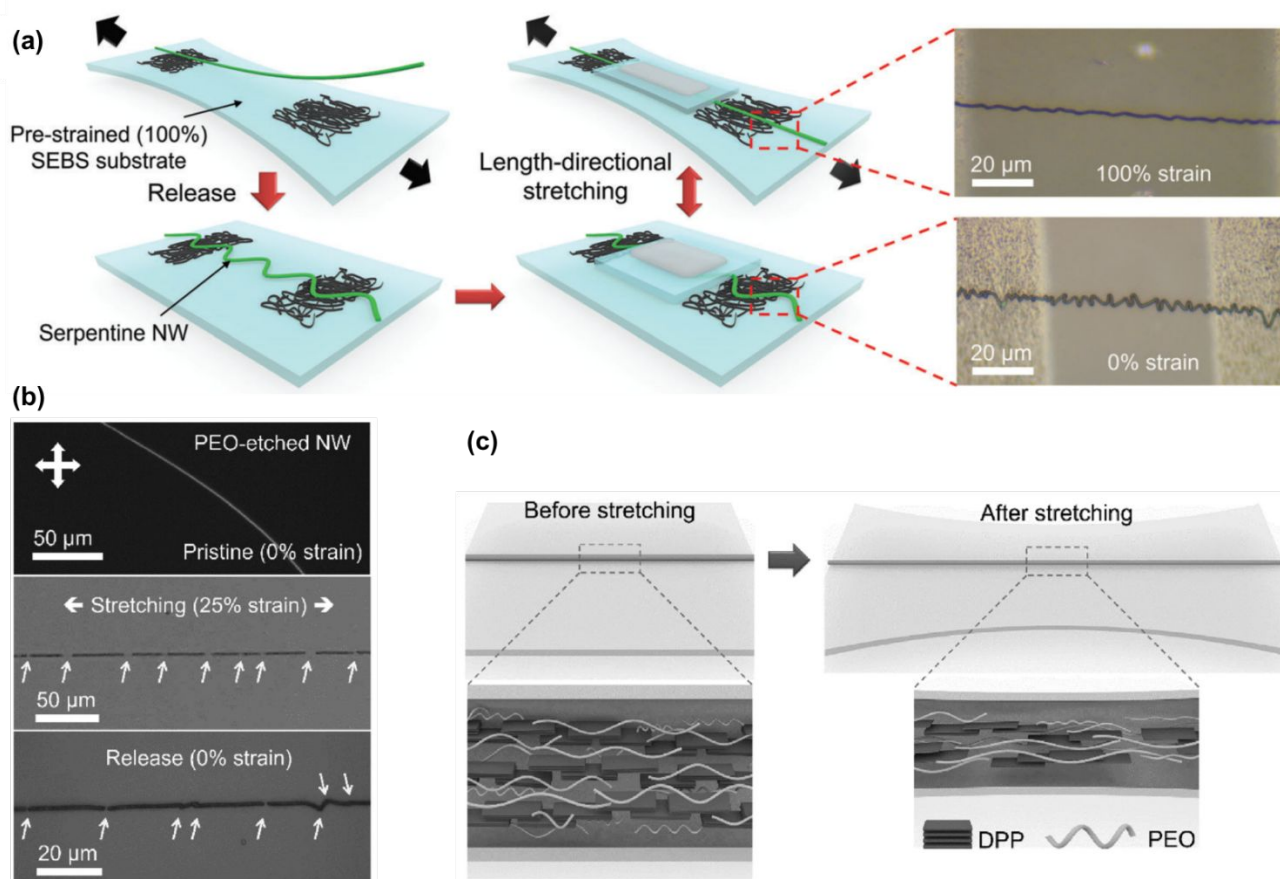


Figure 24. (a) Schematic illustration of deformable transistor with serpentine FT4-DPP:PEO nanowires. Optical microscope images show the serpentine FT4-DPP:PEO nanowires at 0% strain and 100% tensile strain. (b) Polarized optical microscope image (upper) and optical microscope image (middle and lower) of FT4-DPP nanowire (PEO was etched away) under 0% strain (upper), 25% strain (middle), and release back to 0% strain (lower). The arrows point at broken region on the nanowire. (c) Schematic illustration of the morphologies of FT4-DPP:PEO composite nanowires at its pristine state (left) and under stretching state (right). Adapted with permission.¹⁹⁶ Copyright 2018, Wiley-VCH.






















V_G	-2.0 V	-4.0 V	-4.5 V	-5.0 V	-6.0 V	-7.0 V	-8.0 V
TFT under 0% strain	0 cd m ⁻² 	6.9 cd m ⁻² 	50 cd m ⁻² 	84 cd m ⁻² 	112 cd m ⁻² 	183 cd m ⁻² 	196 cd m ⁻² 
TFT under 20% strain	0 cd m ⁻² 	4.5 cd m ⁻² 	33 cd m ⁻² 	51 cd m ⁻² 	98 cd m ⁻² 	110 cd m ⁻² 	120 cd m ⁻² 
TFT under 30% strain	0 cd m ⁻² 	0 cd m ⁻² 	7.5 cd m ⁻² 	33 cd m ⁻² 	48 cd m ⁻² 	57 cd m ⁻² 	63 cd m ⁻² 

Figure 25. Luminance of an OLED powered by a stretchable TFT with different strains (along channel length direction) and inputs. Drain supply is -4.0 V. Adapted with permission.²⁶⁴ Copyright 2015, Nature Publishing Group.

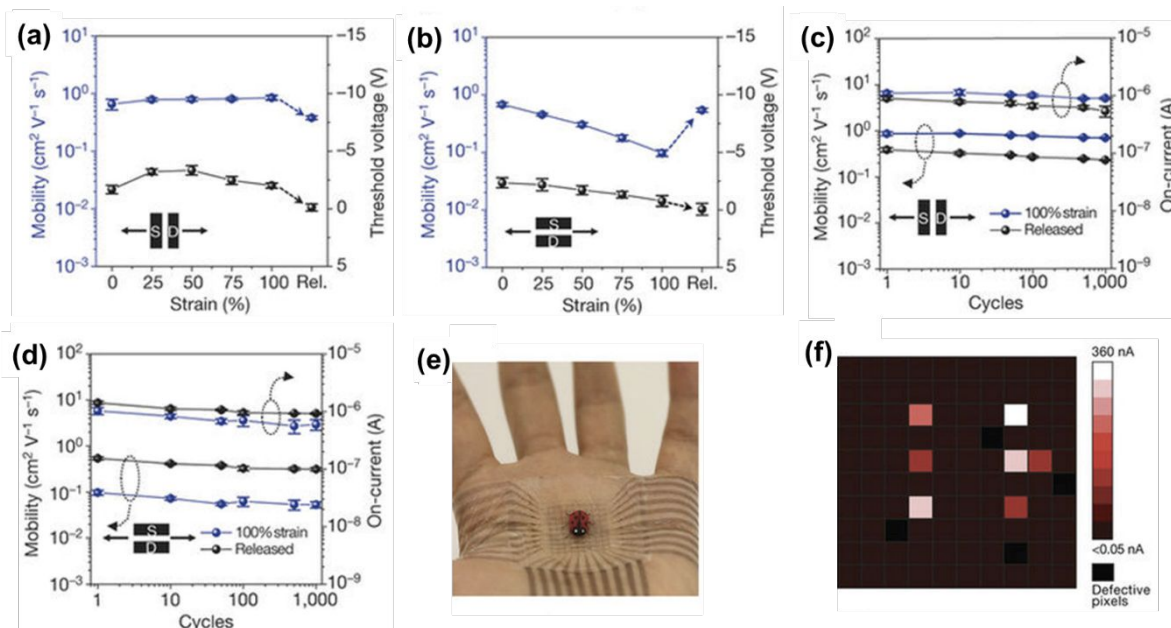


Figure 26. Device performance of the intrinsically stretchable transistor arrays and coupled tactile sensors. Mobilities and threshold voltages when the transistor was stretched (a) parallel and (b) perpendicular to the channel direction. “Rel” presents the value after the device was released from 100% strain. (c, d) Mobilities and on currents of the device for 1 000 stretching cycles at 100% and 0% strain when the transistor was stretched parallel and perpendicular to the channel direction. (e, f) Image and on current map of the coupled flexible tactile sensor matrix with the accurate detection of legs from the artificial lady bug. Adapted with permission.²⁰⁹ Copyright 2018, Nature Publishing Group.

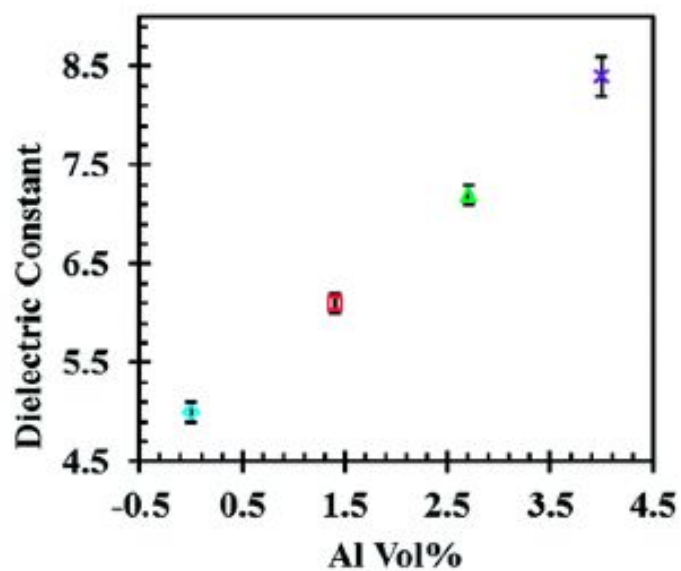


Figure 27. Dielectric constants change with increased Al_2O_3 concentration. Measured at 200 V AC and 400 Hz. Adapted with permission.²⁹⁰

Copyright 2014, Royal Society of Chemistry.

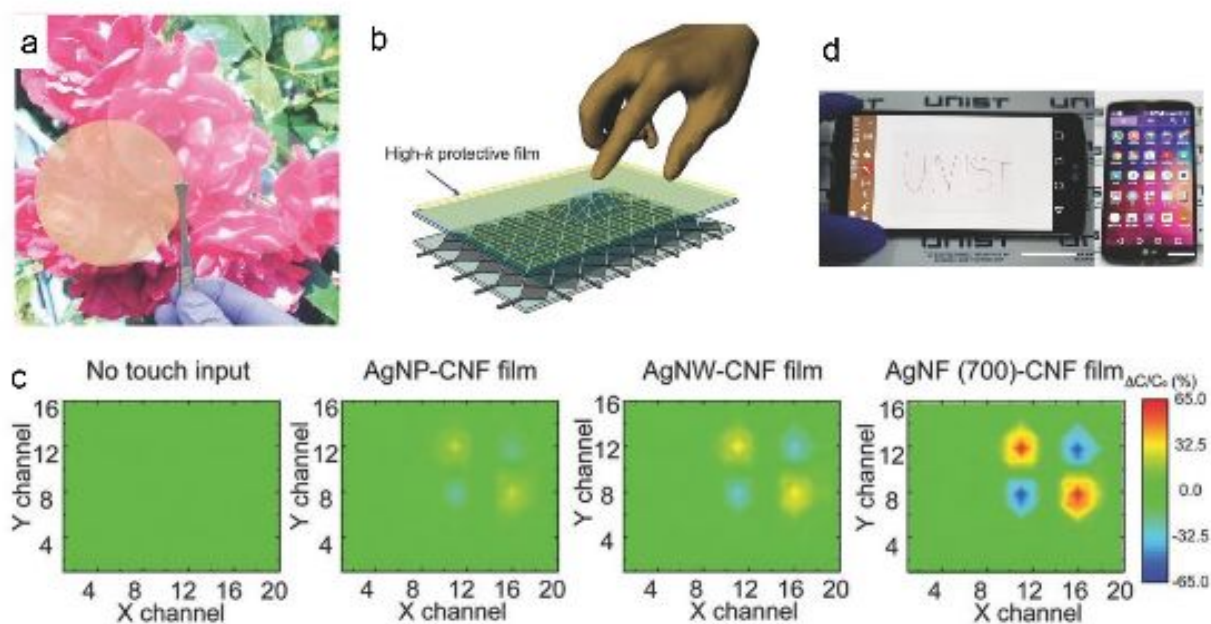


Figure 28. Comparison of cellulose-nanofiber films containing 1.2 wt% AgNPs, AgNWs and AgNFs. (a) Optical transmittance of film with AgNPs (left), AgNWs (middle) and AgNFs (right). (b) Schematic illustration of a capacitive touch sensor panel covered by high-k layer. (c) 2D mappings of capacitance change on each touch sensitive panel with fingertip touch. (d) Photographs of smart phone with glass replaced by AgNFs imbedded film. Adapted with permission.²¹¹ Copyright 2017, Wiley-VCH.

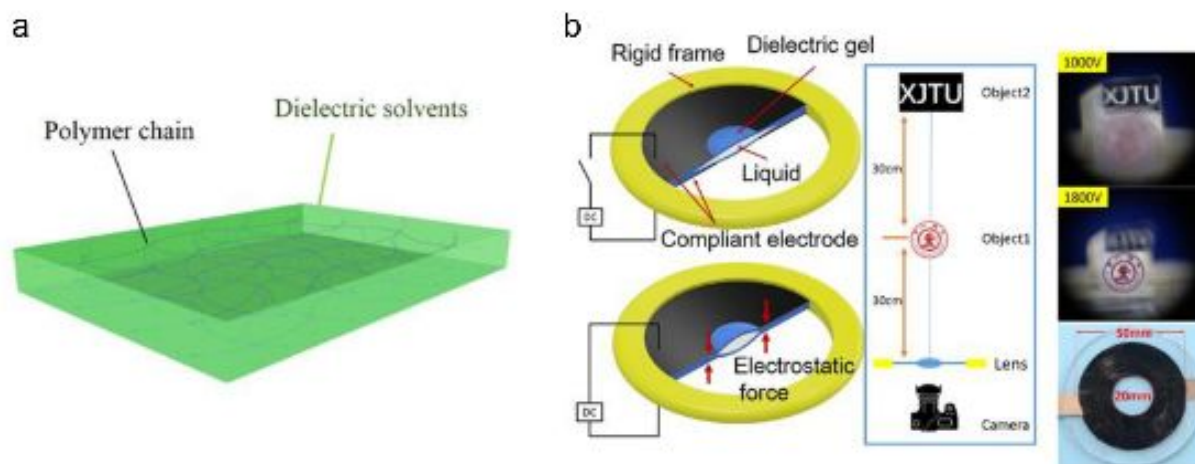


Figure 29. Dielectric gel. (a) Schematic illustration of a dielectric gel (b) Demonstration of a bioinspired lens with tunable focal length. Adapted with permission.³¹¹ Copyright 2018, Nature Publishing Group.

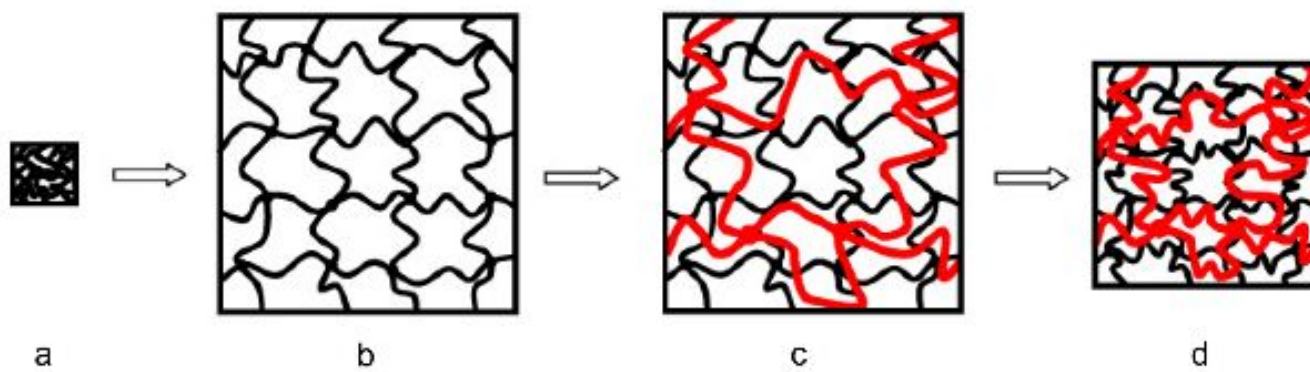


Figure 30. Scheme of the fabrication process of an elastomer with IPN structure. (a) Original acrylic film. (b) Biaxially pre-straining (400% x 400%). (c) Added and cured the additives to fabricate an interpenetrating network. (d) The interpenetrating network preserved most of the pre-strain after releasing the external force. Adapted with permission.³³⁹ Copyright 2007, IOP Publishing.

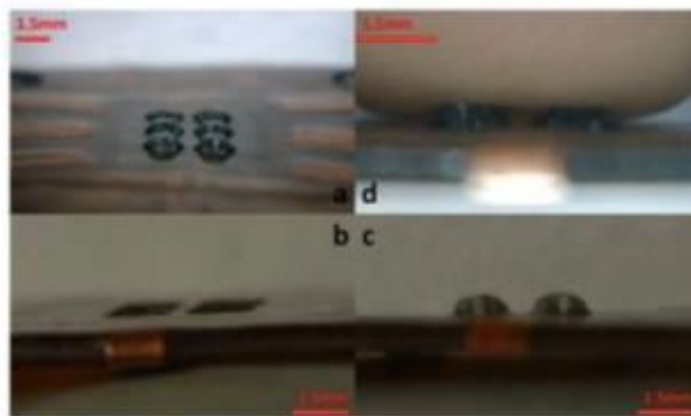


Figure 31. A six-dot Braille character display. (a) All six dots were at ON state. (b) Side view of OFF state. (c) Side view of ON state. (d) Braille character (ON state) was touched by a human finger. Adapted with permission.²²⁵ Copyright 2012, SPIE.

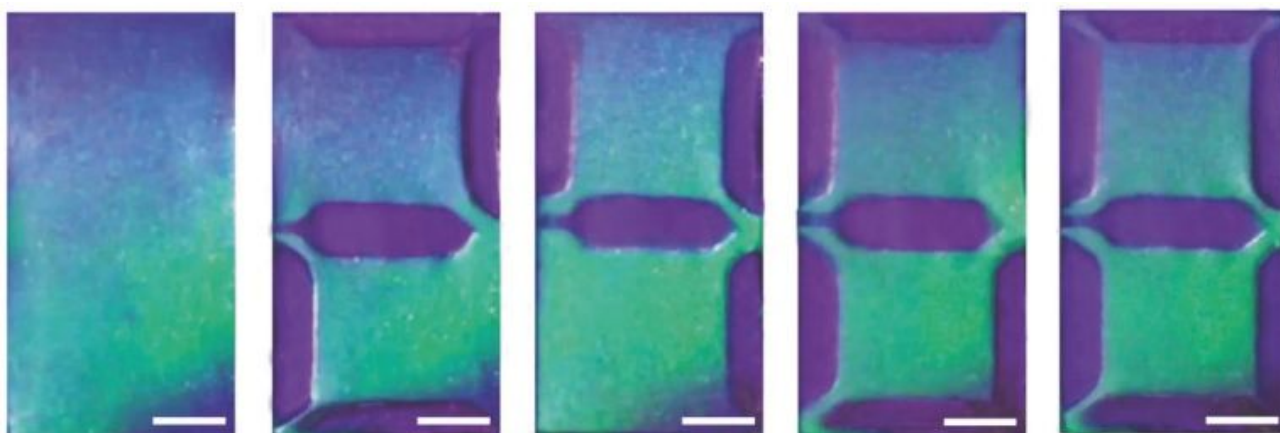


Figure 32. Demonstration of photonic rewritable papers showing selected digits. Scale bars are 3mm in length. Adapted with permission.³⁵⁷

Copyright 2018, Wiley-VCH.

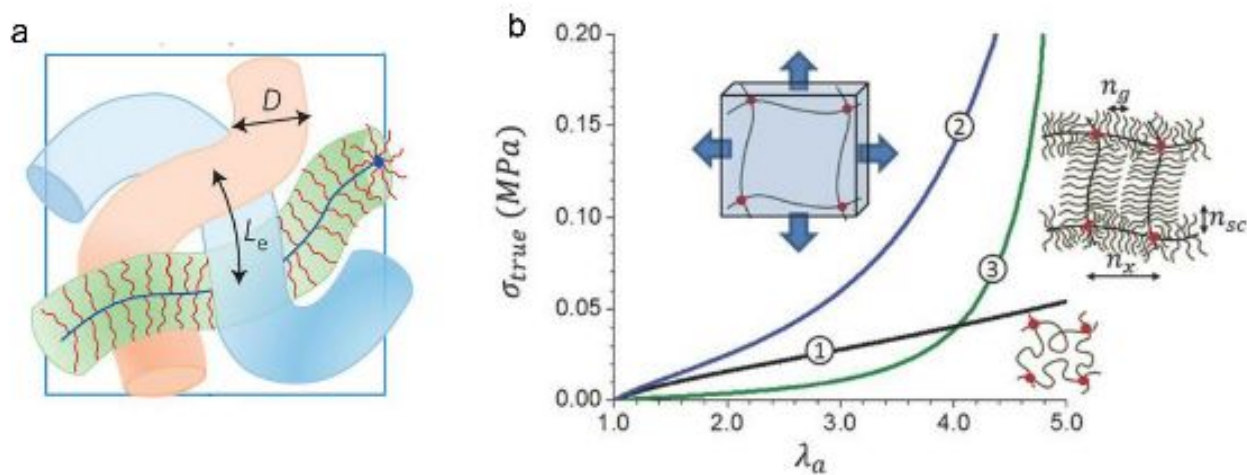


Figure 33. Structure illustration and mechanical properties of bottlebrush-structured elastomers. (a) Illustration shows the interior brush-like structures to lower the entanglement density of polymer backbones. Adapted with permission.³⁶⁵ Copyright 2016, Nature Publishing Group. (b) True stress as a function of areal expansion for 1: a conventional elastomer with linear elasticity, 2: a biaxially pre-stained elastomer that exhibits strain-stiffening, 3: a bottlebrush structured elastomer. Adapted with permission.³⁵¹ Copyright 2016, Wiley-VCH.

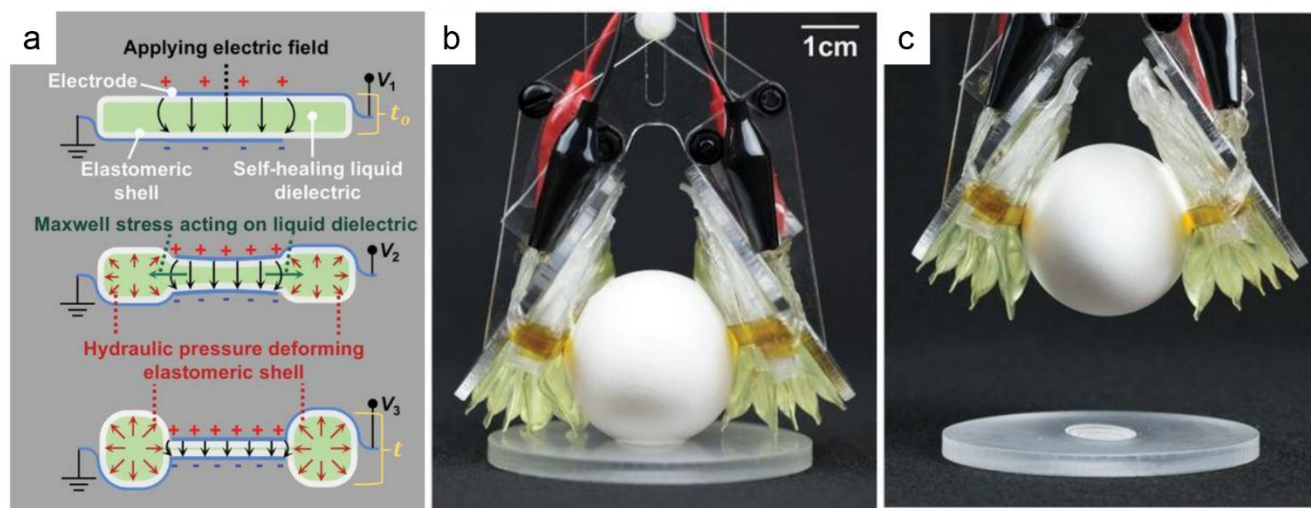


Figure 34. Self-healing donut-shape elastomer with liquid dielectrics. (a) Schematic of actuation process through pull-in transition. (b) A soft gripper made of two stacks of actuators moved a raw egg. Adapted with permission.³⁷¹ Copyright 2018, American Association for the Advancement of Science.



Figure 35. Demonstrations of energy harvesting generators. (a) Structure of a multilayer triboelectric nanogenerator. (b) Top: Demonstration of self-powered shoes that are based on multilayer triboelectric generators with the function of pedometer and fitness track enabled. Bottom: The voltages of energy storage unit while the nanogenerators were driving the pedometer and the fitness tracker. Adapted with permission.²²⁰ Copyright 2017, Wiley-VCH. (c) 20 LEDs were powered by tapping on a triboelectric nanogenerator when the generator was (left) relaxed and (middle) stretched. Right: An LCD screen was driven by a transparent nanogenerator with finger pressing. Adapted with permission.²²² Copyright 2017, American Association for the Advancement of Science.

Table 1. Summary of performance and applications of intrinsically stretchable conductive materials.

Design Rules	Materials	Rs (Ω/sq)/T (%)	Max Strain (%)	Applications	Ref.
Metal wires on/embedded into stretchable polymer substrates	AgNWs/PDMS	30/85	60	Heater	84
	AgNWs/PU	1.8/50	80	Wearable sensor	87
	AgNWs/Poly(TBA-co-AA)	88.6/80	140	Actuator	92
	AgNWs/PEDOT/DA	15/78	100	Healable conductor	95
	AgNWs/PU	44.7/82.7	60	Capacitive sensor	93
	AgNWs/Poly(acrylate)	17.25/80	50	Stretchable electrode	80
	CuNWs/PDMS	12/80	10	Stretchable electrode	379
	CuNWs/PU	8.5/70	90	Stretchable electrode	105
	CNTs/PDMS	500/90	120	Capacitive sensor	380
	Graphene/SEBS	637/95	120	Stretchable electrode	122
Carbon materials/conductive polymer on stretchable polymer substrates	Graphene/Optically clear adhesive	92/84.5	30	Actuator	120
	Graphene/PDMS	280/80	30	Stretchable electrode	66
	Graphene/AgNWs/PDMS	33/94	100	Stretchable electrode	119
	PEDOT:PSS/PDMS	46/82	10	Stretchable electrode	381
	Stretchable conductive polymer/CNTs film	PEDOT:PSS	30/90	125	Stretchable interconnect
	CNTs Sheet	1000/78	200	Loudspeaker	65

Table 2. Summary of performance of stretchable semiconductor materials.

Design Rule	Materials	Morphology Controls	Stretchability	Mobility at strain of 0% [$\text{cm}^2\text{V}^{-1}\text{S}^{-1}$]	Applications	Ref.
Maintain electrical properties while lower elastic modulus	P3DDT:PCBM	Long alkyl chain	10%	-	OSC	156
	PTB7:PC ₇₁ BM:DIO	Small grain domains	100%	-	OSC	158
	OF-B/PEO-DMA/LiF	-	45%	-	OLEC	160
	SuperYellow:ETPTA:PEO:LiF	Crosslinking network	120%	-	OLEC	3
	WLEP:OXD-7	IPN	130%	-	OLED	4
	Microcracked P3HT	Microcracks	265%	3.4×10^{-2}	OFET	161
	PII2T	-	100%	50.7×10^{-2}	OFET	163
	PII2T-C8	Lamellar packing	100%	8.06	OFET	185
	PII2T-PBA	Reduce crystallinity	100%	0.8	OFET	182
	20DPPTTECx	Crosslinking network	150%	OSC	OFET	185
	P3HT-PE	Reduce crystallinity	600%	2×10^{-2}	OFET	168
	P3HT-PMA-P3HT	Nanofibrillar network in rubbery matrix	140%	9×10^{-4}	OFET	167
	DPP-DMPA (P3)	Dynamic non-covalent network	100%	0.66	OFET	49
	DPPT-TT:SEBS	Nanoconfinement	100%	0.59	OFET	164
	P3HT-NF/PDMS	Nanofibril percolated rubber matrix	50%	1.4	OFET	192
	FT4-DPP:PEO	Nanowires networks	100%	>8	OFET	2
	Semiconducting CNT	Nanowire networks	100%	0.18	OFET	162

SWCNT Nanowire networks 50% ~30 OFET 46

Table 3. Summary of performance and morphological control methods of intrinsically stretchable dielectric materials.

Focus	Materials	Inclusion	Morphology Controls	Dielectric Constant	Actuation Performance	Applications	Ref.
	Silicone	Poly(3-hex-ylthiophene)	Polar group	2000@1Hz	7.6% @ 8 kV/mm	Soft Robotic	273
	PU-co-PEG	PEG diacrylate	Polar group	13@12Hz	20% 1000 cycles*	TFT	276
	SEBS	Crosslinked azid	Polar group	2.5@100Hz	100% 1000cycles*	TFT	209
	PDMS+PU IPN network	tetramethyldisiloxane moieties + carboxyl groups	IPN	12@1Hz	7.1% @ 200 kV/mm	Soft Robotic	281
	PDMS	BaTiO ₃ nanoparticles	Inorganic nanofillers	9@100Hz-1MHz	50% 1000cycles*	TFT	266
	PU	PolyCuPc	Inorganic nanofillers	800@1Hz	9.3% @ 20 kV/mm	Soft Robotic	289
	Acrylate copolymer	Al ₂ O ₃	Inorganic nanofillers	8.5@100Hz	56% area strain@ 140 kV/mm	Soft Robotic	290
Increase dielectric constant	P(VDF-TrFE)	CuPc	Inorganic nanofillers	425@1Hz	-1.91% @ 13 kV/mm	Soft Robotic	293
	PDMS	TiO ₂ nanotubes	Inorganic nanofillers	4@1kHz	4.2% @ 40 kV/mm	Soft Robotic	294
	PU	Barium titanate nanoparticles	Inorganic nanofillers	13.6@1kHz	125% @ 27.3 kV/mm	Soft Robotic	295
	SBAS	Graphene oxide	Conductive nanofillers	11@1kHz	21.3% area strain @ 33 kV/mm	Soft Robotic	303
	Cellulose nanofibers-Epoxy	AgNFs	Conductive nanofillers	9.2@120kHz	-	Capacitive sensor	211
	PDMS	Glycerol	High permittivity liquid	16@1kHz	-	Soft Robotic	382
	4-acryloylmorpholine+N,N'-methylenebis(acrylamide)	Propylene carbonate/Ethylene carbonate	High permittivity liquid	30-50@1k-10MHz	172% @ 4 kV/mm	Soft Robotic	311
Lower elastic modulus	Acrylate	glycidyl methacrylate	Long chain polymer	5.67@1kHz	52.08% @ 21.57 kV/mm	Soft Robotic	315
	VHB	1,6 hexanediol diacrylate	Interpenetrating network	-	233% @ 300 kV/mm	Soft Robotic	339
	Acrylate	1,6-hexanediol diacrylate & dibutoxyethoxyethyl formal	Short-chain crosslinker	5@12Hz	314% @ 344 kV/mm	Soft Robotic	109
	Acrylate	Trimethylolpropane triacrylate	Short-chain crosslinker	3.71	70% @ 127 kV/mm	Soft Robotic	354
Increase electrical breakdown strength	PDMS	Monomethacryloxypropyl side chains	Bottlebrush	2.94@1MHz	300% @ 10 kV/mm	Soft Robotic	383
	Polysiloxane	Butylthioether side chains	Bottlebrush	5.4@1MHz	200% @ 53 kV/mm	Soft Robotic	367
	PDMS	Polyphenylmethylsiloxane	Aromatic voltage stabilizer	3.9@1MHz	72 kV/mm (electrical breakdown strength)	Soft Robotic	369
	PDMS	vegetable-based transformer oil	Liquid dielectric	-	37% @ 33 kV/mm	Soft Robotic	371

*Tensile stress cycle test for transistors